Impacts of a double-moment bulk cloud microphysics scheme (NDW6-G23) on aerosol fields in NICAM.19 with a global 14-km grid resolution

Daisuke Goto[1], Tatsuya Seiki[2], Kentaroh Suzuki[3], Hisashi Yashiro[1], Toshihiko Takemura[4]

[1]National Institute for Environmental Studies, Tsukuba, 305-8506, Japan
[2]Japan Agency for Marine-Earth Science and Technology, Yokohama, 236-0001, Japan
[3]Atmosphere and Ocean Research Institute, The University of Tokyo, Kashiwa, 277-8568, Japan
[4]Research Institute for Applied Mechanics, Kyushu University, Fukuoka, 816-8580, Japan

Correspondence to: Daisuke Goto (goto.daisuke@nies.go.jp)

Abstract. In accordance with progression in current capabilities towards high-resolution approaches, applying a convective-permitting resolution to global aerosol models helps comprehend how complex cloud-precipitation systems interact with aerosols. This study investigates the impacts of a double-moment bulk cloud microphysics scheme, i.e., NICAM Double-moment bulk Water 6 developed in this study (NDW6-G23), on the spatiotemporal distribution of aerosols in the Non-hydrostatic Icosahedral Atmospheric Model as part of the version 19 series (NICAM.19) with 14 km grid spacing. The mass concentrations and optical thickness of the NICAM-simulated aerosols are generally comparable to those obtained from in situ measurements, but the differences between the results of NDW6 and NSW6 experiments were larger for some aerosol species, especially dust and sulfate, ~~have larger differences among the experiments with NDW6 and NSW6~~ compared to those between ~~those among~~ the experiments with different horizontal resolutions, i.e., 14 km and 56 km grid spacing, as shown in a previous study. The simulated aerosol burdens using NDW6 are generally lower than those using NSW6; the net instantaneous radiative forcing due to aerosol-radiation interaction (IRFari) is estimated to be -1.~~57~~36 Wm^{-2} (NDW6) and -1.~~86~~62 Wm^{-2} (NSW6) in the global annual mean values ~~of shortwave all-aerosol radiative forcing~~ at the top of the atmosphere (TOA). The net effective radiative forcing due to anthropogenic aerosol-radiation interaction (ERFari) is estimated to be -0.19 Wm^{-2} (NDW6) and -0.23 Wm^{-2} (NSW6) in the global annual mean values at the TOA. This difference among the experiments using different cloud microphysics modules, ~~e.g.~~i.e., 0.~~29~~26 Wm^{-2} or 16% difference in IRFari values and 0.04 Wm^{-2} or 16% difference in ERFari values, is attributed to a different ratio of column precipitation to the sum of the column precipitation and column liquid cloud water, which strongly determines the magnitude of wet deposition in the simulated aerosols. Since the simulated ratios in the NDW6 experiment are larger than those of the NSW6 result, the scavenging effect of the simulated aerosols in the NDW6 experiment is larger than that in the NSW6 experiment. A large difference between the experiments is also found in the aerosol indirect effect (AIE), i.e., the ~~shortwave~~ net effective radiative forcing due to aerosol-cloud interaction (ERFaci) from the present to preindustrial days, which is estimated to be -1.~~34~~28 Wm^{-2} (NDW6) and -0.~~63~~73 Wm^{-2} (NSW6) in global annual

mean values. The magnitude of the ERFaci value in the NDW6 experiment is larger than that in the NSW6 result, ~~probably~~ due to the differences in the susceptibility of the simulated cloud water to the simulated aerosols between NDW6 and NSW6 and the overestimation of the Twomey effect in NSW6 caused by ignorance of sink process in the cloud droplet number concentrations ~~and partly due to the nonlinear relationship between the ERFaci and AOT under different AOTs~~. Therefore, this study shows the importance of the impacts of the cloud microphysics module on aerosol distributions through both aerosol wet deposition and AIE.

1 Introduction

The aerosol-cloud interaction (ACI) is one of the largest sources of uncertainty in near-term climate projections (Szopa et al., 2021). The radiative forcing related to the ACI is estimated to range from -1.45 Wm^{-2} to -0.25 Wm^{-2}, which is the largest among the various forcing agents (Forster et al., 2021). The major process of the ACI is aerosol ~~nucleation~~ activation to act as cloud condensation nuclei (CCN) and its subsequent modification of cloud properties through perturbations to cloud droplet number concentration (Twomey, 1977) and to cloud lifetime via water conversion from cloud to precipitation (Albrecht, 1989). On the other hand, in terms of the aerosol itself, wet deposition through rainout and washout often dominates the sink process and determines the spatiotemporal distribution. Because most aerosols are hygroscopic, they are removed from the atmosphere mainly by rainout or in-cloud scavenging (e.g., Henzing et al., 2006). In the rainout process, activated or formed aerosols in individual cloud droplets fall to the ground surface by precipitation. The modeling of rainout strongly affects the spatiotemporal variation and distribution of hygroscopic aerosols such as sulfate, organic aerosols, and sea salt (Textor et al., 2006; Myhre et al., 2013; Gliß et al., 2021). Even for less hydroscopic aerosols such as dust and black carbon (BC), the wet deposition process is important to determine their atmospheric lifetime (Koffi et al., 2016; Sand et al., 2021). Thus, aerosols and clouds are tightly connected to each other, and hence, an ~~elaboration~~ evaluation of both the cloud module and aerosol physics module is required to improve the ACI in climate models. One of the methods to improve cloud simulations is the use of convection-permitting resolution, which explicitly represents cloud systems with a detailed cloud microphysics scheme (Satoh et al., 2019; Stevens et al., 2019). In very high-resolution models with a horizontal grid size of O (10 km) or less, clouds and precipitation are more realistically represented compared to conventional global models with a grid size of O (100 km) (e.g., Stevens et al., 2019). These results suggest ~~It is promising~~ that convective cloud systems are better represented with a finer model resolution for which ~~when~~ cumulus parameterizations are avoided (e.g., Vergara-Temprado et al., 2020). However, most global models with convection-permitting resolution do not treat aerosols explicitly or do not deeply evaluate aerosol distributions because of very expensive computational costs (Satoh et al., 2019; Stevens et al., 2019; Coppola et al., 2020).

One of the global models with convection-permitting resolution is the Non-hydrostatic Icosahedral Atmospheric Model (NICAM: Tomita and Satoh, 2004; Satoh et al., 2008; Satoh et al., 2014; Kodama et al., 2021) coupled to an aerosol physics module (Suzuki et al., 2008; Dai et al., 2014; Goto, 2014), and the ACI in global cloud resolving simulations has been examined

65 for a decade or more (Suzuki et al., 2008; Sato et al., 2018; Goto et al., 2020). High-resolution simulations of aerosols have various advantages for reproducing the distribution of the observed aerosols (Goto et al., 2015, 2020) and better representing the ACI effect by ~~simulating~~ more realistically simulating the relationship between changes in cloud liquid water path (LWP) and aerosols (Sato et al., 2018). Especially in the Arctic, the simulated aerosols in the high-resolution model are closer to the observations than those in the low-resolution model (Ma et al., 2014; Sato et al., 2016; Goto et al., 2020). With further

70 improvements in computing resources, online aerosol calculations in such high-resolution models are highly promising next steps for understanding the interaction between aerosols, clouds, and precipitation. On the other hand, some issues remain even in global high-resolution simulations using NICAM (Goto et al., 2020). For example, the difference in the simulated aerosol optical thickness (AOT) with high- and low-resolution models is small and estimated to be 3% ~~in a~~of the global average, whereas the difference in the simulated aerosol mass concentrations at the surface is large and estimated to be 20% near the

75 source areas. Over remote oceans such as the Southern Ocean, the simulated AOT sometimes exceeds 0.3 in monthly averages, which apparently shows the overestimation of the simulated AOT compared to the satellite observations. The simulated AOTs include a relatively large bias of 20% compared to the surface-observed results. Past research (Goto et al., 2020) indicated that ~~the~~ biases could be partially resolved by improving ~~the~~ wet deposition through improved cloud-precipitation processes.

The main objective of this study is to clarify the impacts of cloud microphysics modules on aerosol distribution. Therefore,

80 this study uses two different types of cloud microphysics schemes in the NICAM. For the evaluation, the simulated aerosols, clouds, precipitation, and radiation are compared with the observations. In addition, the global budgets for the simulated aerosols are compared to other models for reference.

Section 2 describes the model and the observations used in this study. Section 3 shows the results of the simulated clouds (section 3.1), precipitation (section 3.1) and aerosols (sections 3.2 and 3.3) in the numerical experiments using both the NICAM

85 double-moment bulk cloud microphysics module (NDW6) and the NICAM single-moment bulk module with 6 water categories (NSW6). They are evaluated by a reference obtained from the NICAM with 14 km and 56 km grid spacing in Goto et al. (2020). Section 4 shows and discusses the impacts of aerosols on radiation through aerosol-radiation interactions (ARIs) and ACIs by comparing them with references obtained from both models and satellites. Finally, the summary is shown in section 5.

90 **2 Model descriptions and method**

2.1 Atmospheric model

The NICAM is a ~~nonhydrostatic~~ Non-hydrostatic atmospheric model (Tomita and Satoh, 2004; Satoh et al., 2008; Satoh et al., 2014) that can be ~~calculated~~ run with a coarse resolution of ~~from~~ 50 km to 200 km (e.g., Dai et al., 2014; Kodama et al., 2021). It is also a global model with convection-permitting resolution (Satoh et al., 2019) that greatly helps the understanding of

95 atmospheric phenomena related to clouds and precipitation by resolving the ~~interacting behavior of~~interaction among multiple convective systems (Satoh et al., 2014). The horizontal grid sizes in the NICAM generally range from O(1 km) to O(10 km)

and are often set at 14 km for a useful and effective balance between model complexity and computing resources (Kodama et al., 2014; Kodama et al., 2021; Seiki et al., 2022). NICAM aerosol simulations with 14 km grid sizes were performed for the entire year (Sato et al., 2018; Goto et al., 2020). This study improves previous aerosol simulations (Goto et al., 2020) by using

100   an upgraded version of the NICAM (replacing the version 16 series with the version 19 series, hereafter referred to as NICAM.19) and the sophisticated cloud microphysics module NDW6 (the original version named NDW6-~~SK14~~ SN14 was incorporated into the NICAM by Seiki and Nakajima, 2014, the updated version named NDW6-S15 ~~were~~ was ~~reflected~~ incorporated into the version in NICAM.19 by Seiki et al., 2014, 2015, and the current version named NDW6-G23 considers the interaction between ~~the~~ NDW6-S15 and an aerosol module is introduced to NICAM.19 in this study. The details of the

105   NDW6 update are described in Seiki et al., 2022).

NICAM.19 is an official version of the NICAM that was released at the end of 2019. After the official release, minor updates in NICAM.19 ~~are~~ were continu~~ously released~~ing. One of the updates of NICAM.19 from NICAM.16 is the vertically high resolution in the standard experiment. The number of vertical layers in NICAM.19 is 78 (15 layers below 2-km height), which is finer than the 38 (10 layers below 2-km height) in NICAM.16. The layer heights at the bottom and top are 33 m and 50 km,

110   respectively, in NICAM.19, whereas they are 81 m and 37 km, respectively, in NICAM.16. The increased vertical levels force the timestep to change from 60 seconds in NICAM.16 to 30 seconds in NICAM.19. Various bugs in NICAM.16 are eliminated in NICAM.19, and the aerosol module in NICAM.19 is also updated (explained in section 2.2).

This study uses the double-moment bulk cloud microphysics scheme NDW6, which is newly coupled to the aerosol physics module in this study. For ~~a~~ comparison, the original single-moment bulk cloud microphysics scheme (NSW6: Tomita, 2008;

115   Kodama et al., 2012; Roh and Satoh, 2014) is also used. NSW6 predicts the mass mixing ratios of 6 ~~hydrometeors~~water substances, i.e., water vapor, cloud water, rain, cloud ice, snow, and graupel. Therefore, the cloud droplet number concentration (CDNC) is assumed to be the same as CCN, which was calculated by coupling with the aerosol physics model using the CCN parameterization proposed by Abdul-Razzak and Ghan (2000). This parameterization is a function of the parameterized updraft velocity with turbulent kinetic energy (Lohmann et al., 1999), aerosol sizes, and aerosol chemical composition. The CDNC is

120   then used for autoconversion and accretion in rain formation. In this way, the ACI for both ~~the~~ stratiform- and convective-cloud systems is incorporated in the cloud microphysics scheme. On the other hand, NDW6 predicts both the mass mixing ratios and the number concentrations of ~~hydrometeors~~water substances. Prior to this study, NDW6 ~~is~~ was not coupled with aerosol physics models, and CCN number concentrations at a background level ~~are~~ were assumed to be constant globally (Seiki and Nakajima, 2014). In accordance with the nucleation procedure, the background CCN value set at NDW6-SN14 and

125   NDW6-S15 is replaced with predicted CCN values from the aerosol physics model using the CCN parameterization (Abdul-Razzak and Ghan 2000). In addition, a source term of CDNC value is assumed to be updated to a CCN value only when the CCN value exceeds the CDNC value in a grid box. The CDNC is updated with source (aerosol activation) and sink (autoconversion, accretion, and evaporation for water clouds) in NDW6 (Seiki and Nakajima, 2014). The balance of source and sink tendencies determines the CDNC in NDW6. In this way, NSW6 and NDW6 coupled with the aerosol physics model

130   are affected by the global distribution of aerosols.

Note that autoconversion and accretion, which mainly determine the strength of aerosol lifetime effects (Albrecht, 1989), are different between NSW6 and NDW6. NDW6 uses the parameterization proposed by Seifert and Beheng (2006), and NSW6 uses the parameterization proposed by Khairoutdinov and Kogan (2000)~~, which is updated in this study (cf., Seiki and Roh, 2020)~~. In addition, since NDW6 predicts the CDNC, the CDNC and aerosols are individually transported by advection and

135 removed by reduction terms. In contrast, NSW6 assumes that a change in CCN directly connects with a change in diagnosed CDNC~~, although rain does not directly change cloud water in this case~~. ~~Thus, the impact of scavenged aerosols on cloud water is inevitably overestimated in single-moment bulk cloud microphysics schemes.~~ These differences influence the representation of ACI.

Most relevant cloud parameters used to evaluate the ACI, e.g., LWP and cloud droplet effective radius (CDR), are output in
140 every timestep, but in this study, cloud albedo (CA) is assumed by the following formulation (Platnick and Twomey, 1994) using monthly mean cloud optical thickness (COT or τ_c) for water clouds as postprocessing after the model integration.

$$CA = \frac{\tau_c(1-g)}{1.5+\tau_c(1-g)} \qquad (1)$$

where g is the asymmetry factor and set at 0.85. The cloud fraction (CF) is defined as the cloud occurrence frequency because NICAM with NDW6 and NSW6 does not consider partial-grid clouds. Clouds in a grid exist when the mixing ratios of the
145 sum of cloud water and rain exceed 10^{-5} (kg m^{-3}), which can be detected by satellites (Goto et al., 2019).

Other physical processes in this study are identical to those set in Goto et al. (2020). The advection module is per Miura (2007) and Niwa et al. (2011). The diffusion module is the level-2 Mellor-Yamada-Nakanishi-Niino (MYNN) scheme (Mellor and Yamada, 1972; Nakanishi and Niino, 2004; Noda et al., 2010). ~~Similar~~ As ~~to~~ in previous studies using the NICAM (e.g., Satoh et al., 2010; Kodama et al., 2021), ~~a~~ no ~~cumulus~~ parameterization schemes for deep and shallow convection ~~is~~ are ~~not~~ used in
150 this study. The land surface module is the Minimal Advanced Treatments of Surface Interaction and Runoff (MATSIRO) (Takata et al., 2003). The radiation module is the Model Simulation Radiation Transfer code (MSTRN-X) (Sekiguchi and Nakajima, 2008). The aerosol module is the Spectral Radiation-Transport Model for Aerosol Species (SPRINTARS) (Takemura et al., 2005; Suzuki et al., 2008), which is explained in section 2.2.

~~The NICAM-simulated cloud, precipitation, and radiation fluxes at the top of atmosphere (TOA) are evaluated by satellite~~
155 ~~products. The satellite-based product of precipitation is provided by version 2.2 of the Global Precipitation Climatology Project~~ ~~(GPCP) with monthly 2.5°×2.5° grids (Adler et al., 2003). The satellite-based product of the cloud liquid water path (LWP) is~~ ~~provided by the Multisensor Advanced Climatology (MAC) Total Liquid Water Path L3 with monthly 1°×1° grids (Elsaesser~~ ~~et al., 2017). The ratio of the column precipitation to the sum of the column precipitation and cloud liquid water is calculated~~ ~~by CloudSat products of cloud liquid water and precipitation liquid water in 2C-RAIN-PROFILE (Lebsock and L'ecuyer,~~
160 ~~2011). According to Lebsock and L'ecuyer (2011), this product is more reliable than other Cloudsat products, such as 2C-~~ ~~RAIN-COLUMN, but this product is retrieved over only the ocean, and CloudSat cannot properly detect signals below a height~~ ~~of 1 km (Christensen et al., 2013; Huang et al., 2012; Liu, 2002). The cloud optical thickness (COT) is retrieved from the~~ ~~Moderate Resolution Imaging Spectroradiometer (MODIS) for all types of clouds (Platnick et al., 2015). The cloud fraction~~

2.2 Aerosol module

The mass mixing ratios of the major tropospheric aerosols (dust, sea salt, carbonaceous aerosols including organic matter or OM and BC, and sulfate) and the precursors of sulfate (SO_2 and dimethyl sulfide or DMS) are explicitly calculated in the SPRINTARS-based aerosol module. The details of the aerosol module that is coupled to the NICAM are also described elsewhere (Dai et al., 2014; Goto et al., 2015, 2019, 2020; Goto and Uchida, 2022), but the main three updates in this study are explained as follows. First, when the CCN number concentration is higher than the CDNC is calculated online in the aerosol module, the value of water supersaturation is positive, and the atmospheric pressure is above 300 hPa, the CCN number concentration becomes an input of source tendency for CDNCaerosol nucleation process is calculated using the CCN number concentration. The vertical fluxes of the simulated hydrometeors, except for water vapor, in the cloud microphysics module are used in the wet deposition for aerosols. Second, the assumption of sulfate in clouds is modified. In this study, the sulfate formed in the clouds by aqueous-phase oxidation at the current timestep is not scavenged by the rainout process at the same timestep because the cloud water used in aqueous-phase oxidation is an output at the current timestep. The model timestep is 30 seconds, so this assumption is reasonable in this simulation. Because the model timestep was more than 1 minute in previous studies (Goto et al., 2020), the original model assumes that the sulfate formed in clouds by aqueous-phase oxidation is scavenged by the rainout process at the same timestep. This is one of the uncertainties of the modeling, and the assumption has an impact on the simulated sulfate, as shown later. Third, the treatment of dust aerosols is modified according to the latest version of SPRINTARS coupled to MIROC (Takemura et al., 2009; Tatebe et al., 2019). Dust particles in a wide range of sizes (from 0.13 μm to 8.02 μm in mode radii) are divided into bins, and the number of bins is reduced from 10 to 6. In addition, the dependence of on the leaf area index (LAI) is a newly introduced function of the dust emissions in the aerosol module. The dust emission is a function of the cube of the wind speed at a height of 10 m, absorbed photosynthesis radiation depending on the LAI, soil moisture, and snow cover by using empirical coefficients that depend on 7 regions in the world (Takemura et al., 2009). The empirical coefficients, i.e., threshold values of soil moisture and emission strength, are newly tuned in this study. Except for these updates, the treatment and tuning parameters for the aerosol processes in this study are identical to those in Goto et al. (2020).

The emission fluxes used in this study are the Hemispheric Transport of Air Pollution (HTAP)-v2.2 (Janssen-Maenhout et al., 2015) for BC, organic carbon (OC) and SO_2 from anthropogenic materials and the Global Fire Emission Database (GFED) version 4 (van der Werf et al., 2017) for BC, OC and SO_2 from biomass burning. The ratio of OC to OM is set at 1.6 for

anthropogenic activities and 2.6 for biomass burning (Tsigaridis et al., 2014). Secondary organic aerosols (SOAs) are assumed to be particles by multiplying the emission fluxes of isoprene and terpenes provided by the Global Emissions Initiative (GEIA) (Guenther et al., 1990). Parts of SO₂ are emitted from volcanic eruptions (Diehl et al., 2012) and are formed from DMS, which is interactively emitted in the aerosol module (Bates et al., 1987). Sulfate is formed from SO₂ oxidation with a 3-dimensional distribution of monthly oxidants (ozone, H₂O₂ and OH) provided by a chemical transport model (CHASER) coupled to MIROC (Sudo et al., 2002). Emission fluxes for dust (Takemura et al., 2009) and sea salt (Monahan et al., 1986) are interactively calculated in the model using mainly the wind speed at a height of 10 m.

The removal processes, i.e., wet deposition, dry deposition, and gravitational settling, for aerosols are not different from those used in previous studies (Goto et al., 2020; Goto and Uchida, 2022). However, the wet deposition fluxes simulated by the NICAM in this study are directly modulated by the change in the cloud microphysics modules and autoconversion from clouds to precipitation because the wet deposition flux is strongly related to clouds and precipitation outside of the aerosol module (Goto and Uchida, 2022).

For carbonaceous aerosols, SPRINTARS assumes both external and internal mixtures of organic matter (OM) and BC. Pure OM is generated from terpenes as a product of SOA, whereas pure BC is directly emitted from one-half of the amount in anthropogenic sources. SPRINTARS assumes that pure BC is not aged in the atmosphere. The BC and OM components emitted from other emission sources are internally mixed as two types of internal mixtures of OM and BC with BC to OM ratios of 0.3 and 0.15, respectively. BC, OM and sulfate are assumed to have unimodal lognormal particle size distributions with mode radii of 0.1 μm for the internal mixture of BC and OM, 0.08 μm for pure OM, 0.054 μm for pure BC and 0.0695 μm for sulfate. For sea salt, there are 4 categories of tracers, with mode radii of 0.178 μm, 0.562 μm, 1.78 μm, and 5.62 μm, that do not age or coagulate with each other in SPRINTARS. The internal mixture of BC and OM, pure OM, sulfate, and sea salt is hydrophilic, whereas the dust and pure BC are hydrophobic. Such physical properties for aerosols in this study are identical to those used in Goto et al. (2020).

The optical properties of the aerosols and the calculation methods for ACI in this study are also identical to those used in Goto et al. (2020). The aerosol optical thickness (AOT) at a wavelength of 550 nm is calculated online by the mass concentrations and optical properties for the aerosols and a look-up table prescribed by the Mie theory (Sekiguchi and Nakajima, 2008). To evaluate the radiative forcing of the ARI and ACI, the instantaneous radiative forcing of the ARI (IRFari) and effective radiative forcing for the ACI (ERFaci) are calculated by a general method (e.g., Shindell et al., 2013). The IRFari due to each aerosol species is calculated online by the difference in the radiative fluxes with/without the aerosol species in the radiation module (Goto et al., 2020). The ERFari due to anthropogenic aerosols is calculated as the difference in the IRFari between the preindustrial and present conditions of aerosols. The ERFaci due to anthropogenic aerosols only is calculated by the difference in the cloud radiative fluxes between the preindustrial and present conditions of aerosols according to the method proposed by Ghan (2013). The impacts of anthropogenic aerosols on radiative forcing are estimated by the difference between the standard experiment and the extra experiment under preindustrial conditions. In the extra experiment, everything is the same as those in the standard experiment, except that the anthropogenic emission fluxes of BC, OC and SO₂ are set to zero. The uncertainty

of this assumption is mentioned in section 2.3. In all the experiments, the results presented here are the 6-year simulations after the 1-month spinup calculation, which are obtained from the end of the 1-year aerosol online simulations coupled to NSW6. All the experiments in this study are summarized in Table 1.

In this study, the simulated aerosols are evaluated by in situ measurements and satellite aerosol products. The climatological observations used in the evaluation of the simulated aerosol mass concentrations are provided by the Interagency Monitoring of Protected Visual Environments (IMPROVE; Malm et al., 1994) program in the United States, the European Monitoring and Evaluation Programme (EMEP) in Europe, the Acid Deposition Monitoring Network in East Asia (EANET) in Asia, and the China Meteorological Administration Atmosphere Watch Network (CAWNET; Zhang et al., 2012) in China. The climatological observations used in the evaluation of the simulated AOT are provided by the Aerosol Robotic Network (AERONET; Holben et al., 1998), SKYNET radiometer network (Nakajima et al., 2020), and China Aerosol Remote Sensing Network (CARSNET; Che et al., 2015). These identical datasets were prepared and used in Goto et al. (2020), which shows the location map and description in Table 1 and Figure 1. In the global aerosol validation, the level 3 AOT product of Collection 6 MODIS onboard the polar-orbiting satellite Terra (MOD08_L3) by Platnick et al. (2015) is used. The AOT is retrieved from the deep blue (Hsu et al., 2013) and dark target (Levy et al., 2013) methods. The uncertainty of the retrieved AOT from both methods is similar to each other (Sayer et al., 2014) and estimated to be ± (0.05 + 0.15*AOT) (Levy et al., 2013). However, satellite-retrieved AOTs are still divergent among different sensors (Petrenko and Ichoku, 2013; Alfaro-Contreras et al., 2017; Wei et al., 2019; Sogacheva et al., 2020), so the level 3 AOT product from collection F15_0031 (V22 level 3) of the Multiangle Imaging Spectroradiometer (MISR) onboard Terra by Kahn et al. (2010) is also used in this study. While MODIS has 36 bands from 0.41 μm to 14 μm, a single view and a broad swath of 2330 km, MISR has four bands (0.45 μm, 0.56 μm, 0.67 μm, and 0.87 μm) with nine cameras with the narrowest swath at 380 km. The uncertainty of MISR-retrieved AOT is estimated to be 0.05 or 0.2*AOT (Kahn et al., 2010). Wei et al. (2019) showed that the MODIS-retrieved AOT is the closest to AERONET, and the MISR-retrieved AOT is the second closest to AERONET among various satellite AOT products. Alfaro-Contreras et al. (2017) showed that the bias of the AOT between MODIS and MISR is found over the Southern Ocean, where the MISR-retrieved AOT is larger than the MODIS-retrieved AOT due to cloud contamination (Toth et al., 2013). Petrenko and Ichoku (2013) showed the large uncertainty of the MODIS-retrieved AOT over high albedo areas such as desert, snow, and ice surface. In East Asia, the MISR-retrieved AOT is lower than the AERONET-retrieved AOT, but the MODIS-retrieved AOT is higher than the AERONET-retrieved AOT (Kahn et al., 2010). The 3-dimensional distribution of the aerosol extinction coefficients obtained from the Cloud-Aerosol Lidar with Orthogonal Polarization (CALIOP)/Cloud-Aerosol Lidar and Infrared Pathfinder Satellite Observations (CALIPSO) version 3 provided by the NASA Langley Research Center (LaRC) are used in a 1°×1° grid under clear-sky conditions (Winker et al., 2013). The CALIOP (version 3)-retrieved AOTs are sometimes compared with the MODIS (Collection 6)-retrieved AOTs in previous studies (Kim et al., 2018; Liu et al., 2018; Proestakis et al., 2018). Kim et al. (2018) show that the differences in the CALIOP (version 3)-retrieved AOT and MODIS-retrieved AOT are estimated to be -0.010 over ocean and +0.069 over land due to the inconsistency of the footprint resolution. Compared to the AERONET-retrieved AOT, the CALIOP-retrieved AOT is lower by 0.064. Therefore, over land, the CALIOP-retrieved AOT is underestimated, and the MODIS-retrieved AOT is overestimated. Liu et al. (2018) also showed that the CALIOP-retrieved AOT for polluted days in China is more reliable than the MODIS-retrieved AOT. Therefore, the difference in the retrieved AOT between MODIS, MISR, and CALIOP can be considered as the uncertainty of the satellite retrievals for AOT. These satellite datasets are averaged for the 3 years from 2012-2014. **2.3 Experimental conditions**

All experiments with both NDW6 and NSW6 are carried out for 6-years after the 1-month spin-up calculation. The simulation results are climatological runs, because the model does not nudge meteorological fields such as wind and temperatures but nudges the sea surface temperature (SST) and sea ice by the results of the NICAM from Kodama et al. (2015). The initial conditions for the model spin-up are obtained from the end of the 1-year aerosol simulations coupled to NSW6 without nudging the meteorological fields under the present era.

The emission fluxes used in this study are the Hemispheric Transport of Air Pollution (HTAP)-v2.2 (Janssen-Maenhout et al., 2015) for BC, organic carbon (OC) and SO_2 from anthropogenic sources in 2010 and the Global Fire Emission Database (GFED) version 4 (van der Werf et al., 2017) for BC, OC and SO_2 from biomass burning in climatological average from 2005 to 2014. The ratio of OC to OM is set at 1.6 for anthropogenic activities and 2.6 for biomass burning (Tsigaridis et al., 2014).

Secondary organic aerosols (SOAs) are assumed to form particles, which are calculated by multiplying the emission fluxes of isoprene and terpenes provided by the Global Emissions Initiative (GEIA) (Guenther et al., 1990) using constant factors. SO_2 is emitted from volcanic eruptions (Diehl et al., 2012) and is also formed from DMS, which is interactively emitted in the aerosol module (Bates et al., 1987). Sulfate is formed from SO_2 oxidation with a 3-dimensional distribution of monthly oxidants (ozone, H_2O_2 and OH) provided by a chemical transport model (CHASER) coupled to MIROC (Sudo et al., 2002). Emission fluxes for dust (Takemura et al., 2009) and sea salt (Monahan et al., 1986) are interactively calculated in the model using mainly the wind speed at a height of 10 m.

In the preindustrial experiments, the anthropogenic emission fluxes of BC, OC and SO_2 are assumed to be zero in this study. Hoesly et al. (2018) estimated global averages of the differences in the emission amounts of anthropogenic sources between 1850 and 2010 to be 2.1% (sulfate), 12.0% (BC), and 22.7% (OC). The residential sector has the largest contribution to the total anthropogenic emissions in the preindustrial era. Takemura (2020) calculated the IRFari due to anthropogenic sulfate under the conditions of 0% and 30% of the present emissions and found that the difference in the IRFari was within 0.03 Wm^{-2}. Therefore, differences in the assumptions for the preindustrial era between this study and other studies, such as IPCC-AR6 (Szopa et al., 2021), will result in a difference in the IRFari due to anthropogenic sources of at most 0.05 Wm^{-2}. Takemura (2020) also calculated ERFari and ERFaci due to anthropogenic sulfate under the conditions of 0% and 30% of the present emissions and found that the difference in ERFari plus ERFaci was within 0.2 Wm^{-2}. These are possible uncertainties in the estimated radiative forcings due to anthropogenic sources in this study, but these magnitudes are smaller than the difference between NDW6 and NSW6 in this study, as shown in section 4.

2.4 Observations

The NICAM simulated cloud, precipitation, and radiation fluxes at the top of atmosphere (TOA) are evaluated by satellite products. The satellite-based product of precipitation is provided by version 2.2 of the Global Precipitation Climatology Project (GPCP) with monthly 2.5°×2.5° grids (Adler et al., 2003). The satellite-based product of the cloud liquid water path (LWP) is provided by the Multisensor Advanced Climatology (MAC) Total Liquid Water Path L3 with monthly 1°×1° grids (Elsaesser et al., 2017). The ratio of the column precipitation to the sum of the column precipitation and cloud liquid water is calculated by CloudSat products of cloud liquid water and precipitation liquid water in 2C-RAIN PROFILE (Lebsock and L'ecuyer, 2011). According to Lebsock and L'ecuyer (2011), this product is more reliable than other Cloudsat products, such as 2C-RAIN COLUMN, but this product is retrieved over only the ocean, and CloudSat cannot properly detect signals below a height of 1 km (Christensen et al., 2013; Huang et al., 2012; Liu, 2002). The cloud optical thickness (COT) is retrieved from the

The NICAM-simulated cloud, precipitation, and radiation fluxes at the top of the atmosphere (TOA) are evaluated by satellite products. The satellite-based product of precipitation is provided by version 2.2 of the Global Precipitation Climatology Project (GPCP) with monthly 2.5°×2.5° grids (Adler et al., 2003). The satellite-based product of the LWP is provided by the Multisensor Advanced Climatology (MAC) Total Liquid Water Path L3 with monthly 1°×1° grids (Elsaesser et al., 2017). The ratio of the column precipitation to the sum of the column precipitation and cloud liquid water is calculated by CloudSat products of cloud liquid water and precipitation liquid water in 2C-RAIN-PROFILE (Lebsock and L'ecuyer, 2011). According to Lebsock and L'ecuyer (2011), this product is more reliable than other Cloudsat products, such as 2C-RAIN-COLUMN, but this product is retrieved over only the ocean, and CloudSat cannot properly detect signals below a height of 1 km (Christensen et al., 2013; Huang et al., 2012; Liu, 2002). The cloud optical thickness (COT) is retrieved from the Moderate Resolution Imaging Spectroradiometer (MODIS) for all types of clouds (Platnick et al., 2015). The CF at a low level is estimated from datasets under the International Cloud Climatology Project (ISCCP; Rossow and Schiffer, 1999). The satellite-based radiation fluxes, i.e., outgoing shortwave and longwave radiative flux (hereafter referred to as OSR and OLR) and shortwave and longwave cloud radiative forcing (hereafter referred to SWCRF and LWCRF), are provided by the Clouds and the Earth's Radiant Energy System (CERES) experiment onboard Terra and Aqua, as CERES_EBAF_Ed4.1, with 1°×1° grids (Loeb et al., 2009). For the comparisons in this study, these datasets are averaged for the 3 years from 2012-2014, except for approximately 6 yearly averages (June 2006 to April 2011) in 2C-RAIN-PROFILE.

The NICAM-simulated aerosols are evaluated by in situ measurements and satellite aerosol products. The climatological observations used in the evaluation of the simulated aerosol mass concentrations are provided by the Interagency Monitoring of Protected Visual Environments (IMPROVE; Malm et al., 1994) program in the United States, the European Monitoring and Evaluation Programme (EMEP) in Europe, the Acid Deposition Monitoring Network in East Asia (EANET) in Asia, and the China Meteorological Administration Atmosphere Watch Network (CAWNET; Zhang et al., 2012) in China. The climatological observations used in the evaluation of the simulated AOT are provided by the Aerosol Robotic Network (AERONET; Holben et al., 1998), SKYNET radiometer network (Nakajima et al., 2020), and China Aerosol Remote Sensing Network (CARSNET; Che et al., 2015). The same datasets were prepared and used in Goto et al. (2020), which shows the location map and description in Table 1 and Figure 1. In the global aerosol validation, the level 3 AOT product of Collection 6 MODIS onboard the polar-orbiting satellite Terra (MOD08_L3) by Platnick et al. (2015) is used. The AOT is retrieved from the deep blue (Hsu et al., 2013) and dark target (Levy et al., 2013) methods. The uncertainty of the retrieved AOT from both

methods is similar to each other (Sayer et al., 2014) and estimated to be ± (0.05 + 0.15*AOT) (Levy et al., 2013). However, satellite-retrieved AOTs are still divergent among different sensors (Petrenko and Ichoku, 2013; Alfaro-Contreras et al., 2017; Wei et al., 2019; Sogacheva et al., 2020), so the level 3 AOT product from collection F15_0031 (V22 level 3) of the Multiangle Imaging Spectroradiometer (MISR) onboard Terra by Kahn et al. (2010) is also used in this study. While MODIS has 36 bands from 0.41 μm to 14 μm, a single view and a broad swath of 2330 km, MISR has four bands (0.45 μm, 0.56 μm, 0.67 μm, and 0.87 μm) with nine cameras with the narrowest swath at 380 km. The uncertainty of MISR-retrieved AOT is estimated to be 0.05 or 0.2*AOT (Kahn et al., 2010). Wei et al. (2019) showed that the MODIS-retrieved AOT is the closest to AERONET, and the MISR-retrieved AOT is the second closest to AERONET among various satellite AOT products. Alfaro-Contreras et al. (2017) showed that the bias of the AOT between MODIS and MISR is found over the Southern Ocean, where the MISR-retrieved AOT is larger than the MODIS-retrieved AOT due to cloud contamination (Toth et al., 2013). Petrenko and Ichoku (2013) showed the large uncertainty of the MODIS-retrieved AOT over high albedo areas such as desert, snow, and ice surfaces. In East Asia, the MISR-retrieved AOT is lower than the AERONET-retrieved AOT, but the MODIS-retrieved AOT is higher than the AERONET-retrieved AOT (Kahn et al., 2010). The 3-dimensional distribution of the aerosol extinction coefficients obtained from the Cloud-Aerosol Lidar with Orthogonal Polarization (CALIOP)/Cloud-Aerosol Lidar and Infrared Pathfinder Satellite Observations (CALIPSO) version 3 provided by the NASA Langley Research Center (LaRC) are used in a 1° × 1° grid under clear-sky conditions (Winker et al., 2013). The CALIOP (version 3)-retrieved AOTs are sometimes compared with the MODIS (Collection 6)-retrieved AOTs in previous studies (Kim et al., 2018; Liu et al., 2018; Proestakis et al., 2018). Kim et al. (2018) show that the differences in the CALIOP (version 3)-retrieved AOT and MODIS-retrieved AOT are estimated to be -0.010 over ocean and +0.069 over land due to the inconsistency of the footprint resolution. Compared to the AERONET-retrieved AOT, the CALIOP-retrieved AOT is lower by 0.064. Therefore, over land, the CALIOP-retrieved AOT is underestimated, and the MODIS-retrieved AOT is overestimated. Liu et al. (2018) also showed that the CALIOP-retrieved AOT for polluted days in China is more reliable than the MODIS-retrieved AOT. Therefore, the difference in the retrieved AOT between MODIS, MISR, and CALIOP can be considered as the uncertainty of the satellite retrievals for AOT. These satellite datasets are averaged for the 3 years from 2012-2014.

2.5 Reference datasets

Our previous model results provided in Goto et al. (2020) using NICAM.16 at a global 14-km high resolution (hereafter referred to as the HRM) and a global 56-km low resolution (hereafter referred to as the LRM) are used as references to compare the NICAM results. As mentioned in section 2.1, the number of vertical layers is set at 38, and the timestep is 1 minute in both the HRM and LRM. The integration periods in both the HRM and LRM are 3 years as climatological runs. The emission inventories, i.e., 2010 for anthropogenic sources, climatological average in 2005-2014 for biomass burning, and natural sources in the present era, and the nudged SST and sea ice in this study are identical to those in both the HRM and LRM, but the initial conditions in this study are different from those in both the HRM and LRM, which use the model results at the end of December after a 1.5-month spin-up. The initial conditions for the model spin-up are prepared by the reanalysis datasets of the National

Centers for Environmental Prediction (NCEP) Final (FNL) (Kalnay et al., 1996) in November 2011. In the cloud microphysics and autoconversion modules, NDW6 coupled to Seifert and Beheng (2006) and NSW6 coupled to Khairoutdinov and Kogan (2000) are used in this study, whereas NSW6 coupled to Berry (1967) is used in both the HRM and LRM. The improvement in the aerosol module described in section 2.2 is also different from that in the HRM and LRM. The results of the HRM and LRM are useful for evaluating the current model results because the observations are limited in some parameters, such as aerosol global budgets and radiative forcings.

In addition to the results in Goto et al. (2020) as references for a comparison of global aerosol budgets and aerosol optical properties, results obtained from the AeroCom Phase-III project (Gliß et al., 2021) are used in this study. AeroCom Phase-III includes 14 global models and can be the best reference to evaluate global aerosol simulations. For references of the IRFari, the Max Planck Aerosol Climatology version 2 (MACv2 by Kinne, 2019) provides global maps for aerosol optical and radiative properties by calculating an offline radiative transfer model with the ensemble mean among the AeroCom global models and the in-situ measurements of AERONET. Another reference for IRFari is the mean value from more than 10 studies based on the observations in Thorsen et al. (2021). The IRFari in Thorsen et al. (2021) is only estimated in the shortwave at the TOA.

3 Results and discussion

3.1 Precipitation and clouds

For simplicity, the simulated ~~products~~ results in the numerical experiment with the NDW6 (or NSW6) cloud microphysics module are expressed hereafter as "the NDW6(NSW6)-simulated ~~products~~results". First, the NICAM-simulated (i.e., both NDW6- and NSW6-simulated) precipitation and clouds are evaluated ~~by~~ using satellite ~~data~~results. Figure 1 shows the zonal and horizontal distributions of the annual, January and July averages of precipitation. Table ~~2~~1 includes the global and annual mean values of precipitation, which are estimated to be 3.01 mm day^{-1} (NDW6), 2.78 mm day^{-1} (NSW6), and 2.68 mm day^{-1} (GPCP). These differences among NDW6, NSW6, and GPCP are also found in January and July. The main reason for these differences is the overestimation of NICAM-simulated precipitation over the tropics. This tendency can be found in previous studies using other high-resolution models with finer horizontal resolutions (e.g., Stevens et al., 2019; Wedi et al., 2020).

Figure 2 shows the zonal and horizontal distributions of the annual, January and July averages of the LWP over only the oceans. The global and annual mean LWP values over only the oceans (60°S-60°N) are estimated to be 95.8 g m^{-2} (NDW6), 104.4 g m^{-2} (NSW6), and 119.6 g m^{-2} (MAC). The zonal and annual distributions of the NDW6-simulated LWP near the polar regions (> 45°S and > 45°N) ~~is~~ are more comparable to the MAC results than to the NSW6 results. This feature is explained by the better reproducibility of supercooled liquid water in low-level mixed-phase clouds (Roh et al., 2020; Seiki and Roh, 2020; Noda et al., 2021). ~~In the other regions, i.e., 45°S-45°N, the NDW6-simulated LWP is not closer to the MAC result compared to the NSW6 result.~~ In the tropics where the LWP is larger than the other areas, the NDW6-simulated LWP is lower and not

closer to the MAC results than the NSW6-simulated LWP. Notably, the MAC results contain regional biases of up to 25%, especially in the tropics (Elsaesser et al., 2017), but even with the largest errors, the NDW6- and NSW6-simulated LWPs in the tropics are still underestimated compared to the MAC results. In the horizontal distribution over the eastern Pacific Ocean and Southern Atlantic Ocean at lower latitudes (30°S-0), the NDW6-simulated LWP is lower than the NSW6 results but comparable to the MAC results. However, over the western Pacific Ocean and Indian Ocean at the lower latitudes, both NDW6- and NSW6-simulated LWPs are lower than the MAC results. Therefore, the overestimation of the NSW6-simulated LWP in the eastern Pacific Ocean and Southern Atlantic Ocean effectively balanced the underestimation of the zonal averages of the simulated LWP and unexpectedly led to zonal LWP values closer to the MAC results. This situation also occurs in the northern hemisphere at lower latitudes (30°N-0). Therefore, in the lower latitudes (30°S-30°N), the zonal averages of the NSW6-simulated LWP look closer to the MAC results, but this is attributed to the compensation errors in the regional distribution. As a result, ~~However, the seasonal and horizontal biases of the NSW6-simulated LWP are effectively cancelled, and~~ the global and annual mean values of the NSW6-simulated LWP appear closer to the MAC results. ~~In terms of the distribution pattern and seasonal cycle, the NDW6-simulated LWP is closer to the MAC result compared to the NSW6 result. The low bias of the NICAM-simulated LWP over the tropics is caused by underestimation in the western Pacific Ocean.~~

Table ~~2~~ 1 includes other cloud information (COT and CF at the low level). Both NDW6- and NSW6-simulated COTs in annual, January and July global mean values are underestimated compared to the MODIS results. This tendency is similar to the results of the LWP. In the spatial distribution, the NDW6-simulated COT has a lower bias over midlatitude to polar regions, whereas the NSW6-simulated COT has a lower bias in other areas (not shown). For low-altitude CF ~~at the low level~~, the differences between the NDW6- and NSW6-simulated results are very small, and both results are underestimated compared to the ISCCP results. Therefore, the difference in the cloud microphysics module has almost no impact on the CF.

In summary, the global and annual mean values of the NDW6 simulation include biases of +12% in ~~the~~ precipitation, -20% in the LWP, -45% in the COT, and -28% in the CF at low levels. The biases in the NSW6 simulation have the same sign, but their magnitudes are slightly different (+4% in the precipitation, -13% in the LWP, -35% in the COT, and -27% in the CF at low levels). These mean values are useful for discussing differences among global climate models in terms of the global budget, but they generally include compensation errors in ~~time and~~ space, as explained above. Therefore, the results of precipitation in both NDW6 and NSW6 are comparable to the observations, but those of LWP in NDW6 are different from those in NSW6. The ~~in~~ NDW6-simulated LWPs are generally ~~better and~~ closer to ~~those of~~ the ~~real atmosphere~~observations, except for the tropics.

3.2 Mass loading of aerosols

NICAM-simulated aerosols are evaluated by statistical metrics, including the Pearson correlation coefficient (PCC), normalized mean bias (NMB), and root-mean-square error (RMSE), defined as (A1), (A2) and (A3) in Appendix A. Figure 3 shows scatterplots of the surface mass concentrations of the NICAM-simulated and observed aerosols. For OM, the calculated statistical metrics in NDW6 are 0.847 (PCC), 3.40 μg m^{-3} (RMSE), and -30.4% (NMB), and the difference between NDW6

and NSW6 is very small. For BC, the calculated statistical metrics in NDW6 are 0.904 (PCC), 1.05 µg m^{-3} (RMSE), and -53.4% (NMB). The difference in the simulated BC between NDW6 and NSW6 is also very small. For sulfate, the calculated statistical metrics in NDW6 are 0.807 (PCC), 3.97 µg m^{-3} (RMSE), and -10.4% (NMB), whereas those in NSW6 are 0.853 (PCC), 3.67 µg m^{-3} (RMSE), and -3.7% (NMB).

445   Figure 4 and Table ~~A1~~ A2 indicate global and annual mean values of column burden, emission, and atmospheric lifetime, which ~~is~~ are calculated by the ratio of column burden to total deposition amount. The column burdens of the NDW6- and NSW6-simulated dust range within the uncertainty of the recent models participating in the AeroCom Phase-III project (Gliß et al., 2021). The amount of dust emissions and the dust lifetime in all NICAM simulations range within the uncertainty obtained from the AeroCom models. The difference in the dust column burden between NDW6 and NSW6 is 23%, which is

450   mainly caused by the 10% difference in emissions between NDW6 and NSW6 due to the difference in the simulated wind. Since the dust emission is approximately proportional to the cubic wind speed at a height of 10 m, only a 3.2% difference in the wind speed in the case of a 10 ms^{-1} average causes a 10% difference in the dust emission strength.

For sea salt, the differences in the column burden, emission, and lifetime among the NICAM simulations are not ~~so~~ as large and range within the uncertainty of the references. However, the emission flux of the NDW6-simulated sea salt is higher than

455   that of the NSW6-simulated sea salt, whereas the column burden of the NDW6-simulated sea salt is lower than that of the NSW6-simulated sea salt. This is mainly caused by the difference in wet deposition (see Appendix Table ~~A1~~ A2). The difference in wet deposition is strongly affected by the difference in the ratio of column precipitation to the sum of the column precipitation and column liquid cloud water (RPCW) between NDW6 and NSW6, as shown in Figure 5. The NDW6-simulated RPCW is larger than that of the NSW6 result, which is easy to see from the results of Figures 1 and 2. Because the NSW6-

460   simulated clouds are larger in most regions except for in the tropics, the NDW6-simulated RPCW is much closer to the CloudSat-retrieved RPCW. In the western Pacific Ocean over the tropics where the simulated aerosols are low, the NSW6 results are closer to the CloudSat results. An increase in the RPCW leads to an increase in the aerosols that are dissolved into ~~clouds, which fall to the ground as~~ rain-drops and are removed from the atmosphere. Therefore, NDW6-simulated clouds and precipitation cause more wet deposition of simulated aerosols compared to the NSW6 results.

465   Emissions of OM and BC are given from the database, so the differences in the column burden and lifetime are mainly discussed. The column burdens of the NDW6-simulated OM and BC, including water-soluble BC (WSBC) and water-insoluble BC (WIBC), are always lower than the NSW6 results. The lifetimes of the NDW6-simulated OM and BC are always shorter than those of the NSW6 results. The differences in the column burden as well as the lifetimes of OM and BC between NDW6 and NSW6 are at most 15%. All the results simulated by the NICAM are within the uncertainty of the AeroCom models but

470   are relatively lower than the medians and averages among the AeroCom models. The BC lifetimes are 5.4 days (NDW6) and 6.3 days (NSW6). They range from 2.9 days to 8.7 days (median 5.5 days) in the AeroCom models (Gliß et al., 2021). Sulfate is a secondary component and is formed from SO$_2$ oxidation in the atmosphere and within clouds. Its complexity results in different features from other primary species. The column burden of sulfate is 0.45 TgS (NDW6) and 0.52 TgS (NSW6). The results range from 0.22 TgS to 0.98 TgS (0.60 TgS at the median) in the AeroCom models (Gliß et al., 2021). The lifetimes

475 of sulfate are 2.9 days (NDW6) and 3.3 days (NSW6). They range from 1.8 days to 7.0 days (median 4.9 days) in the AeroCom models (Gliß et al., 2021). To understand the difference in the column burden and lifetime of sulfate between different schemes and resolutions, SO_2, as a precursor of sulfate, becomes an important factor. The column burden of NDW6-simulated SO_2 is 0.28 TgS, which is 1~~9~~6% lower than the NSW6 result. Therefore, the difference in the column burden of sulfate between NDW6 and NSW6 is mainly caused by the difference in the column burden of SO_2 because the difference is very small in the

480 wet deposition of sulfate between NDW6 and NSW6 (Table ~~A1~~A2). The difference in the column burden of SO_2 between NDW6 and NSW6 is caused by the chemical loss in the aqueous phase (0.~~7~~5 TgS yr^{-1} or +~~2~~1%) and gas phase (~~-~~1.~~1~~3 TgS yr^{-1} or -~~7~~10%) and wet deposition (0.~~4~~5 TgS yr^{-1} or +~~24~~23%), as shown in Table ~~A1~~A2. The differences between NSW6 and HRM are mentioned in Appendix A.

485 **3.3 Aerosol optical ~~products~~properties**

Figure 6 shows a global comparison of annual, January, and July averages of both NDW6- and NSW6-simulated AOTs with ground-based measurements (AERONET, SKYNET, and CARSNET). The model performance of both NDW6- and NSW6-simulated AOT is very good, with a high correlation (the PCC value is 0.662 to 0.807 in NDW6 and 0.721 to 0.837 in NSW6), moderate uncertainty (the RMSE value is 0.13 to 0.23 in NDW6 and 0.12 to 0.16 in NSW6), and moderate bias (the NMB

490 value is -24.1% to +27.5% in NDW6 and -8.9% to -5.0% in NSW6). These values are much better than those reported in Goto et al. (2020) (e.g., ~~the~~PCC value~~s~~ of 0.471 to 0.589, ~~the~~RMSE values of 0.21 to 0.23, and ~~the~~NMB value~~s~~ of -44.1% to -5.4%), as shown in Appendix B.

Figure 7 shows horizontal distributions of the annual averages in AOT in both NICAM simulations under all-sky and clear-sky conditions and satellite observations of MODIS and MISR onboard TERRA. Generally, both NDW6- and NSW6-

495 simulated AOTs are comparable to the satellite results. As shown in Figure 6, the NDW6-simulated AOT is lower than the NSW6 result. The AOT under all-sky conditions tends to be larger than the AOT under clear-sky conditions, mainly because the relative humidity (RH) under all-sky conditions is generally higher than the RH under clear-sky conditions (Dai et al., 2015). Over the outflow regions of North Africa over the Atlantic Ocean, both the NDW6- and NSW6-simulated AOTs are generally comparable to the satellite results. Over East China, Russia, and Central Asia, there are relatively large differences

500 among the NICAM-simulated, MODIS-retrieved and MISR-retrieved AOTs. As explained in section 2.2, over land such as East China, near the Arctic such as Russia, and in desert areas such as Central Asia, the MODIS-retrieved AOTs tend to be higher than the MISR-retrieved AOTs (Kahn et al., 2010; Shi et al., 2011; Petrenko and Ichoko, 2013). Over the Southern Ocean, where the MISR-retrieved AOT includes cloud contamination (Toth et al., 2013; Alfaro-Contreras et al., 2017), both the NDW6-simulated and NSW6-simulated AOTs are lower than the MISR-retrieved results and comparable to the MODIS-

505 retrieved results. The simulated AOT compositions are also compared with the references of the AeroCom models in Appendix C.

Figure 8 indicates the vertical profiles of the aerosol extinction coefficients in regional and annual averages. Since the CALIOP-retrieved results above a 5 km height include some bias (Watson-Parris et al., 2018), the discussion is focused on the results below a 5 km height. Large differences between NDW6 and NSW6 are found in South Asia (India and Southeast Asia), Africa (the coast of North Africa, North Africa, the coast of Central Africa, and South Africa), and South America, where the NDW6-simulated aerosols are lower than the NSW6-simulated results. In South Asia (Figures 8d and 8i), the vertical profiles of both NDW6- and NSW6-simulated aerosol extinction coefficients are comparable to the CALIOP-retrieved results with peak heights of 0.5-1 km. In East China (Figure 8e), the vertical profiles of both NDW6- and NSW6-simulated aerosol extinction coefficients are different from those obtained from CALIOP, which has low aerosols below 2 km height. These CALIOP (version 3) retrieval results may include biases because CALIOP (version 4) improved this underestimation in East China (Kim et al., 2018). Along the coast of North Africa, both NDW6- and NSW6-simulated aerosols are comparable to the CALIOP-retrieved results (Figure 8g), although in the dust source area in North Africa (Figure 8h), they are overestimated compared to the CALIOP-retrieved results. This may be one problem of CALIOP retrievals over desert areas where the assumed lidar ratio of pure dust is low (Schuster et al., 2012). In the biomass burning areas (the coast of central Africa, South America, and South Africa), as shown in Figures 8(j), 8(k), and 8(l), the heights at which the extinction coefficient decays (called 'decay height') in the CALIOP results are much more reliable than the vertical profiles of the CALIOP-retrieved extinction coefficient because ~~the~~ CALIOP cannot detect the signal below the optically thick layers (Ma et al., 2013). The decay heights of the NICAM-simulated extinction coefficients are lower along the coasts of central Africa and South Africa and higher in South America compared to the CALIOP results. This large bias of the vertical profile indicates a problem of the vertical transport of aerosols originating from biomass burning in the NICAM, which may not be solved by the improvement of the cloud microphysics module and finer resolution of the model grids. The differences between NSW6 and HRM are mentioned in Appendix B.

4 Radiative forcing

This section discusses the impacts of aerosols on radiation through ARI and ACI by comparing them with references obtained from both models and satellites. These comparisons verify the usefulness of the NICAM aerosol model coupled ~~to~~ with both the NDW6 and NSW6 modules for climate simulations.

4.1 Aerosol-Radiation Interaction (ARI)

Figure 9 shows the shortwave and longwave instantaneous radiative forcing of the ARI (IRFari) at the TOA and the surface in the NICAM and references (HRM and LRM in Goto et al., 2020; MACv2 in Kinne, 2019; observational estimates in Thorsen et al., 2021). The magnitudes of the IRFari values among all the NICAM-simulated dust values under both all-sky and clear-sky conditions at the TOA are larger than the reference results (Kinne, 2019). For example, the shortwave IRFari dust values at the TOA under all-sky conditions are calculated to be -0.46 Wm^{-2} (NDW6), -0.57 Wm^{-2} (NSW6), and -0.24 Wm^{-2} (Kinne, 2019). This is partly caused by the weaker absorption of AOT and the higher dust AOT in this study compared to the median

value of the AeroCom models, as shown in Figure C1. In contrast, at the surface, the magnitudes of ~~the~~ both shortwave and longwave IRFari values among all the NICAM-simulated dust values under both all-sky and clear-sky conditions are smaller than the results in Kinne (2019). This is consistent with too little shortwave absorption, but ~~This~~ this is inconsistent with the results of the larger column burden and AOT of dust in this study compared to those of the AeroCom models in Figures 4 and C1. The comparison with the results of Kinne (2019) may imply a much higher mass extinction coefficient of the dust or bias of the simulated dust size distribution, as noted by Kok et al. (2017), who concluded that the simulated dust in current global models is too fine. For other absorption components, i.e., POM+WSBC and WIBC, the NSW6-simulated IRFari values are higher than the NDW6 results. Under all-sky conditions, both NDW6- and NSW6-simulated IRFari values due to POM+WSBC and WIBC are positive because of an increase in absorption in the presence of clouds. At the surface, the difference in the IRFari values among all the NICAM simulations has the same tendency as that obtained from the difference in the column burden or AOT. For SOA, as the other component of carbonaceous aerosols and nonlight-absorbing matter, the difference in the IRFari values among all NICAM simulations generally has the same tendency as that obtained from the difference in carbonaceous aerosols. For other nonlight-absorbing components, i.e., sea salt and sulfate, the difference in the IRFari values between the ~~all-sky~~TOA and the ~~clear-sky conditions~~surface is very small. At the TOA and the surface, the magnitudes of the NDW6-simulated IRFari values in both shortwave and longwave under both the all-sky and clear-sky conditions are lower than those of the NSW6 results. This is consistent with the results of the column burden (Figure 4) and AOT (Figure C1). The shortwave IRFari values due to sea salt under all-sky conditions are estimated to be -0.56 Wm^{-2} (NDW6), -0.65 Wm^{-2} (NSW6), and -0.72 Wm^{-2} (Kinne, 2019). If the estimation by Kinne (2019) is assumed to be real, the NICAM-simulated AOT of sea salt is underestimated by 10-20%, probably because the NICAM underestimates the column burden of sea salt, which ~~can~~may be ~~caused~~due to ~~by~~its ~~lower~~short lifetime relative to the values from Kinne (2019)~~among the references~~ (Figure 4c). This may suggest that the NICAM-simulated sea salt is ~~more~~scavenged more by wet deposition, possibly due to high precipitation in the NICAM (Figure 1). For sulfate, the shortwave IRFari values under all-sky conditions are estimated to be -0.51 Wm^{-2} (NDW6), -0.60 Wm^{-2} (NSW6), and -0.83 Wm^{-2} (Kinne, 2019). This is consistent with the results of lower values of both the column burden and AOT of sulfate among the reference models (Figures 4b and C), which is caused by the lower lifetime of sulfate among the AeroCom models (Figure 4c).

Overall, the IRFari values due to all aerosols under all-sky conditions are estimated to be -1.57 Wm^{-2} (NDW6) and -1.86 Wm^{-2} (NSW6), -1.92 Wm^{-2} (from -3.1 Wm^{-2} to -0.61 Wm^{-2} in Thorsen et al., 2021), and -1.10 Wm^{-2} (Kinne, 2019). The magnitude of the IRFari by Kinne (2019) is lower than the other estimates because the light-absorbing effect is higher in this reference than in the others. The NSW6-simulated shortwave IRFari value is close to the reference value obtained from observational estimates in Thorsen et al. (2021) ~~by summarizing both satellite and model results~~, whereas the NDW6-simulated shortwave IRFari value is lower than the median value of ~~the references~~Thorsen et al. (2021) by approximately 0.4 Wm^{-2}. The differences in the IRFari values between NDW6 and NSW6 ~~is~~are 0.29 Wm^{-2}~~,~~ (shortwave), 0.03 Wm^{-2} (longwave), and 0.26 Wm^{-2} (sum of shortwave and longwave), ~~which~~which ~~is~~are approximately 16% (shortwave), 14% (longwave), and 16% (sum) of the total IRFari value in NDW6. For anthropogenic aerosols, the shortwave IRFari values under all-sky conditions are estimated to be

-0.38 Wm^{-2} (NDW6), -0.45 Wm^{-2} (NSW6), and -0.63 Wm^{-2} (from -0.11 Wm^{-2} to -1.00 Wm^{-2} in Thorsen et al., 2021). The difference in IRFari values between NDW6 and NSW6 is 0.07 Wm^{-2}~~,~~ (shortwave), 0.00 Wm^{-2} (longwave), and 0.06 Wm^{-2} (sum of shortwave and longwave), which is approximately 15% (shortwave), 3% (longwave), and 16% (sum) of the total IRFari value in NDW6. The magnitudes of both NDW6- and NSW6-simulated shortwave IRFari values range within the uncertainty but are lower than the median of Thorson et al. (2021). This difference in the total IRFari between NDW6 and NSW6 is caused by the difference in the simulated dust, sea salt and sulfate, as shown in section 3. The difference between NICAM and the reference is mainly attributed to the lower value of the column burden of the simulated sulfate. In conclusion, the magnitudes of both the NDW6- and NSW6-simulated IRFari values are within the uncertainty of the references, even if the uncertainty is caused by the assumption in the preindustrial days, as mentioned in section 2.3. ~~and t~~The difference in the IRFari values between NDW6 and NSW6 is up to 20%. In addition, the difference in the IRFari values between NDW6 and NSW6 is larger than the difference between the HRM and LRM in Goto et al. (2020), as mentioned in Appendix D. Therefore, the model development of the cloud microphysics module is important.

Figure 10(a) and Table 2 show~~s~~ the global and annual mean ~~IRFari~~ ERFari values due to anthropogenic aerosols. The NICAM-simulated ~~IRFari~~ ERFari values (-0.~~22~~19 Wm^{-2} in NDW6 and -0.~~26~~23 Wm^{-2} in NSW6) ~~range around the upper limit of the references (-0.25 Wm^{-2}), including both the satellite observations and models in Thorsen et al. (2021), but~~ are comparable to the value of -0.25 Wm^{-2} (-0.45 Wm^{-2} to -0.05 Wm^{-2}) shown in IPCC-AR6 (Forster et al., 2021). The NICAM-simulated shortwave ERFari values (-0.22 Wm^{-2} in NDW6 and -0.26 Wm^{-2} in NSW6) are slightly underestimated compared to the references (-0.25 Wm^{-2}) provided by the observational estimates in Thorsen et al. (2021), given the uncertainties for preindustrial emissions in this study. The difference between NDW6 and NSW6 is calculated to be 0.04 Wm^{-2} (approximately 16%). ~~This is because the IRFari values due to anthropogenic aerosols exclude dust, for which there is a relatively large difference between NDW6 and NSW6.~~ Under clear-sky conditions, the NICAM-simulated values (-0.52 Wm^{-2} in NDW6 and -0.60 Wm^{-2} in NSW6) in shortwave are smaller in magnitude than the lower limit of the references (-0.67 Wm^{-2}) in Thorsen et al. (2021). The difference between NDW6 and NSW6 is calculated to be 0.08 Wm^{-2} (approximately 13%). Even in the net, i.e., sum of shortwave and longwave, the NICAM-simulated values are -0.47 Wm^{-2} in NDW6 and -0.55 Wm^{-2} in NSW6, and the calculated difference between NDW6 and NSW6 is 0.08 Wm^{-2} (approximately 13%). In summary, ~~The~~ the difference in the ~~anthropogenic I~~ERFari values between NDW6 and NSW6 is up to 15% or 0.08 Wm^{-2}.

4.2 Aerosol-Cloud Interaction (ACI)

Before evaluating the simulated radiative forcings due to ACI, the simulated cloud radiative forcing (CRF) and total radiation fluxes are compared and evaluated~~for model evaluations of radiation budget~~. As shown in Table 1~~2~~, the global ~~and January~~ averages of the SWCRF for January are estimated to be -48.4 Wm^{-2} (NDW6), -49.3 Wm^{-2} (NSW6), and -50.4 Wm^{-2} (CERES), whereas the global ~~and July~~ averages of the SWCRF for July are estimated to be -41.8 Wm^{-2} (NDW6), -48.7 Wm^{-2} (NSW6), and -44.5 Wm^{-2} (CERES). The difference in the SWCRF between NDW6 and NSW6 is 0.9 Wm^{-2} in January and 6.9 Wm^{-2} in July. The difference in the SWCRF between NICAM and CERES in January is 2.0 Wm^{-2} (NDW6) and 1.1 Wm^{-2} (NSW6),

whereas the difference in the SWCRF between NICAM and CERES in July is 2.7 Wm^{-2} (NDW6) and -4.2 Wm^{-2} (NSW6). At 30°S-30°N latitudes and in annual averages, the NDW6-simulated SWCRF values are underestimated compared to the CERES results, whereas the NSW6-simulated SWCRF values are overestimated and more comparable to the CERES results. At other latitudes and in annual averages, the NDW6-simulated SWCRF is comparable to the CERES results, whereas the NSW6-simulated SWCRF values are underestimated compared to the CERES result. The global and annual averages of ~~the~~ SWCRF are estimated to be -42.5 Wm^{-2} (NDW6), -45.9 Wm^{-2} (NSW6), and -45.7 Wm^{-2} (CERES). The NSW6-estimated SWCRF value is highly comparable to the CERES result but includes large compensation errors in the ~~spatiotemporal~~regional distribution. The details of the spatiotemporal characteristics are discussed in Appendix E. The NDW6-estimated SWCRF values are concluded to be better than the NSW6 results~~.~~, but the underestimation of the simulated SWCRF can have an impact on the aerosol simulations. The underestimation of the simulated SWCRF indicates the underestimation of the simulated LWP and/or the overestimation of the simulated CDR. When the simulated LWP is underestimated, the simulated aerosols are also underestimated, because the simulated precipitation is generally comparable to the observations in this study, as shown in Figure 1. When the simulated CDR is overestimated, the simulated CCN must be underestimated. This is consistent with the underestimation of the simulated aerosol. Therefore, if the negative biases in the simulated SWCRF are eliminated, the simulated aerosols will increase. For OSR, OLR, and LWCRF, the validation using CERES results is also shown in Appendix E. The underestimation of the simulated LWCRF is caused by the underestimation of the simulated high-level clouds, but the impacts of this negative biases in the simulated LWCRF on the aerosol simulations are unclear due to ignorance of the interaction between aerosols and ice crystals (as ice nuclei) in this model.

Given the verification of the NICAM-simulated ~~SW~~CRF above, the simulated ACI due to anthropogenic aerosols is discussed by comparing the results between NDW6 and NSW6 for simulations with aerosol and precursor gas emissions for ~~under~~ the preindustrial (PI), mentioned in section 2.3, and the present day (PD) ~~in Figure 10(b)~~. Figure 11 shows the global maps of changes in the simulated CCN at 1-km heights, CDNC at 1-km heights only for NDW6, CDR at 1-km heights~~AOT~~, LWP~~-~~, CA, CF at 1-km height and ~~shortwave~~ net ERFaci between PD and PI. ~~Table~~ Figure ~~3~~ 12 also shows the average values of th~~ose global and~~e selected regions. ~~These show global and annual mean values of effective radiative forcing for aerosol-cloud interactions (ERFaci) due to anthropogenic aerosols. The global annual averages of the ERFaci value are estimated to be -1.34 Wm^{-2} (NDW6) and -0.63 Wm^{-2} (NSW6). Both NDW6- and NSW6-estimated ERFaci values range within the results in IPCC-AR6 (Forster et al., 2021), i.e., -0.84 Wm^{-2} (-1.45 Wm^{-2} to -0.25 Wm^{-2}), but only NDW6-estimated ERFaci values exceeds the results in the Radiative Forcing Model Intercomparison Project (RFMIP) (Smith et al., 2020), i.e., -0.81±0.30 Wm^{-2}. The magnitude of the ERFaci value in NDW6 is larger than that in NSW6 by 0.72 Wm^{-2} (approximately 53% of the ERFaci value in NDW6), whereas the NDW6-simulated aerosol loadings are smaller than the NSW6 results, as shown in the previous sections. The difference in the ERFaci between NDW6 and NSW6 may be partly explained by a nonlinear relationship of the ERFaci to AOT under the different LWPs, as proposed by Carslaw et al. (2013) who argued that even if the aerosol difference between PI and PD is similar, the value of ERFaci can be larger when the aerosol concentration is lower. The NDW6-simulated AOT is lower than the NSW6-simulated results by 20%, as shown in Figure C1.~~ These figures show that the global average of

the NDW6-calculated ∂CCN at a 1-km height is estimated to be 16.70 cm^{-3} (∂CCN), whereas that in NSW6 is estimated to be 19.59 cm^{-3} (∂CCN). The NDW6-calculated ∂CCN values are lower than the NDW6 results. In ∂CDNC, the NDW6-estimated values are +0.70 cm^{-3} (global), +4.22 cm^{-3} (the United States), +4.58 cm^{-3} (Europe), +3.57 cm^{-3} (East Asia), and +0.34 cm^{-3} (India). However, the CDNC used in NSW6 is equal to the CCN concentrations due to the ignorance of sink process in the CDNC in NSW6, as mentioned in section 2.1, so the difference in ∂CDNC between NDW6 and NSW6 is very large. As a result, the NSW6-simulated ∂CDR values at the 1-km height are much larger than the NDW6 results. The NDW6-estimated ∂CDR is -0.17 µm (global), -0.64 µm (the United States), -0.55 µm (Europe), -0.91 µm (East Asia), and -0.33 µm (India), whereas the NSW6-estimated ∂CDR is -0.34 µm (global), -0.93 µm (the United States), -0.91 µm (Europe), -1.20 µm (East Asia), and -0.81 µm (India). As shown in Figure 11, the NDW6- and NSW6-estimated ∂CDR values are negative near the industrial regions where the ∂CCN is large. Therefore, the approximately 15% difference in ∂CCN between NDW6 and NSW6 causes the approximately 50% difference in ∂CDR. This indicates that the Twomey effect, i.e., the response of ∂CDR to ∂CCN, in NSW6 is larger than that in NDW6.

To evaluate the Twomey effect in NDW6 and NSW6, the global averages of differences in the mixing ratios and number concentrations for clouds between the PD and PI aerosol conditions are plotted in Figure 13. The changes in ∂Qc in both NDW6 and NSW6 are positive at most heights, so Qc increases as aerosols increase. This is consistent with the results of ∂LWP shown in Figures 11 and 12(e). The largest value of ∂Qc in both NDW6 and NSW6 occurs at a height of approximately 1.5 km, but the largest values in NDW6 are distributed up to a height of 2 km. Above a height of 3 km, ∂Qc in NDW6 is positive, whereas ∂Qc in NSQ6 is close to zero or negative. This difference in ∂Qc between NDW6 and NSW6 is possibly caused by the differences in the simulated supercooled liquid water in mixed-phase clouds, as mentioned in section 3.1. For ∂CDNC, the largest values in NDW6 occur at a height of 1.2 km, which is slightly lower than the height where the largest value of ∂Qc occurs. This reflects the vertical structure of typical clouds in NDW6. In contrast, the vertical profile of ∂CDNC in NSW6 is different from that of ∂Qc because NSW6 cannot predict CDNC and adopts ∂CCN. This implies that ∂CDR is anti-proportional to ∂Qc from the surface to the 4-km height and has a low value below the 1.5-km height and the largest value at a height of approximately 1.5 km. Specifically, above a height of 3 km, where ∂Qc is close to zero and ∂CDNC has a positive value, ∂CDR should be small. The possible overestimation of ∂CDR in NSW6 represents possible overestimation of the Twomey effect in NSW6.

As mentioned above, the NDW6-calculated ∂LWP values are higher than the NSW6 results by three times in global averages. The NDW6-estimated values are +2.12 g m^{-2} (global), +7.52 g m^{-2} (the United States), +15.45 g m^{-2} (Europe), +8.77 g m^{-2} (East Asia), and +3.36 g m^{-2} (India), whereas the NSW6-estimated values are +0.65 g m^{-2} (global), +4.96 g m^{-2} (the United States), +2.52 g m^{-2} (Europe), +2.62 g m^{-2} (East Asia), and -0.44 g m^{-2} (India). The positive values in ∂LWP in both NDW6 and NSW6 could be caused by a decrease in auto-conversion due to the increase in CDNC. However, magnitudes of ∂LWP differ between NDW6 and NSW6, which is the largest in Europe among others, whereas the NDW6- and NSW6-simulated ∂CCN are close to each other in most regions. This appears to indicate that the cloud water susceptibility, defined as the difference in ∂LWP against ∂CCN from PD to PI conditions, is larger in NDW6 than in NSW6. Such a different susceptibility

could be interpreted in terms of different complexities of hydrometeors interactions between NSW6 and NDW6, particularly whether or not the CDNC and rain drop number concentration (RDNC) are predicted. This generates different variabilities of CDNC and RDNC between the two schemes, possibly leading to the different susceptibilities. Nevertheless, more detailed analysis will be required in future studies to explore microphysical processes responsible for these different behaviors between the two schemes.

~~Figure 11 shows that t~~The horizontal distribution of changes in the simulated ~~LWP~~ ERFaci is generally consistent with changes in the simulated ∂~~ERFaci~~LWP (Figure 11). By decreasing the simulated ∂CDR, increasing the simulated ∂LWP from PI to PD, and increasing the simulated ∂CA and ∂CF at 1-km height, the negative values of the simulated ERFaci in ~~the~~ industrial regions, such as the United States, Europe, and East Asia, increase in magnitude. The global annual averages of the net ERFaci value are estimated to be -1.28 Wm^{-2} (NDW6) and -0.73 Wm^{-2} (NSW6). Both NDW6- and NSW6-estimated ERFaci values range within the results in IPCC-AR6 (Forster et al., 2021), i.e., -0.84 Wm^{-2} (-1.45 Wm^{-2} to -0.25 Wm^{-2}), and the Radiative Forcing Model Intercomparison Project (RFMIP) (Smith et al., 2020), i.e., -0.81±0.30 Wm^{-2}, by considering the uncertainty caused by the assumption in the PI conditions. The magnitude of the ERFaci value in NDW6 is larger than that in NSW6 by 0.55 Wm^{-2} (approximately 43% of the ERFaci value in NDW6), whereas the NDW6-simulated aerosol loadings are smaller than the NSW6 results, as shown in the previous sections. ~~Table~~ Figure ~~3~~ 12 shows that the negative NDW6-estimated ERFaci value~~s~~ ~~is~~ are larger ~~negatively~~ than the NSW6-estimated ERFaci values by ~~0.72 Wm^{-2} (Global), 1~~2.~~23~~33 Wm^{-2} (US), 4~~3~~.~~24~~22 Wm^{-2} (Europe), 1.~~57~~10 Wm^{-2} (East Asia), and 0.~~87~~89 Wm^{-2} (India). Therefore, it was suggested that the ERFaci due to the cloud lifetime effect in NDW6 was larger than that in NSW6 due to the Twomey effect, although the NSW6-simulated ERFaci certainly includes some bias due to the overestimation of the Twomey effect. ~~The difference in the simulated susceptibility, defined as a difference in the LWP change against the aerosol change from PD to PI, between NDW6 and NSW6 is key to understand the difference in the ERFaci. Sato et al. (2018) showed that the NICAM coupled to NSW6 at a 14 km grid spacing generally succeeds in reproducing the satellite-retrieved susceptibility on a global scale. The satellite-retrieved susceptibilities are generally negative over ocean and positive over the industrial areas, such as the United States, Europe, and East Asia. In these industrial areas, the NSW6-simulated susceptibilities tend to be negative, whereas the NDW6 results tend to be positive and consistent with satellite results. In India, the difference in the ERFaci between NDW6 and NSW6 is smaller than those in the other industrial areas, probably because both the NDW6- and NSW6-simulated susceptibilities are negative or slightly positive. Notably, the reason for the differences in the susceptibility between NDW6 and NSW6 should be addressed in future studies.~~

Other possible reasons for the differences in the ERFaci between NDW6 and NSW6 are discussed. Carslaw et al. (2013) and Wilcox et al. (2015) pointed out that the different baselines of aerosol fields can provide small differences in ERFaci between two simulations. As mentioned in the previous sections for aerosols, the NDW6-simulated aerosols are generally lower than the NSW6 results, for example IRFari is approximately 15% lower. However, the baseline of CCN at 1-km height between NDW6 and NSW6 under the PI conditions is not very different, so the difference in the baseline of aerosols between NDW6 and NSW6 does not cause the difference in ERFaci between the two simulations.

The difference in the autoconversion from clouds to precipitation between NDW6 and NSW6 can be a reason for the difference in ERFaci between NDW6 and NSW6. Using a global aerosol model, MIROC, coupled to a double-moment bulk cloud microphysics scheme with coarse resolution of 1.4° × 1.4°, the difference in ERFaci between Khairoutdinov and Kogan (2000) and Seifert and Beheng (2006) is estimated to be 0.15 Wm^{-2} (Michibata and Suzuki, 2020). This magnitude of ERFaci difference potentially caused by the two different autoconversion schemes cannot explain the difference in ERFaci between NDW6 and NSW6 of this study.

5 Summary

To estimate the impacts of cloud microphysics modules on aerosols and their radiative forcing, 6-year simulations of aerosols are performed using two different types of cloud microphysics schemes, i.e., the double-moment bulk cloud microphysics module (NDW6) and the single-moment bulk module with 6 water categories (NSW6), in the NICAM at a 14 km grid spacing. The previous study ~~of~~ by Goto et al. (2020) also simulated aerosols at a 14 km grid spacing. The NICAM used in this study was updated from our previous study of Goto et al. (2020), which also simulated aerosols at a 14 km grid spacing in terms of the cloud microphysics module (from NSW6 to NDW6), the vertical resolution (from 38 layers to 78 layers) and some aerosol modules (sulfate and dust).

The model performance of the surface aerosol mass concentrations and AOT are evaluated with in situ measurements by statistical metrics of correlation (PCC), bias (NMB), and uncertainty (RMSE). The model performances of both NDW6-simulated surface mass and NSW6-simulated surface mass as well as AOT are very good, with moderate to high correlation, low to moderate uncertainty, and low to moderate bias. The differences between NDW6 and NSW6 are small, but they are greatly improved from the previous study of Goto et al. (2020). For example, the PCCs between the simulated and observed AOTs in annual averages are 0.807 (NDW6) and 0.837 (NSW6), which are much higher than 0.471 (HRM) and 0.356 (LRM) in Goto et al. (2020). The reason for these ~~performance~~ improvements in this study is not only the update from Goto et al. (2020) but also the increase in available computational resources (using the supercomputer Fugaku in this study), resulting in approximately 12 times faster computation time than the supercomputer K in Goto et al. (2020).

The NDW6-simulated aerosol distributions are generally lower than the NSW6 results. For example, the global and annual mean values of the simulated AOT under all-sky conditions are estimated to be 0.127 (NDW6) and 0.153 (NSW6), which range within the model uncertainty of the AeroCom models. These differences among the NICAM experiments with different cloud microphysics modules, i.e., NDW6 and NSW6, are caused by a different ratio of column precipitation to the sum of the column precipitation and column liquid cloud water or RPCW, which strongly determines the wet deposition in the aerosols. Since the NDW6-simulated LWP is generally lower than the NSW6 result and the NDW6-simulated precipitation is generally comparable to the NSW6 result, the scavenging effect of the aerosols in NDW6 is larger than that in NSW6. The NDW6-simulated RPCW, precipitation and LWP are generally closer to the satellite-retrieved results compared to the NSW6 result,

although their global and annual mean values in NDW6 are sometimes no closer to the observation than the NSW6 results due to compensation errors in ~~time and~~ space.

The differences in the dust emissions, dust column burden and SO_2, AOT, and IRFari values for total aerosols between NDW6 and NSW6 are larger than those in the other aerosol budgets and components. For example, the net IRFari values due to all aerosols under all-sky conditions are estimated to be -1.~~57~~36 Wm^{-2} (NDW6), -1.~~86~~62 Wm^{-2} (NSW6), and -1.92 Wm^{-2} (from -3.1 Wm^{-2} to -0.61 Wm^{-2} in Thorsen et al., 2021). The difference in IRFari values between NDW6 and NSW6 is 0.~~29~~26 Wm^{-2}, which is at most 20% of the total IRFari value in NDW6. The ERFari values due to anthropogenic aerosols under all-sky conditions are estimated to be -0.19 Wm^{-2} (NDW6), -0.23 Wm^{-2} (NSW6), and -0.25 Wm^{-2} (-0.45 Wm^{-2} to -0.05 Wm^{-2}) shown in IPCC-AR6 (Forster et al., 2021). The difference between the NICAM and the reference may be larger, given the uncertainties in the preindustrial emissions in this study. The ~~large~~ difference in NDW6 and NSW6 is probably caused by the difference in the simulated dust and sulfate in the present study, as shown in section 3. The difference in the dust between NDW6 and NSW6 is mainly caused by the difference in the emission fluxes due to the difference in the simulated wind, whereas those in the sulfate are mainly caused by the differences in the wet deposition of SO_2. A large difference among the experiments is also found in the interaction between aerosols and clouds, ERFaci, in which the global annual mean values in the net are estimated to be -1.~~34~~28 Wm^{-2} (NDW6) and -0.~~63~~73 Wm^{-2} (NSW6). The difference in the net ERFaci values between NDW6 and NSW6 is 0.~~72~~55 Wm^{-2} (approximately ~~53~~43% of the ERFaci value in NDW6). This difference is larger than ~~those~~ that in ~~the IRFari~~ERFari, which is ~~up to 15~~approximately 20% or 0.~~08~~04 Wm^{-2}. The regional differences in ERFaci between NDW6 and NSW6 are found to be large in the industrial areas, where the NDW6-simulated ERFaci values are negatively larger than the NSW6-simulated results. These differences are mainly caused by the difference in the susceptibility of the ∂LWP to ∂~~AOT~~CCN ~~and partly due to a nonlinear relationship between the ERFaci and AOT under different AOTs, a.~~ As discussed in section 4.~~2~~, it was suggested the increase in changes in ERFaci due to the cloud lifetime effect in NDW6 is larger than that in NSW6 due to the Twomey effect, although the NSW6-simulated ERFaci certainly includes some bias due to the overestimation of the Twomey effect. The different susceptibility between NDW6 and NSW6 could be interpreted in terms of different complexities of hydrometeors interactions between NSW6 and NDW6, particularly whether the CDNC and RDNC are predicted. This generates different variabilities of CDNC and RDNC between the two schemes, possibly leading to the different susceptibilities. Nevertheless, more detailed analysis will be required in future studies to explore microphysical processes responsible for these different behaviors between the two schemes.

Other possible reason for the differences in the ERFaci between NDW6 and NSW6 is the different baselines of aerosol fields, as suggested by Carslaw et al. (2013) and Wilcox et al. (2015), but this is minor because the baseline of CCN at 1-km height between NDW6 and NSW6 under the PI conditions is not very different. Another possible reason is the difference in the autoconversion between NDW6 and NSW6, and the difference in ERFaci between Khairoutdinov and Kogan (2000) and Seifert and Beheng (2006) is estimated to be 0.15 Wm^{-2} by using a general circulation model MIROC (Michibata and Suzuki, 2020). However, this magnitude of ERFaci difference potentially caused by the two different autoconversion schemes cannot explain the difference in ERFaci between NDW6 and NSW6 of this study. As mentioned in section 2.3, the assumption of the

preindustrial conditions for aerosols can cause possible differences in the aerosol radiative forcing due to the anthropogenic sources between this study and other studies, such as IPCC-AR6 (Szopa et al., 2021). This study assumes that the anthropogenic emission fluxes of BC, OC and SO_2 are zero in the preindustrial conditions, whereas other studies often use them in 1750 or 1850 provided by Hoesly et al. (2018). Using the results of MIROC by Takemura (2020), the possible difference in the aerosol radiative forcing due to the anthropogenic source will be at most 0.05 Wm^{-2} (IRFari) and 0.2 Wm^{-2} (ERFari plus ERFaci).

In climate simulations, the simulated radiation fluxes, i.e., SWCRF and OSR, are important. Although there are compensation errors in the spatiotemporalregional distribution, the differences in the global and annual averages between NICAM (NDW6 and NSW6) and CERES are estimated to be at most 3.2 Wm^{-2} (SWCRF and OSR). For longwave radiation, which is not the specific focus of this study, the differences in the global and annual averages between NICAM (NDW6 and NSW6) and CERES are estimated to be at most 6.4 Wm^{-2} (LWCRF) and at most 3.4 Wm^{-2} (OLR). These biases in the radiation fluxes between NICAM and CERES are acceptable for a climate model, but the negative biases of SWCRF and LWCRF may cause the underestimation of aerosols and the overestimation of the net ERFaci, respectively.

In conclusion, the NICAM at a 14 km grid spacing with both the NDW6 and NSW6 cloud microphysics modules for 6 years generally successfully reproduces the observed aerosols. The NDW6-simulated RPCW, precipitation and LWP are generally closer to the satellite-retrieved results compared to the NSW6 result. The cloud microphysics representation of NDW6 is more elaborate than that of NSW6, and it found that the NSW6-simulated CDR is overestimated due to the inability to predict CDNC in NSW6. and thusTherefore, the use of NDW6 is recommended in environmental and climate simulations. At the same time, because the ERFaci in NDW6 needs validation, in the future it will be necessary to perform additional experiments targeting specific cases of volcano in Iceland shown in Malavelle et al. (2017) to deeply evaluate the model results in NDW6.However, because simulations using NDW6 require 1.5 times more calculation resources, the use of NSW6 is still useful for long-period climate simulations at high resolutions.

Appendix A: Comparisons in of the aerosol mass loading between NSW6 in this study and the results in Goto et al. (2020)

As shown in sections 3.2 and 3.3, the evaluation is performed using statistical metrics: the Pearson correlation coefficient (PCC), normalized mean bias (NMB), and root-mean-square error (RMSE). These metrics using the concentration (C) of the observation (*obs*) and the simulation (*sim*) and the sampling number (N) are defined as follows:

$$PCC = \frac{\sum(C_{obs}-\overline{C_{obs}})(C_{sim}-\overline{C_{sim}})}{\sqrt{\sum(C_{obs}-\overline{C_{obs}})^2\sum(C_{sim}-\overline{C_{sim}})^2}} \tag{A1}$$

$$NMB = \frac{\sum(C_{sim}-C_{obs})}{\sum(C_{obs})} \times 100[\%] \tag{A2}$$

$$RMSE = \sqrt{\frac{\sum(C_{sim}-C_{obs})^2}{N}} \tag{A3}$$

805   For the mass loading of OM, the statistical metrics obtained in this study are greatly improved compared to the previous study using NICAM.16 (e.g., PCC ~~or~~ of 0.~~847~~819, RMSE of ~~35.40~~03, and NMB of ~~-29~~54.9 ~~-8~~ μg m^{-3} from Goto et al., 2020), as shown in Table A1. For BC in Table A1, the statistical metrics in this study are not improved from Goto et al. (2020). For sulfate in Table A1, the values of the PCC and RMSE in this study are close to those in Goto et al. (2020), but the NMB in this study is much lower. Therefore, the model performance for surface aerosol mass concentrations in this study is apparently

810   improved by modifying the sulfur module, as described in section 2.2.

Global and annual mean values of column burden, emission, and atmospheric lifetime are also compared to the results of Goto et al. (2020), as shown in Table A2~~1~~. The difference in the dust emission and its column burden among different cloud microphysics modules, i.e., between NDW6 and NSW6, is larger than that among different horizontal resolutions, i.e., between the HRM (14 km) and LRM (56 km). The dust lifetime in this study is shorter than that in Goto et al. (2020). The difference

815   is probably caused by the difference in the dust emission scheme, as described in section 2.2. ~~Surely~~In support of this, the global climate model MIROC uses the same dust emission scheme as in this study and has a shorter lifetime among the AeroCom models (Gliß et al., 2021). The decrease in the number of bins from 10 to 6 may reduce the variability of the particle size distribution, move the center of the particle size distribution to coarser sizes, lead to an increase in the amount of deposition, and then reduce the lifetime. For sea salt, the difference in the emissions between NSW6 in this study and the HRM in Goto

820   et al. (2020) is approximately 11%. This causes the difference in the column burden, although the difference in the lifetime between this study and Goto et al. (2020) is small. For OM and BC, the differences in NSW6 and HRM are small and within the AeroCom models (Gliß et al., 2021).

For sulfate, the column burden is 0.52 TgS (NSW6), 0.38 TgS (HRM) and 0.32 TgS (LRM), which are within the uncertainty among AeroCom models (Gliß et al., 2021). The lifetimes of sulfate are 3.3 days (NSW6), 2.4 days (HRM) and 2.1 days

825   (LRM), which are also within the variability among the AeroCom models (Gliß et al., 2021). The difference in the sulfate column burden between NSW6 and the HRM is larger than the difference among cloud microphysics modules and different horizontal resolutions. This is attributed to a change in the assumption that sulfate forms in clouds by aqueous-phase oxidation, as described in section 2.2. The difference in the column burden of the simulated sulfate among cloud microphysics modules is comparable to that among different horizontal resolutions. For SO$_2$, the column burden of the simulated SO$_2$ is 0.33 TgS

830   (NSW6), 0.33 TgS (HRM), and 0.31 TgS (LRM). Therefore, the difference in the horizontal distribution affects SO$_2$ oxidation and then the column burden of sulfate, whereas the difference in the cloud microphysics module does not affect the chemical budget of SO$_2$ oxidation.

Appendix B: Comparisons in the AOT between NSW6 in this study and the results in Goto et al. (2020)

The scatterplots of the simulated AOT and the ~~surface~~ground-based -observed AOT are shown in Figure 6 in this study and

835   Figure 6 in Goto et al. (2020). The statistical metrics in this study (both NDW6 and NSW6) are much better than those reported in Goto et al. (2020). The PCC value improved from 0.471 (HRM) to 0.837 (NSW6), the RMSE value improved from 0.21 (HRM) to 0.12 (NSW6), and the NMB value improved from -20.2% to -5.4%. In the horizontal distribution of the AOT shown

in Figure 7, especially over the Southern Ocean, the NSW6-simulated AOT is greatly improved from the results of Figure 5 in Goto et al. (2020). This means that an AOT larger than 0.3 was frequently observed in past NICAM simulations. Over heavy

840 AOT areas, for example, in the Sichuan Basin located in ~~southwest~~ Southwest China and the Indo-Gangetic Plain, the NSW6-simulated AOT is generally more comparable to the satellite-retrieved AOTs compared to the results in the HRM in Goto et al. (2020). The improvement in these areas is caused by the increased number of vertical layers below 2 km height from 10 to 15 in this study, as described in section 2.1. The higher vertical resolution causes better performance of the simulated aerosols in the boundary layer by suppressing the artificial dispersion and diffusion of the aerosols near the surface on the basin. This

845 change can be found in not only the AOT but also the column burden and the surface mass concentrations of the aerosols.

At the end of section 3.3, the vertical profiles of the simulated aerosol extinction coefficients are evaluated by the CALIOP retrieval results (Figure 8). Due to the increase in the vertical layer from Goto et al. (2020) to the present study, any improvements in the vertical profiles of the simulated aerosols between NSW6 and the HRM are expected to be large, but drastic changes are not found in most regions. Large differences in the vertical profile are found in East China (Figure 8e), the

850 coast of East Asia (Figure 8f), and Southeast Asia (Figure 8i). Along the coast of East Asia, for example, the decay height of the CALIOP-retrieved extinction coefficients is approximately 0.5 km, whereas the decay height of the NSW6-simulated extinction coefficients is approximately 1 km and that of the HRM-simulated extinction coefficients is zero. In this area, the NSW6-simulated results are improved ~~from~~ over the HRM-simulated results. In dusty regions such as the coast of northern Africa (Figure 8g) and northern Africa (Figure 9h), the differences in the aerosol profiles between NSW6 and the HRM are

855 small, even though the dust schemes used in NSW6 are different from those in the HRM, as described in section 2.2. Along the coast of central Africa and over South America, both NSW6- and HRM-simulated results still include biases in the vertical profiles. As mentioned in section 3.3, this bias indicates a problem of the vertical transport of aerosols originating from biomass burning in the NICAM, which may not be solved by the finer vertical and horizontal resolutions.

Appendix C: Comparisons of the AOT components between the NICAM and AeroCom models

860 The simulated AOT compositions are compared with the references of the AeroCom models (Gliß et al., 2021) in Figure C1. All the NICAM-simulated dust AOTs are larger than those obtained from the AeroCom models. Since the column loadings of both the NDW6- and NSW6-simulated dust ranges are within the uncertainty among the AeroCom models shown in Figure 4, the dust treatment updates, especially the reduction in the number of bins for dust, may result in a higher mass extinction coefficient of the dust. The uncertainty of the dust AOTs among the AeroCom models is lower than that of other AOTs,

865 probably because the AeroCom models in dusty areas must be tuned by modifying dust emissions to become closer to the satellite results. All the NICAM-simulated sea salt AOTs range within the uncertainty of the AeroCom models, but the mass extinction coefficient of the sea salt tends to be higher than that of the AeroCom models since the column burden of the NICAM-simulated sea salt is lower than that of the AeroCom models. For carbon and sulfate, all the NICAM-simulated AOTs range within the uncertainty of the AeroCom models. For total species, the NICAM-simulated AOTs, except under NDW6

870 and clear-sky conditions, are larger than the upper range among the AeroCom models. The NDW6-simulated AOTs and the

NSW6-simulated AOTs under only clear-sky conditions are close to the median values of the AeroCom models but lower than the averages obtained from the ground-based AERONET measurements and satellites in Figure 3 of Gliß et al. (2021). The NDW6- and NSW6-simulated absorption AOTs also range within the uncertainty of the AeroCom models (Sand et al., 2021) but are lower than the median value of the AeroCom models.

875 Appendix D: Comparisons ~~in~~ of the shortwave IRFari between NSW6 in this study and the results in Goto et al. (2020)

As shown in Figure 9, the NSW6-estimated IRFari values are compared with the HRM-estimated values and references. Generally, the differences in the IRFari values between NSW6 and HRM are similar ~~tendencies~~ to those in the column burden. After the improvement of increased vertical levels and ~~updates~~ updated aerosol modules, the IRFari values at TOA are changed by +0.27 Wm^{-2} (dust), -0.13 Wm^{-2} (~~Seasalt~~seasalt), -0.01 Wm^{-2} (WSBC+POM, i.e., BC-containing particles), +0.04 Wm^{-2}
880 (SOA, i.e., pure OM), +0.03 Wm^{-2} (WIBC, i.e., pure BC), -0.14 Wm^{-2} (sulfate), -0.11 Wm^{-2} (only anthropogenic aerosols), and +0.08 Wm^{-2} (all aerosols). At the surface, the IRFari values are changed by +0.45 Wm^{-2} (dust), -0.14 Wm^{-2} (~~Seasalt~~seasalt), -0.08 Wm^{-2} (BC-containing particles), +0.03 Wm^{-2} (SOA), -0.04 Wm^{-2} (pure BC), -0.12 Wm^{-2} (sulfate), +0.08 Wm^{-2} (only anthropogenic aerosols), and -0.25 Wm^{-2} (all aerosols). The differences in the IRFari magnitude between NSW6 and HRM are generally higher than those among the different cloud microphysics modules (NDW6 and NSW6) and the different horizontal
885 resolutions (HRM and LRM).

For IRFari, due to changes in aerosols from the preindustrial era and the present era, the difference~~s~~ in NSW6 and HRM is +0.03 Wm^{-2} (all-sky) and -0.03 Wm^{-2} (clear-sky), respectively (see Figure 10). Under ~~the~~ all-sky condition~~s~~, the difference in the anthropogenic IRFari values between NSW6 and HRM is the largest, whereas under ~~the~~ clear-sky condition~~s~~, the difference in the values between NDW6 and NSW6 is the largest among these differences. This result is mainly caused by the increase
890 in the simulated sulfate in the present study, as shown in Appendix A.

Appendix E: Evaluation of total radiative fluxes in NICAM

Figure E1 illustrates the horizontal distribution of the NDW6- and NSW6-simulated and CERES-retrieved SWCRF as annual, January, and July averages. Over the Southern Ocean in January and the North Pacific and Atlantic Oceans in July, the magnitudes of the SWCRF values are larger than those in other areas and seasons. In these areas, the NDW6-simulated SWCRF
895 values over the Southern Ocean are closer to the CERES results, whereas the NSW6 results are lower than the CERES results. These results are very consistent with the LWP results, as shown in Figure 2. Over southern China, the eastern US, Europe, central Africa, and the coast of Mexico in January and central Africa, the central Pacific Ocean, and central Asia in July, the NDW6-simulated SWCRF values are closer to the CERES results, whereas in Australia in January and in South Asia in July, the NSW6-simulated SWCRF values are closer to the CERES results. Conversely, in these areas, the magnitudes of the NDW6-
900 simulated SWCRF values are underestimated compared to the CERES results, which is caused by the underestimation of the NDW6-simulated clouds. Neither the NDW6- nor the NSW6-simulated SWCRF values are generally comparable to the CERES results in coastal central Africa in January, the outflow in northern Africa in January, the central Pacific Ocean in

January, and the Arctic in July. In zonal averages, these biases that are found in various areas may be effectively cancelled. The NDW6-simulated SWCRF values are closer to the CERES-retrieved results, especially for most of the Northern Hemisphere and at 60-90°S latitudes in January and at 30-90°N latitudes and most of the Southern Hemisphere in July. In contrast, the NSW6-simulated SWCRF values are closer to the CERES results, especially at 45°S-10°N latitudes in January and at 0-45°N latitudes in July.

Figure E2 shows the spatiotemporal distribution of the simulated OSR. As shown in Figure E1, the good performance of the NDW6-simulated clouds and SWCRF generally produces closer results to those of CERES in the Southern Ocean, Northern Pacific, and Atlantic Ocean in January. Especially over the ocean, the larger magnitude of the SWCRF yields a larger magnitude of the OSR. Therefore, the biases of the simulated SWCRF directly reflect the results of the simulated OSR. This is also indicated by the comparisons of the zonal distribution of both ~~the~~ SWCRF and OSR. Over land, however, due to limited clouds and large aerosols, radiative impacts due to aerosols can be found. In January, at 30-45°N latitudes, including industrial areas such as eastern China and dusty areas such as central Asia and western China, the NDW6-simulated SWCRF values are comparable to the CERES results, but the NDW6-simulated OSR values are larger than the CERES results. This suggests the overestimation of scattering aerosols, underestimation of light-absorbing aerosols, or overestimation of the surface albedo in ~~the~~ dusty areas. Figure 7 does not suggest overestimation of simulated aerosols compared to the satellite results. Figure C1 shows an underestimation tendency for absorption AOT among the AeroCom models. Therefore, overestimation of the simulated OSR may be caused by the underestimation of simulated light-absorbing aerosols. In July, at 60-90°N latitudes, even though the magnitudes of the NDW6-simulated SWCRF are lower than those of the CERES results, the NDW6-simulated OSR values are comparable to the CERES results. This may imply the underestimation of the simulated scattering aerosols, which is consistent with the results over the Arctic shown in Figure 12 of Goto et al. (2020), even though the seasonal variation in the simulated aerosols is comparable to the ground-based observations. Other possibilities include the overestimation of light-absorbing aerosols over the Arctic and/or this effect on the decrease in water vapor, but this possibility is inconsistent with the results of Figure C1. Globally, the NDW6-simulated OSR is more comparable to the CERES result than the NSW6 result in terms of annual, January, and July averages, as shown in Table ~~2~~1. The global and annual averages are calculated to be 98.6 Wm^{-2} (NDW6), 102.0 Wm^{-2} (NSW6), and 99.0 Wm^{-2} (CERES).

For longwave radiation, the impacts of ARI are relatively small. Because the NICAM does not explicitly address the interaction between aerosols and ice clouds, the impacts of the ACI on longwave radiation are also small. Here, the results of OLR and LWCRF are briefly discussed using the global averages shown in Table ~~2~~1. The global and annual averages of LWCRF are calculated to be 21.5 Wm^{-2} (NDW6), 26.8 Wm^{-2} (NSW6), and 27.9 Wm^{-2} (CERES). The NSW6-simulated LWCRF appears closer to the CERES results, especially at 30°S-30°N latitudes. When the horizontal distribution of the LWCRF is examined, compensation errors in terms of longitudes are found. In the western Pacific Ocean, the NSW6-simulated clouds at high levels are remarkably overestimated compared to the CERES results, but in other areas, both the NDW6- and NSW6-simulated LWCRF are underestimated compared to the CERES results. However, because the NDW6-simulated clouds at the high level are not as remarkably overestimated compared to the CERES results, the global average of the NDW6-simulated LWCRF is

lower than the CERES results. In the OLR shown in Table ~~2~~1, the global and annual averages are calculated to be 242.2 Wm^{-2} (NDW6), 236.8 Wm^{-2} (NSW6), and 240.2 Wm^{-2} (CERES). In January and July, the NDW6-simulated OLR appears close to the CERES results, whereas the NSW6-simulated OLR is lower than both the CERES and NDW6 results. As already

940   mentioned, compensation errors in the ~~horizontal~~ regional distribution arise, but such errors cannot be solved by improvements ~~of~~ to the aerosols.

Code and data availability

945   The source codes of NICAM.19 used in this study can be obtained at DOI:10.5281/zenodo.7731449 upon request under general terms and conditions (http://nicam.jp/hiki/?Research+Collaborations). The relevant model results in this study are archived at DOI:10.5281/zenodo.7731486.

Author contributions

DG designed and conducted the numerical experiments and analyses. TS and HY configured the model and prepared the
950   external conditions of the experiments. DG wrote the initial draft of the paper, and all the coauthors (TS, KS, HY, and TT) participated in the discussions of the results and commented on the original manuscript.

Competing interests

The authors declare that they have no conflicts of interest.

Acknowledgments

955   We acknowledge the developers and administrators of the NICAM (http://nicam.jp/; last access: ~~13~~30 ~~March~~ August 2023), MODIS (https://modis.gsfc.nasa.gov/; last access: 30 August~~13 March~~ 2023), MISR (https://misr.jpl.nasa.gov/; last access 30 August~~13 March~~ 2023), CALIOP (https://www-calipso.larc.nasa.gov/; last access: 30 August~~13 March~~ 2023), GPGP (https://www.ncei.noaa.gov/access/metadata/landing-page/bin/iso?id=gov.noaa.ncdc:C00933; last access 30 August ~~13 March~~ 2023), MACLWP (https://disc.gsfc.nasa.gov/datasets/MACLWP_diurnal_1/summary?keywords=measures; last access 30
960   August ~~13 March~~ 2023), ISCCP (https://isccp.giss.nasa.gov/; last access 30 August ~~13 March~~ 2023), 2C-RAIN-PROFILE (https://www.cloudsat.cira.colostate.edu/data-products/2c-rain-profile; last access ~~13 March~~30 August 2023), and the relevant PIs of the IMPROVE (http://vista.cira.colostate.edu/Improve/; last access: ~~13 March~~30 August 2023), EMEP (https://www.emep.int/; last access: 30 August~~13 March~~ 2023), EANET (https://www.eanet.asia/; last access: 30 August~~13 March~~ 2023), AERONET (https://aeronet.gsfc.nasa.gov/; last access: 30 August~~13 March~~ 2023), SKYNET
965   (https://www.skynet-isdc.org/; last access: 30 August~~13 March~~ 2023) and CARSNET sites. The CERES datasets were obtained from the NASA LaRC Atmospheric Science Data Center (https://asdc.larc.nasa.gov/; last access: 30 August ~~13 March~~2023).

Some of the authors were supported by the Environment Research and Technology Development Fund S-20 (S-20-1(1): JPMEERF21S12001, S-20-1(3): JPMEERF21S12003, and S-20-1(4): JPMEERF21S12004) of the Environmental Restoration and Conservation Agency that were provided by the Ministry of Environment (MOE) of Japan and by the Japan Society for the Promotion of Science (JSPS) KAKENHI grants (17H04711 and 19H05669) and the Ministry of Education, Culture, Sports, Science, and Technology (MEXT) (JPMXP1020200305) via the "Program for Promoting Research on the Supercomputer Fugaku" (Large Ensemble Atmospheric and Environmental Prediction for Disaster Prevention and Mitigation). Additionally, we were supported by the Advanced Studies of Climate Change Projection (SENTAN) of MEXT (JPMXD0722680395), MOE/GOSAT, Japan Science and Technology (JST), Japan Aerospace Exploration Agency (JAXA)/EarthCARE, JAXA/GCOM-C, and National Institute for Environmental Studies (NIES), Japan. The model simulations were performed using the following supercomputers: the RIKEN/Fugaku computer (hp210166, hp210253, hp220167, and hp220213), Flow at Information Technology Center, Nagoya University, and NEC SX-Aurora TSUBASA at NIES. Global maps in the figures are drawn using the Grid Analysis and Display System (GrADS) (http://cola.gmu.edu./grads/; last access: 20 30 December August 2022 2023). We acknowledge Takuro Michibata (Okayama University, Japan) for preparing the Cloudsat datasets in Figure 5 and discussing the cloud precipitation in NICAM, Eiji Oikawa (Meteorological Research Institute, Japan) for preparing the CALIPSO dataset used in Goto et al. (2020), Takashi M. Nagao (University of Tokyo, Japan) for preparing the MODIS cloud dataset used in Goto et al. (2020), and Haruka Hotta (University of Tokyo, Japan) for helping set up the NICAM to run with NDW6.

References

Abdul-Razzak, H., and Ghan, S. J.: A parameterization of aerosol activation: 2 Multiple aerosol types, J. Geophys. Res., 105, D5, 6837-6844, doi:10.1029/1999JD901161, 2000.

Adler, R. F., Huffman, G. J., Chang, A., Ferraro, R., Xie, P., Janowiak, J., Rudolf, B., Schneider, U., Curtis, S., Bolvin, D., Gruber, A., Susskind, J., and Arkin, P.: The version 2 Global Precipitation Climatology Project (GPCP) monthly precipitation analysis 1979-present, J. Hydrometeorol., 4, 1147-1167, doi:10.1175/1525-7541(2003)004<1147:TVGPCP>2.0.CO;2, 2003.

Albrecht, B. A.: Aerosols, cloud microphysics, and fractional cloudiness, Science, 245(4923), 1227-1230, http://doi.org/10.1126/science.245.4923.1227, 1989.

Alfaro-Contreras, R., Zhang, J., Reid, J. S., and Chistopher, S.: A study of 15-year aerosol optical thickness and direct shortwave aerosol radiative effect trends using MODIS, MISR, CALIOP and CERES. Atmos. Chem. Phys., 17, 13849-13868, https://doi.org/10.5194/acp-17-13849-2017, 2017.

Bates, T. S., Charlson, R. J., and Gammon, R. H.: Evidence for the climate role of marine biogenic sulphur, Nature, 329, 319–321, 1987.

Berry, E. X.: Cloud droplet growth by collection, J. Atmos. Sci., 24, 688-701, 1967.

1000 Carslaw, K. S., Lee, L. A., Reddington, C. L., Pringle, K. L., Rap, A., Forster, P. M., Mann, G. W., Spracklen, D. V., Woodhouse, M. T., Regayre, L. A., and Pierce, J. R.: Large contribution of natural aerosols to uncertainty in indirect forcing, Nature, 503, 67-71, doi:10.1038/nature12674, 2013.

Che, H., Zhang, X.-Y., Xia, X., Goloub, P., Holben, B., Zhao, H., Wang, Y., Zhang, X.-C., Wang, H., Blarel, L., Damiri, B., Zhang, R., Deng, X., Ma, Y., Wang, T., Geng, F., Qi, B., Zhu, J., Yu, J., Chen, Q., and Shi, G.: Ground-based aerosol

1005 climatology of China: aerosol optical depths from the China Aerosol Remote Sensing Network (CARSNET) 2002–2013, Atmos. Chem. Phys., 15, 7619–7652, doi:10.5194/acp-15-7619-2015, 2015.

Christensen, M. W., Stephens, G. L., and Lebsock, M. D.: Exposing biases in retrieved low cloud properties from CloudSat: A guide for evaluating observations and climate data, J. Geophys. Res. Atmos., 116, 12120-12131, doi:10.1002/2013JD020224, 2013.

1010 Chung, S. H., and Seinfeld, J. H.: Global distribution and climate forcing of carbonaceous aerosols, J. Geophys. Res., 107(D19), 4407, doi:10.1029/2001JD001397, 2002.

Coppola, E., Sobolowski, S., Pichelli, E., Raffaele, F., Ahrens, B., Ander, I., Ban, N., Bastin, S., Belda, M., Belusic, D., Caldas-Alvarez, A., Cardoso, R. M., Davolo, S., Dobler, A., Fernandez, J., Fita, L., Fumiere, Q., Giorgi, F., Goergen, K., Güttler I., Halenka, T., Heinzeller, D., Hodnebrog, Ø., Jacob, D., Kartsios, S., Katragkou, E., Kendon, E., Khodayar, S.,

1015 Kunstmann, H., Knist, S., Lavín-Gullón, A., Lind, P., Lorenz, T., Maraun, D., Marelle, L., van Meijgaard, E., Milovac, J., Myhre, G., Panitz, H.-J., Piazza, M., Raffa, M., Raub, T., Rockel, B., Schär, C., Sieck, K., Soares, P. M. M., Somot, S., Srnec, L., Stocchi, P., Tölle, M. H., Truhetz, H., Vautard, R., de Vries, H., and Warrach-Sagi, K.: A first-of-its-kind multi-model convection permitting ensemble for investigating convective phenomena over Europe and the Mediterranean, Clim. Dyn., 55, 3-34, https://doi.org/10.1007/s00382-018-4521-8, 2020.

1020 Dai, T., Goto, D., Schutgens, N. A. J., Dong, X., Shi, G., and Nakajima, T.: Simulated aerosol key optical properties over global scale using an aerosol transport model coupled with a new type of dynamic core. Atmos. Environ., 82, 71-82, https://doi.org/10.1016/j.atmosenv.2013.10.018, 2014.

Dai, T., Shi, G., and Nakajima, T.: Analysis and evaluation of the global aerosol optical properties simulated by an online aerosol-coupled non-hydrostatic icosahedral atmospheric model, Adv. Atmos. Sci., 32(6), 743–758, doi:

1025 10.1007/s00376-014-4098-z, 2015.

Diehl, T., Heil, A., Chin, M., Pan, X., Streets, D., Schulz, M., and Kinne, S.: Anthropogenic, biomass burning, and volcano emissions of black carbon, organic carbon, and SO_2 from 1980 to 2010 for hindcast model experiments, Atmos. Chem. Phys. Discuss., 12, 24895-24954, doi:10.5194/acpd-12-24895-2012, 2012.

Elsaesser, G. S., O'Dell, C. W., Lebsock, M. D., Bennartz, R., Greenwald, T. J., and Wentz, F. J.: The multisensor advanced

1030 climatology of liquid water path (MAC-LWP). J. Clim., 30(24), 10193–10210. https://doi.org/10.1175/JCLI-D-16-0902.1, 2017.

Forster, P., Storelvmo, T., Armour, K., Collins, W., Dufresne, J.-L., Frame, D., Lunt, D.J., Mauritsen, T., Palmer, M. D., Watanabe, M., Wild, M., and Zhang, H.: The Earth's Energy Budget, Climate Feedbacks, and Climate Sensitivity. In Climate Change 2021: The Physical Science Basis. Contribution of Working Group I to the Sixth Assessment Report of the Intergovernmental Panel on Climate Change [Masson-Delmotte, V., Zhai, P., Pirani, A., Connors, S.L., Péan, C., Berger, S., Caud, N., Chen, Y., Goldfarb, L., Gomis, M. I., Huang, M., Leitzell, K., Lonnoy, E., Matthews, J. B. R., Maycock, T. K., Waterfield, T., Yelekçi, O., Yu, R., and Zhou, B. (eds.)]. Cambridge University Press, Cambridge, United Kingdom and New York, NY, USA, pp. 923–1054, doi:10.1017/9781009157896.009, 2021.

Hoesly, R. M., Smith, S. J., Feng, L., Klimont, Z., Janssens-Maenhout, G., Pitkanen, T., Seibert, J. J., Vu, L., Andres, R. J., Bolt, R. M., Bond, T. C., Dawidowski, L., Kholod, N., Kurokawa, J., Li, M., Liu, L., Lu, Z., Moura, M. C. P., O'Rourke, P. R., and Zhang, Q.: Historical (1750-2014) anthropogenic emissions of reactive gases and aerosols from the Community Emissions Data System (CEDS), Geosci. Model Dev., 11, 369-408, doi:10.5194/gmd-11-369-2018, 2018.

Hsu, N. C., Jeong, M. J., Bettenhausen, C., Sayer, A. M., Hansell, R., Seftor, C. S., Huang, J., and Tsay, S. C.: Enhanced Deep Blue aerosol retrieval algorithm: the second generation. J. Geophys. Res.-Atmos. 118, 9296–9315, 2013.

Ghan, S. J.: Technical Note: Estimating aerosol effects on cloud radiative forcing, Atmos. Chem. Phys., 13, 9971-9974, doi:10.5194/acp-13-9971-2013, 2013.

Gliß J., Mortier, A., Schulz , M., Andrews, E., Balkanski, Y., Bauer, S. E., Benedictow, A. M. K., Bian, H., Checa-Garcia, R., Chin, M., Ginoux, P., Griesfeller, J. J., Heckel, A., Kipling, Z., Kirkevåg, A., Kokkola, H., Laj, P., Le Sager, P., Lund, M. T., Myhre, C. L., Matsui, H., Myhre, G., Neubauer, D., van Noije, T., North, P., Olivié, D. J. L., Rémy, S., Sogacheva, L., Takemura, T., Tsigaridis, K., and Tsyro, S. G.: AeroCom phase III multi-model evaluation of the aerosol life cycle and optical properties using ground- and space-based remote sensing as well as surface in situ observations. Atmos. Chem. Phys., 21, 87-128, https://doi.org/10.5194/acp-21-87-2021, 2021.

Goto, D.: Modeling of black carbon in Asia using a global-to-regional seamless aerosol-transport model, Environ. Pol., 195, 330-335, http://dx.doi.org/10.1016/j.envpol.2014.06.006, 2014.

Goto, D., Nakajima, T., Takemura, T., and Sudo, K.: A study of uncertainties in the sulfate distribution and its radiative forcing associated with sulfur chemistry in a global aerosol model, Atmos. Chem. Phys., 11, 10889-10910, doi:10.5194/acp-11-10889-2011, 2011.

Goto, D., Oshima, N., Nakajima, T., Takemura, T., and Ohara, T.: Impact of the aging process of black carbon aerosols on their spatial distribution, hygroscopicity, and radiative forcing in a global climate model, Atmos. Chem. Phys. Discuss., 12, 29801-29849, doi:10.5194/acpd-12-29801-2012, 2012.

Goto, D., Dai, T., Satoh, M., Tomita, H., Uchida, J., Misawa, S., Inoue, T., Tsuruta, H., Ueda, K., Ng, C.F.S., Takami, A., Sugimoto, N., Shimizu, A., Ohara, T., and Nakajima,T.: Application of a global nonhydrostatic model with a stretched-grid system to regional aerosol simulations around Japan, Geosci. Model Dev., 8, 235-259. Doi:10.5194/gmd-8-235-2015, 2015.

1065 Goto, D., Kikuchi, M., Suzuki, K., Hayasaki, M., Yoshida, M., Nagao, T. M., Choi, M., Kim, J., Sugimoto, N., Shimizu, A., Oikawa, E., and Nakajima, T.: Aerosol model evaluation using two geostationary satellites over East Asia in May 2016, Atmos. Res., 217, 93-113, doi:10.1016/j.atmosres.2018.10.016, 2019.

Goto, D., Sato, Y., Yashiro, H., Suzuki, K., Oikawa, E., Kudo, R., Nagao, T. M., and Nakajima, T.: Global aerosol simulations using NICAM.16 on a 14 km grid spacing for a climate study: improved and remaining issues relative to a lower-
1070 resolution model. Geosci. Model Dev., 13, 3731-3768, doi:10.5194/gmd-13-3731-2020, 2020.

Goto, D., and Uchida, J.: Uncertainty in Aerosol Rainout Processes Through the Case of the Radioactive Materials Emitted by the Fukushima Dai-ichi Nuclear Power Plant in March 2011. J. Meteorol. Soc. Japan., 100(1), 197-217, doi:10.2151/jmsj.2022-010, 2022.

Guenther, A., Hewitt, C. N., Erickson, D., Fall, R., Geron, C., Graedel, T., Harley, P., Klinger, L., Lerdau, M., McKay, W. A.,
1075 Pierce, T., Scholes, B., Steincrecher, R., Tallamraju, R., Taylor, J., and Zimmerman, P. A.: Global-Model of Natural Volatile Organic-Compound Emissions, J. Geophys. Res., 100, 8873–8892, 1995.

Henzing, J. S., Olivié, D. J. L., and van Velthoven, P. F. J.: A parameterization of size resolved below cloud scavenging of aerosols by rain, Atmos. Chem. Phys., 6, 3363-3375, https://doi.org/10.5194/acp-6-3363-2006, 2006.

Holben, B. N., Eck, T. F., Slutsker, I., Tanré, D., Buis, J. P., Setzer, A., Vermote, E., Reagan, J. A., Kaufman, Y., Nakajima,
1080 T., Lavenu, F., Jankowiak, I., and Smirnov, A.: AERONET – A federated instrument network and data archive for aerosol characterization, Rem. Sens. Environ., 66, 1-16, 1998.

Huang, Y., Siems, S. T., Manton, M. J., Hande, L. B., and Haynes, J. M.: The structure of low-altitude clouds over the Southern Ocean as seen by CloudSat, J. Clim., 25, 2535-2546, doi:10.1175/JCLI-D-11-00131.1, 2012.

Huneeus, N., Schulz, M., Balkanski, Y., Griesfeller, J., Prospero, J., Kinne, S., Bauer, S., Boucher, O., Chin, M., Dentener, F.,
1085 Diehl, T., Easter, R., Fillmore, D., Ghan, S., Ginoux, P., Grini, A., Horowitz, L., Koch, D., Krol, M. C., Landing, W., Liu, X., Mahowald, N., Miller, R., Morcrette, J.-J., Myhre, G., Penner, J., Perlwitz, J., Stier, P., Takemura, T., and Zender, C. S.: Global dust model intercomparison in AeroCom phase I, Atmos. Chem. Phys., 11, 7781-7816, doi:10.5194/acp-11/7781-2011, 2011.

Janssens-Maenhout, G., Crippa, M., Guizzardi, D., Dentener, F., Muntean, M., Pouliot, G., Keating, T., Zhang, Q., Kurokawa,
1090 J., Wankmüller, R., Denier van der Gon, H., Kuenen, J. J. P., Klimont, Z., Frost, G., Darras, S., Koffi, B., and Li, M.: HTAP_v2.2: a mosaic of regional and global emission grid maps for 2008 and 2010 to study hemispheric transport of air pollution, Atmos. Chem. Phys., 15, 11411–11432, 2015.

Kahn, R. A., Gaitley, B. J., Garay, M. J., Diner, D. J., Eck, T. F., Smirnov, A., and Holben, B. N.: Multiangle Imaging SpectroRatiometer global aerosol product assessment by comparison with the Aerosol Robotic Network, J. Geophys.
1095 Res., 115, D23209, doi:10.1029/2010JD014601, 2010.

Kalnay, E., Kanamitsu, M., Kistler, R., Collins, W., Deaven, D., Gandin, L., Iredell, M., Saha, S., White, G., Woollen, J., Zhu, Y., Chelliah, M., Ebisuzaki, W., Higgins, W., Janowiak, J., Mo, K. C., Ropelewski, C., Wang, J., Leetmaa, A., Reynolds, R., Jeene, R., and Joseph, D.: The NCEP/NCAR 40-year reanalysis project, B. Am. Meteorol. Soc., 77(3), 437-,471 1996.

1100 Khairoutdinov, M., and Kogan, Y.: A new cloud physics parameterization in a large-eddy simulation model of marine stratocumulus. Mon. Wea. Rev., 128, 229–243, 2000.

Kim, M. -H., Kin, S. -W., Yoon S. -C., and Omar, A. H.: Comparison of aerosol optical depth between CALIOP and MODIS-Aqua for CALIOP aerosol subtypes over the ocean, J. Geophys. Res. Atmos., 118, 13241-13252, doi:10.1002/2013JD019527, 2013.

1105 Kim, M. -H., Omar, A. H., Tackett, J. L., Vaughan, M. A., Winker, D. M., Trepte, C. R., Hu Y., Liu, Z., Poole, L. R., Pitts, M. C., Kar, J., and Magill, B. E.: The CALIPSO version 4 automated aerosol classification and lidar ratio selection algorithm, Atmos. Meas. Tech., 11, 6107-6135, https://doi..org/10.5194/amt-11-6107-2018, 2018.

Kinne, S.: Aerosol radiative effects with MACv2, Atmos. Chem. Phys., 19, 10919-10959, doi:10.5194/acp-19-10919-2019, 2019.

1110 Kodama C., Noda, A. T., and Satoh, M.: An Assessment of the cloud signals simulated by NICAM using ISCCP, CALIPSO, and CloudSat satellite simulators, J. Geophys. Res, doi:10.1029/2011JD017317, 2012.

Kodama, C., Yamada, Y., Noda, A. T., Kajikawa, Y., Nasuno, T., Yamaura, T., Takahashi, H. G., Hara, M., Kawatani, Y., Satoh, M., and Sugi, M.: A 20-year climatology of a NICAM AMIP-type simulation. J. Meteorol. Soc. Japan. Ser. II 93, 393-424, doi:10.2151/jmsj.2015-024, 2015.

1115 Kodama, C., Ohno, T., Seiki, T., Yashiro, H., Noda, A. T., Nakano, M., Yamada, Y., Roh, W., Satoh, M., Nitta, T., Goto, D., Miura, H., Nasuno, T., Miyakawa, T., Chen, Y.-W., and Sugi, M.: The non-hydrostatic global atmospheric model for CMIP6 HighResMIP simulations (NICAM16-S): Experimental design, model description, and sensitivity experiments. Geosci. Model Dev.,14, 795-820, doi:10.5194/gmd-14-795-2021, 2021.

Koffi, B., Schulz, M., Bréon, F. -M., Dentener, F., Steensen, B. M., Griesfeller, J., Winker, D., Balkanski, Y., Bauer, S. E.,
1120 Chin, M., Diehl, T., Easter, R., Ghan, S., Hauglustaine, D. A., Iversen T., Kirkevåg, A., Liu, X., Lohmann, U., Myhre, G., Rasch, P., Seland, Ø., Skeie, R. B., Steenrod, S. D., Stier, P., Tackett, J., Takemura, T., Tsigaridis, K., Vuolo, M. R., Yoon, J., and Zhang, K.: Evaluation of the aerosol vertical distribution in global aerosol models through comparison against CALIOP measurements: AeroCom phase II results, J. Geophys. Res. Atmos., 121, 7254-7283, doi:10.1002.2015JD024639, 2016.

1125 Lebsock M. D., and L'Ecuyer, T. S.: The retrieval of warm rain from CloudSat, J. Geophys. Res. Atmos., 116, D20, https://doi.org/10.1029/2011JD016076, 2011.

Levy, R. C., Mattoo, S., Munchak, L. A., Remer, L. A., Sayer, A. M., Patadia, F., and Hsu, N. C.: The Collection 6 MODIS aerosol products over land and ocean. Atmos. Meas. Tech. 6, 2989–3034, https://doi.org/10.5194/amt-6-2989-2013, 2013.

Liu, B., Ma Y., Gong, W., Zhang, M., Wang, W., and Shi, Y.: Comparison of AOD from CALIPSO, MODIS, and Sun
1130 Photometer under different conditions over Central China, Sci. Rep., 8:10066, doi:10.1038/s41598-018-28417-7, 2018.

Liu, Y.: Impacts of active satellite sensors' low-level cloud detection limitations on cloud radiative forcing in the Arctic, Atmos. Chem. Phys., 22, 8181-8173, https://doi/org/10.5194/acp-22-8151-2022, 2022.

Loeb, N. G., Wielicki, B. A., Doelling, D. R., Smith, D. R., Keyes, D. F., Kato, S., Manalo-Smith, N., and Wong, T.: Toward optimal closure of the Earth's top-of-atmosphere radiation budget. J. Clim., 22, 748-766, doi:10.1175/2008JCLI2637.1., 2009.

Lohmann, U., Feichter, J., Chuang, C. C., and Penner, J. E.: Prediction of the number of cloud droplets in the ECHAM GCM, J. Geophys. Res., 104 (D8), 9169-9198, 1999.

Ma, X., Bartlett, K., Harmon, K., and Yu, F.: Comparison of AOD between CALIPSO and MODIS: significant differences over major dust and biomass burning regions, Atmos. Meas. Tech., 6, 2391-2401, doi:10.5194/amt-6-2391-2013, 2013.

Ma, P.-L., Rasch, P. J., Fast, J. D., Easter, R. C., Gustafson Jr., W. I., Liu, X., Ghan S. J., and Singh, S.: Assessing the CAM5 physics suite in the WRF-Chem model: implementation, resolution sensitivity, and a first evaluation for regional case study, Geosci. Model Dev., 7, 755-778, doi:10.5194/gmd-7-755-2014, 2014.

Ma, P. -L., Rasch, P. J., Chepfer, H., Winker, D. M., and Ghan, S. J.: Observational constraint on cloud susceptibility weakened by aerosol retrieval limitations, Nat. Comm., 9, 2640, doi:10.1038/s41467-018-05028-4, 2018.

Malavelle, F., Haywood, J. M., Jones, A., Gettelman, A., Clarisse, L., Bauduin, S., Allan, R. P., Karset, I. H. H., Kristjánsson, J. E., Oreopoulos, L., Cho, N., Lee, D., Bellouin, N., Boucher, O., Grosvenor, D. P., Carslaw, K. S., Dhomse, S., Mann, G. W., Schmidt, A., Coe, H., Hartley, M. E., Dalvi, M., Hill, A. A., Johnson, B. T., Johnson, C. E., Knight, J. R., O'Connor, F. M., Partridge, D. G., Stier, P., Myhre, G., Platnick, S., Stephens, G. L., Takahashi, H., and Thordarson, T.: Strong constraints on aerosol-cloud interaction from volcanic eruptions, Nature, 546, 485-491, doi:10/1038/nature22974, 2017.

Malm, W. C., Sislerm J. F., Huffmann, D., Eldred, R. A., and Cahill, T. A.: Spatial and seasonal trends in particle concentration and optical extinction in the United States, J. Geophys. Res., 99, 1347-1370, https://doi.org/10.1029/93JD02916. 1994.

Mellor, G. L., and Yamada, T.: A hierarchy of turbulence closure models for planetary boundary layers, J. Atmos. Sci., 31, 1791–1806, doi: 10.1175/1520-0469(1974)031<1791:AHOTCM>2.0.CO;2, 1974.

Michibata, T., and Suzuki, K.: Reconciling compensating errors between precipitation constraints and the energy budget in a climate model, Geophys Res. Lett., 47, e2020GL088340, doi:10.1029/2020GL088340, 2020.

Miura, H.: An upwind-biases conservative advection scheme for spherical hexagonal-pentagonal grids, Mon. Wea. Rev., 135, 4038-4044, 2007.

Morrison, H., Thompson, G., and Tatarskii, V.: Impact of cloud microphysics on the development of trailing stratiform precipitation in a simulated squall line: comparison of one- and two-moment schemes, Mon. Wea. Rev., 137, 991-1007, doi:10.1175/2008MWR2556.1, 2008.

Myhre G., Samset, B. H., Schulz, M., Balkanski, Y., Bauer, S., Berntsen, T. K., Bian, H., Bellouin, N., Chin, M., Diehl, T., Easter, R. C., Feichter, J., Ghan, S. J., Hauglustaine, D., Iversen, T., Kinne, S., Kirkevåg, A., Lamarque, J. -F., Lin, G., Liu, X., Lund, M.T., Luo, G., Ma, X., van Noije, T., Penner, J.E., Rasch, P. J., Ruiz, A., Seland, Ø., Skeie, R. B., Stier, P., Takemura, T., Tsigaridis, K., Wang, P., Wang, Z., Xu, L., Yu, H., Yu, F., Yoon, J.-H., Zhang, K., Zhang, H., and Zhou, C.: Radiative forcing of the direct aerosol effect from AeroCom Phase II simulations, Atmos. Chem. Phys. 13, 1853-1877, doi:10.5184/acp-13-1853-2013, 2013.

Monahan, E. C., Spiel, D. E., and Davidson, K. L.: A model of marine aerosol generation via whitecaps and wave disruption, in Oceanic Whitecaps and Their Role in Air-Sea Exchange Processes, edited by E. C. Monahan and G. M. Niocaill, pp. 167-174, Springer, New York, 1986.

1170 Nakajima, T., Campanelli, M., Che, H., Estellés, V., Irie, H., Kim, S.-W., Kim, J., Liu, D., Nishizawa, T., Pandithurai, G., Vijay Kumar Soni, V. K., Thana, B., Tugjsurn, N. -T., Aoki, K., Sujung Go, S., Hashimoto, M., Higurashi, A., Kazadzis, S., Khatri P., Kouremeti, N., Kudo, R., Marenco, F., Momoi, M., Ningombam, S. S., Ryder, C. L., Uchiyama, A., and Yamazaki, A.: An overview of and issues with sky radiometer technology and SKYNET, Atmos. Meas. Tech., 13, 4195-4218, doi:10.5194/amt-13-4195-2020, 2020

1175 Nakanishi, M., and Niino, H.: An improved Mellor–Yamada level 3 model with condensation physics: its design and verification, Bound. Layer Meteor., 112, 1–31, doi:10.1023/B:BOUN.0000020164.04146.98, 2004.

Niwa, Y., Tomita, H., Satoh, M., and Imasu, R.: A three-dimensional icosahedral grid advection scheme preserving monotonicity and consistency with continuity for atmospheric tracer transport, J. Meteor. Soc. Jpn., 89, 255–268, doi: 10.2151/jmsj.2011-306, 2011.

1180 Noda, A. T., Oouchi, K., Satoh, M., Tomita, H., Iga, S., and Tsushima, Y.: Importance of the subgrid-scale turbulent moist process: Cloud distribution in global cloud-resolving simulations, Atmos. Res., 96, 208–217, doi:10.1016/j.atmosres.2009.05.007, 2010.

Noda, A., Seiki, T., Roh, W., Satoh, T., and Ohno, T.: Improved representation of low-level mixed-phase clouds in a global cloud-system-resolving simulation, J. Geophys. Res. Atmos, 126, e2021JD035223, 1185 https://doi.org/10.1029/2021JD035223, 2021.

Petrenko, M., and Ichoku, C.: Coherent uncertainty analysis of aerosol measurements from multiple satellite sensors, Atmos. Chem. Phys., 13, 6777-6805, doi:10.5194/acp-13-6777-2013, 2013.

Platnick, S., and Twomey, S.: Determining the susceptibility of cloud albedo to changes in droplet concentration with the advanced very high resolution radiometer, J. Appl. Meteorol., 33(3), 334-347, 1994.

1190 Platnick, S., Hubanks, P., Meyer, K., and King, M. D.: MODIS Atmosphere L3 Monthly Product. NASA MODIS Adaptive Processing System, Goddard Space Flight Center, USA: http://dx.doi.org/10.5067/MODIS/MOD08_M3.006, 2015.

Roh, W., and Satoh, M.: Evaluation of precipitating hydrometeor parameterizations in a single-moment bulk microphysics scheme for deep convective systems over the Tropical Central Pacific, J. Atmos. Sci., 77, 3781-3801, https://doi.org/10.1175/JAS-D-13-0252.1, 2014.

1195 Roh, W., Satoh, M., Hashino, T., Okamoto, H., and Seiki, T.: Evaluations of the thermodynamic phases of clouds in a cloud-system-resolving model using CALIPSO and a satellite simulator over the Southern Ocean, J. Atmos. Sci., 77, 3781-3801, https://doi.org/10.1175/JAS-D-19-0273.1, 2020.

Rossow, W. B., and Schiffer, R. A.: Advances in understanding clouds from ISCCP. Bulletin of the American Meteorological Society, 80, 2261–2287. https://doi.org/10.1175/1520-0477(1999)080<2261:AIUCFI>2.0.CO;2, 1999.

1200   Proestakis, E., Amiridis, V., Marinou, E., Georgoulias, A. K., Solomos, S., Kazadzis, S., Chimot, J., Che, H., Alexandri, G., Binietoglou,I., Daskalopoulou, V., Kourtidis, K. A., de Leeuw, G., and van der A, R. J.: Nine-year spatial and temporal evolution of desert dust aerosols over South and East Asia as retrieved by CALIOP, Atmos. Chem. Phys., 18, 1337-1362, https://doi.org//10.5194/acp-18-1337-2018, 2018.

Sand, M., Samset, B. H., Myhre, G., Gliß, J., Bauer, S. E., Bian, H., Chin, M., Checa-Garcia, R., Ginoux, P., Kipling, Z.,
1205   Kirkevåg, A., Kokkola, H., Sager, P. L., Lund, M. T., Matsui, H., van Noije, T., Olivié, D. J. L., Remy, S., Schulz, M., Stier, P., Stjern, C. W., Takemura, T., Tsigaridis, K., Tsyro, S. G., and Watson-Parris, D.: Aerosol absorption in global models from AeroCom Phase III. Atmos. Chem. Phys., 21, 15929–15947, doi:10.5194/acp-21-15929-2021, 2021.

Sato, Y., Goto, D., Michibata, T., Suzuki, K., Takemura, T., Tomita, H., and Nakajima, T.: Aerosol effects on cloud water amounts were successfully simulated by a global cloud-system resolving model, Nature Com., 9: 985,
1210   doi:10.1038/s41467-018-03379-6, 2018.

Satoh, M., Matsuno, T., Tomita, H., Miura, H., Nasuno, T., and Iga, S.: Nonhydrostatic icosahedral atmospheric model (NICAM) for global cloud resolving simulations. J. Comput. Phys., 227, 3486-3514. Doi:10.1016/j.jcp.2007.02.006, 2008.

Satoh, M., Inoue, T., and Miura, H.: Evaluations of cloud properties of global and local cloud system resolving models using
1215   CALIPSO and CloudSat simulators, J. Geophys. Res., 115, D00H14, https://doi.org/10.1029/2009JD012247, 2010.

Satoh, M., Tomita, H., Yashiro, H., Miura, H., Kodama, C., Seiki, T., Noda, A.T., Yamada, Y., Goto, D., Sawada, M., Miyoshi, T., Niwa, Y., Hara, M., Ohno, T., Iga, S., Arakawa, T., Inoue, T., and Kubokawa, H.: The non-hydrostatic icosahedral atmospheric model: description and development. Prog. Earth. Plan. Sci., 1, 18-49. Doi:10.1186/s40645-014-0018-1, 2014.

1220   Satoh, M., Stevens, B., Judt, F., and Khairoutdinov, M., Lin, S. -J., Putman, W. M., and Düben, P.: Global Cloud-Resolving Models, Curr. Clim. Change Rep., 5, 172-184, doi:10.1007/s40461-019-00131-0, 2019.

Sayer, A. M., Munchak, L. A., Hsu, N. C., Levy, R. C., Bettenhausen, C., and Jeong, M.-J.: MODIS collection 6 aerosol products: comparison between aqua's e-deep blue, dark target, and "merged" data sets, and usage recommendations. J. Geophys. Res.-Atmos. 119, 13965–13989, 2014.

1225   Schuster, G. L., Vaughan, M., MacDonnell, D., Su, W., Winker, D., Dubovik, O., Lapyonok, T., and Trepte, C.: Comparison of CALIPSO aerosol optical depth retrievals to AERONET measurements, and a climatology for the lidar ratio of dust, Atmos. Chem. Phys., 12, 7431-7452, doi:10.5194/acp-12-7431-2012, 2012.

Seifert, A., and Beheng, K. D.: A two-moment cloud microphysics parameterization for mixed-phase clouds. Part 1: Model description. Meteorol. Atmos. Phys., 92(1), 45–66. https://doi.org/10.1007/s00703-005-0112-4, 2006.

1230   Seiki, T., and Nakajima, T.: Aerosol effects of the condensation process on a convective cloud simulation. Journal of the Atmospheric Sciences, 71 (2), 833–853. https://doi.org/10.1175/JAS-D-12-0195.1, 2014.

Seiki, T., Kodama, C., and Noda, A. T.: Improvement in global cloud-system-resolving simulations by using a double-moment bulk cloud microphysics scheme, J. Clim., 28, 2405-2419, doi:10.1175/JCLI-D-14-00241.1, 2015.

Seiki, T., and Roh, W.: Improvements in supercooled liquid water simulations of low-level mixed-phase clouds over the Southern Ocean using a single-column model, J. Atmos. Sci., 77, 3803-3819, doi:10.1175/JAS-D-19-0266.1, 2020.

Seiki, T., Roh, W., and Satoh, M.: Cloud microphysics in global cloud resolving models, Atmosphere-Ocean, doi:10.1080/07055900.2022.2075310, 2022.

Sekiguchi, M., and Nakaima, T.: A k-distribution-based radiation code and its computational optimization for an atmospheric general circulation model, J. Quant. Spectrosc. Radiat. Transf., 109, 2779-2793, doi: 10.1016/j.jqsrt.2008.07.013, 2008.

Shi, Y., Zhang, J., Reid, J. S., Hyer, E. J., Eck, T. F., Holben, B. N., and Kahn, R. A.: A critical examination of spatial biases between MODIS and MISR aerosol products – application for potential AERONET deployment, Atmos. Meas. Tech., 4, 2823-2836, doi:10.5194/amt-4-2823-2011, 2011.

Shindell, D. T., Lamarque, J. F., Schulz, M., Flanner, M., Jiao, C., Chin, M., Young, P.J., Lee, Y.H., Rotstayn, L., Mahowald, N., Milly, G., Faluvegi, G., Balkanski, Y., Collins, W.J., Conley, A.J., Dalsoren, S., Easter, R., Ghan, S., Horowitz, L., Liu, X., Myhre, G., Nagashima, T., Naik, V., Rumbold, S.T., Skeie, R., Sudo, K., Szopa, S., Takemura, T., Voulgarakis, A., Yoon, J.H., and Lo, F.: Radiative forcing in the ACCMIP historical and future climate simulations. Atmos. Chem. Phys., 13:2939–2974, 2013.

Sogacheva, L., Popp, T., Sayer, A. M., Dubovik, O., Garay, M. J., Heckel, A., Hsu, N. C., Jethva H., Kahn, R. A., Kolmonen, P., Kosmale, M., de Leeuw, G., Levy, R. C., Litvinov, P., Lyapustin, A., North, P., Torres, O., and Arola, A.: Merging regional and global aerosol optical depth records from major available satellite products, Atmos. Chem. Phys., 20, 2031-2056, https://doi/org/105194/acp-20-2031-2020. 2020.

Sreekanth, V., and Kulkarni, P.: Comparison of V4 and V3 CALIOP (L3) aerosol products: A global perspective, Remote Sensing Applications: Society and Environment 20, 100412, https://doi.org/10.1016/j.rsase.2020.100412, 2020.

Stevens, B., Satoh, M., Auger, L., Biercamp, J., Bretherton, C. S., Chen, X., Düben, P., Judt, F., Khairoutdinov, M., Klocke, D., Kodama, C., Kornblueh L., Lin, S. -J., Neumann, P., Putman, W. M., Röber, N., Shibuya, R., Vanniere, B., Vidale, P. L., Wedi, N., and Zhou, L.: DYAMOND: the Dynamics of the Atmospheric general circulation Modeled On Non-hydrostatic Domains, Prog. Earth. Plan. Sci., 6:61, doi:10.1186/s40645-019-0304-z, 2019.

Stevens, B., Acquistapace, C., Hansen, A., Heinze, R., Klinger, C., Klocke, D., Rybka, H., Schubotz, W., Windmiller, J., Adamidis, P., and Arka, I.: The added value of large-eddy and storm-resolving models for simulating clouds and precipitation, J. Meteorol. Soc. Japan., 98(2), 395-435, doi:10.2151/jmsj.2020-021, 2020.

Sudo, K., Takahashi, M., Kurokawa, J., and Akimoto, H.: CHASER: A global chemical model of the troposphere: 1. Model description, J. Geophys. Res., 107 (D17), 4339, doi:10.1029/2001JD001113, 2002.

Suzuki, K., Nakajima, T., Satoh, M., Tomita, H., Takemura, T., Nakajima, T. Y., and Stephens, G. L.: Global cloud-system-resolving simulation of aerosol effect on warm clouds. Geophys. Res. Lett., 35, L19817. Doi:10.1029/2008GL035449, 2008.

Szopa, S., Naik, V., Adhikary, B., Artaxo, P., Berntsen, T., Collins, W.D., Fuzzi, S., Gallardo, L., Kiendler-Scharr, A., Klimont, Z., Liao, H., Unger, N., and Zanis, P.: Short-Lived Climate Forcers. In Climate Change 2021: The Physical Science Basis.

Contribution of Working Group I to the Sixth Assessment Report of the Intergovernmental Panel on Climate Change [Masson-Delmotte, V., Zhai, P., Pirani, A., Connors, S.L., Péan, C., Berger, S., Caud, N., Chen, Y., Goldfarb, L., Gomis, M.I., Huang, M., Leitzell, K., Lonnoy, E., Matthews, J.B.R., Maycock, T.K., Waterfield, T., YelekçI, O., Yu, R., and Zhou, B. (eds.)]. Cambridge University Press, Cambridge, United Kingdom and New York, NY, USA, pp. 817–922, doi:10.1017/9781009157896.008, 2021.

Takata, K., Emori, S., and Watanabe, T.: Development of the minimal advanced treatments of surface interaction and runoff, Global. Planet. Change, 38, 209-222, doi: 10.1016/S0921-8181(03)00030-4, 2003.

Takemura, T., Okamoto, H., Maruyama, Y., Numaguti, A., Higurashi, A., and Nakajima, T.: Global three-dimensional simulation of aerosol optical thickness distribution of various origins, J. Geophys. Res., 105, 17853–17873, doi: 10.1029/2000JD900265, 2000.

Takemura, T., Nozawa, T., Emori, S., Nakajima, T. Y., and Nakajima, T.: Simulation of climate response to aerosol direct and indirect effects with aerosol transport-radiation model. J. Geophys. Res., 110, D02202. https://doi.org/10.1029/2004JD005029, 2005.

Takemura, T., Egashira, M., Matsuzawa, K., Ichijo, H., O'ishi, R., and Abe-Ouchi, A.: A simulation of the global distribution and radiative forcing of soil dust aerosols at the Last Glacial Maximum, Atmos. Chem. Phys., 9, 3061-3073, 2009.

Takemura, T.: Return to different climate states by reducing sulphate aerosols under future CO_2 concentrations, Sci. Rep., 10, 21748, doi: 10.1038/s41598-020-78805-1, 2020.

Tatebe, H., Ogura, T., Nitta, T., Komuro, Y., Ogochi, K., Takemura, T., Sudo, K., Sekiguchi, M., Abe, M., Saito, F., Chikira, M., Watanabe, S., Mori, M., Hirota, N., Kawatani, Y., Mochizuki, T., Yoshimura, K., Takata, K., O'ishi, R., Yamazaki, D., Suzuki, T., Kurogi, M., Kataoka, T., Watanabe, M., and Kimoto, M.: Description and basic evaluation of simulated mean state, internal variability, and climate sensitivity in MIROC6. Geosci. Model. Dev. 12:2727–2765. https://doi.org/10.5194/gmd-12-2727-2019, 2019.

Textor, C., Schulz, M., Guibert, S., Kinne, S., Balkanski, Y., Bauer, S., Berntsen, T., Berglen, T., Boucher, O., Chin, M., Dentener, F., Diehl, T., Easter, R., Feichter, J., Fillmore, D., Ghan, S., Ginoux, P., Gong, S., Grini, A., Hendricks, J., Horowitz, L., Huang, P., Isaksen, I., Iversen, T., Kloster, S., Koch, D., Kirkevåg, A., Kristjansson, J. E., Krol, M., Lauer, A., Lamarque, J. F., Liu, X., Montanaro, V., Myhre, G., Penner, J. E., Pitari, G., Reddy, S., Seland, Ø., Stier, P., Takemura, T., and Tie, X.: Analysis and quantification of the diversities of aerosol life cycles within AeroCom, Atmos. Chem. Phys., 6, 1777–1813, doi: 10.5194/acp-6-1777-2006, 2006.

Thorsen, T. J., Winker, D. M., and Ferrare, R. A.: Uncertainty in observational estimates of the aerosol direct radiative effect and forcing, J. Clim., doi:10.1175/JCLI-D-19-1009.1, 2021.

Tomita, H.: New microphysics with five and six categories with diagnostic generation of cloud ice, J. Meteorol. Soc. Jpn., 86A, 121-142, 2008.

Toth, T. D., Zhang, J., Campbell, J. R., Reid, J. S., Shim Y., Johnson, R. S., Smirnov, A., Vaughan, M. A., and Winker, D. M.: Investigating enhanced Aqua MODIS aerosol optical depth retrievals over the mid-to-high latitude Southern Oceans

through intercomparison with co-located CALIOP, MAN, and AERONET data sets, J. Geophys. Res. Atmos., 118, 4700-4714, doi:10.1002/jgrd.50311, 2013.

Tsigaridis, K., Daskalakis, N., Kanakidou, M., Adams, P. J., Artaxo, P., Bahadur, R., Balkanski, Y., Bauer, S. E., Bellouin, N., Benedetti, A., Bergman, T., Berntsen, T. K., Beukes, J. P., Bian, H., Carslaw, K. S., Chin, M., Curci, G., Diehl, T., Easter, R. C., Ghan, S. J., Gong, S. L., Hodzic, A., Hoyle, C. R., Iversen, T., Jathar, S., Jimenez, J. L., Kaiser, J. W., Kirkevåg, A., Koch, D., Kokkola, H., Lee, Y. H., Lin, G., Liu, X., Luo, G., Ma, X., Mann, G. W., Mihalopoulos, N., Morcrette, J.-J., Müller, J.-F., Myhre, G., Myriokefalitakis, S., Ng, N. L., O'Donnell, D., Penner, J. E., Pozzoli, L., Pringle, K. J., Russell, L. M., Schulz, M., Sciare, J., Seland, Ø., Shindell, D. T., Sillman, S., Skeie, R. B., Spracklen, D., Stavrakou, T., Steenrod, S. D., Takemura, T., Tiitta, P., Tilmes, S., Tost, H., van Noije, T., van Zyl, P. G., von Salzen, K., Yu, F., Wang, Z., Wang, Z., Zaveri, R. A., Zhang, H., Zhang, K., Zhang, Q., and Zhang, X.: The AeroCom evaluation and intercomparison of organic aerosol in global models, Atmos. Chem. Phys., 14, 10845-10895, doi:10.5194/acp-14-10845-2014, 2014.

Twomey, S.: Pollution and the planetary albedo, Atmos. Environ., 8(12), 1251-1256, https://doi.org/10.1016/0004-6981(74)90004-3, 1974.

van der Werf, Randerson, J. T., Giglio, L., van Leeuwen, T. T., Chen, Y., Rogers, B. M., Mu, M., van Marle, M. J. E., Morton, D. C., Collatz, G. J., Yokelson, R. J., and Kasibhatla, P. S.: Global fire emissions estimates during 1997-2016, Earth Syst. Sci. Data, 9, 697-720, doi:10.5194/essd-9-697-2017, 2017.

Vergara-Temprado, J., Ban, N., Panosetti, D., Schulemmer, L., Schär, C.: Climate models permit convection at much coarser resolutions than previously considered, J. Clim., 33, 1915-1933, doi:10.1175/JCLI-D-19-0286.1, 2020.

Watson-Parris, D., Schutgems, N. Winker, D., Burton, S. P., Ferrare, R. A., and Stier, P.: On the limits of CALIOP for constraining modeled free tropospheric aerosol. Geophys. Res. Lett., 45, 9260-9266, doi:10.1029/2018GL078195, 2018.

Wedi, N. P., Polichtchouk, I., Dueben, P., Anantharaj, V. G., Bauer, P., Boussetta, S., Browne, P., Deconinck, W., Gaudin, W., Hadade, I., Hatfield, S., Iffrig, O., Lopez, P., Maciel, P., Mueller, A., Saarinen, S., Sandu, I., Quintino,T., and Vitart, F.: A baseline for global weather and climate simulations at 1 km resolution, J. Adv. Model. Earth Syst., 12, e2020MS002192. https://doi.org/10.1029/2020MS002192, 2020.

Wei, J., Peng, Y., Mahmood, R., Sun, L., and Guo, J.: Intercomparison in spatial distributions and temporal trends derived from multi-source satellite aerosol products, Atmos. Chem. Phys., 19, 7183-7207, https://doi.org/10.5194/acp-19-7183-2019, 2019.

Wilcox, L. J., Highwood, E. J., Booth, B. B. B., and Carslaw, K. S.: Quantifying sources of inter-model diversity in the cloud albedo effect, Geophys. Res. Lett., 42, doi:10.1002/2015GL063301, 2015.

Winker, D. M., Tackett, J. L., Getzewich, B. J., Liu, Z., Vaughan, M. A., and Rogers, R. R.: The global 3-D distribution of tropospheric aerosols as characterized by CALIOP, Atmos. Chem. Phys., 13, 3345–3361, https://doi.org/10.5194/acp-13- 3345-2013, 2013.

1335   Zhang, X. Y., Wang, Y. Q., Niu, T., Zhang, X. C., Gong, S. L., Zhang, Y. M., and Sun, J. Y.: Atmospheric aerosol compositions in China: spatial/temporal variability, chemical signature, regional haze distribution and comparisons with global aerosols, Atmos. Chem. Phys., 12, 779-799, doi:10.5194/acp-12-779-2012, 2012.

Table 1: Experimental design in this study and Goto et al. (2020) as a reference

Name	Version	Resolution [km]	Lev.	Cloud microphysics module	Autoconversion	Reference
NDW6	19	14	78	NDW6	Seifert and Beheng (2006)	This study
NSW6	19	14	78	NSW6	Khairoutdinov and Kogan (2000)	This study
HRM	16	14	38	NSW6	Berry (1967)	Goto et al. (2020)
LRM	16	56	38	NSW6	Berry (1967)	Goto et al. (2020)

340

Table 12: Annual, January and July mean values of clouds, precipitation, and radiation

	Precipitation [mm day^{-1}]	LWP[*1] [g m^{-2}]	COT[*2]	Low-level CF	OSR [W m^{-2}]	SWCRF [W m^{-2}]	OLR [W m^{-2}]	LWCRF [W m^{-2}]
Annual mean								
NDW6	3.01	95.8	7.1	0.19	98.6	-42.5	242.2	21.5
NSW6	2.78	104.4	8.3	0.19	102.0	-45.9	236.8	26.8
Observation[*3]	2.68	119.6	12.9	0.26	99.0	-45.7	240.2	27.9
January								
NDW6	2.99	98.0	7.2	0.18	105.9	-48.4	238.5	22.0
NSW6	2.79	99.1	8.1	0.18	106.7	-49.3	233.4	26.7
Observation[*3]	2.73	120.2	14.5	0.25	105.9	-50.4	237.6	27.6
July								
NDW6	3.09	100.7	7.3	0.21	94.4	-41.8	245.5	21.7
NSW6	2.85	119.0	9.3	0.21	101.6	-48.7	240.4	26.8
Observation[*3]	2.71	121.8	13.2	0.27	94.1	-44.5	244.0	27.7

[*1] LWP over oceans (60°S-60°N); [*2] COT (60°S-60°N); [*3] GPCP (precipitation), MAC (LWP), MODIS (COT), ISCCP (low-level CF), and CERES (OSR, SWCRF, OLR, and LWCRF)

345

Table 2: Global and annual mean values of ERFari for anthropogenic aerosol, ERFaci for anthropogenic aerosol-, and the net ERF (sum of ERFari and ERFaci) for shortwave, longwave, and net (sum of shortwave and longwave) radiation under the all-sky abnd clear-sky conditions. All units are in W m^{-2}.

	ERFari under the all-sky conditions			
	NDW6	NSW6	HRM	LRM
Shortwave	-0.22	-0.26	-0.33	-0.26
Longwave	0.03	0.03	0.04	0.02
Net	-0.19	-0.23	-0.29	-0.24
	ERFari under the clear-sky conditions			
Shortwave	-0.52	-0.60	-0.63	-0.51
Longwave	0.05	0.05	0.05	0.03
Net	-0.47	-0.55	-0.57	-0.48
	ERFaci			
Shortwave	-1.34	-0.63	-0.81	-1.17
Longwave	0.06	-0.10	-0.12	0.07
Net	-1.28	-0.73	-0.93	-1.10
	ERFari+ERFaci			
Shortwave	-1.56	-0.89	-1.15	-1.43
Longwave	0.09	-0.07	-0.08	0.09
Net	-1.47	-0.96	-1.23	-1.34

Table 3: Global and regional averages of the differences in AOT, LWP and shortwave ERFaci between the preindustrial and the present day	AOT		LWP		ERFaci	
	NDW6	NSW6	NDW6	NSW6	NDW6	NSW6
Global	0.023	0.031	2.12	0.65	-1.34	-0.63
US[*1]	0.071	0.076	7.52	4.96	-4.30	-3.07
Europe[*2]	0.062	0.070	15.45	2.52	-7.29	-3.05
East Asia[*3]	0.201	0.203	8.77	0.00	-4.92	-3.35
India[*4]	0.129	0.176	3.36	-0.44	-2.25	-1.38

1350 [*1] US (90°W-60°W, 30°N-50°N); [*2] Europe (0°E-30°E, 40°N-60°N) ; [*3] East Asia (110°E-140°E, 20°N-50°N) ; [*4] India (70°E-90°E, 10°N-35°N)

1355
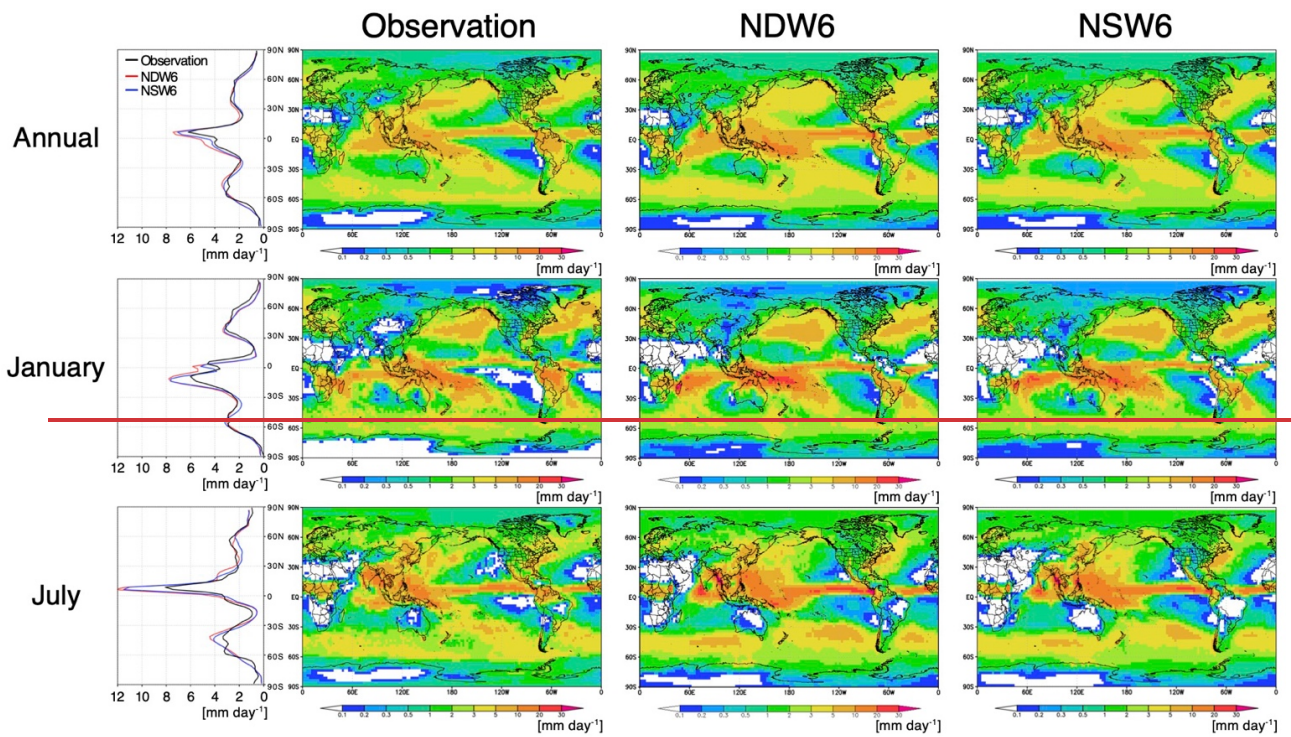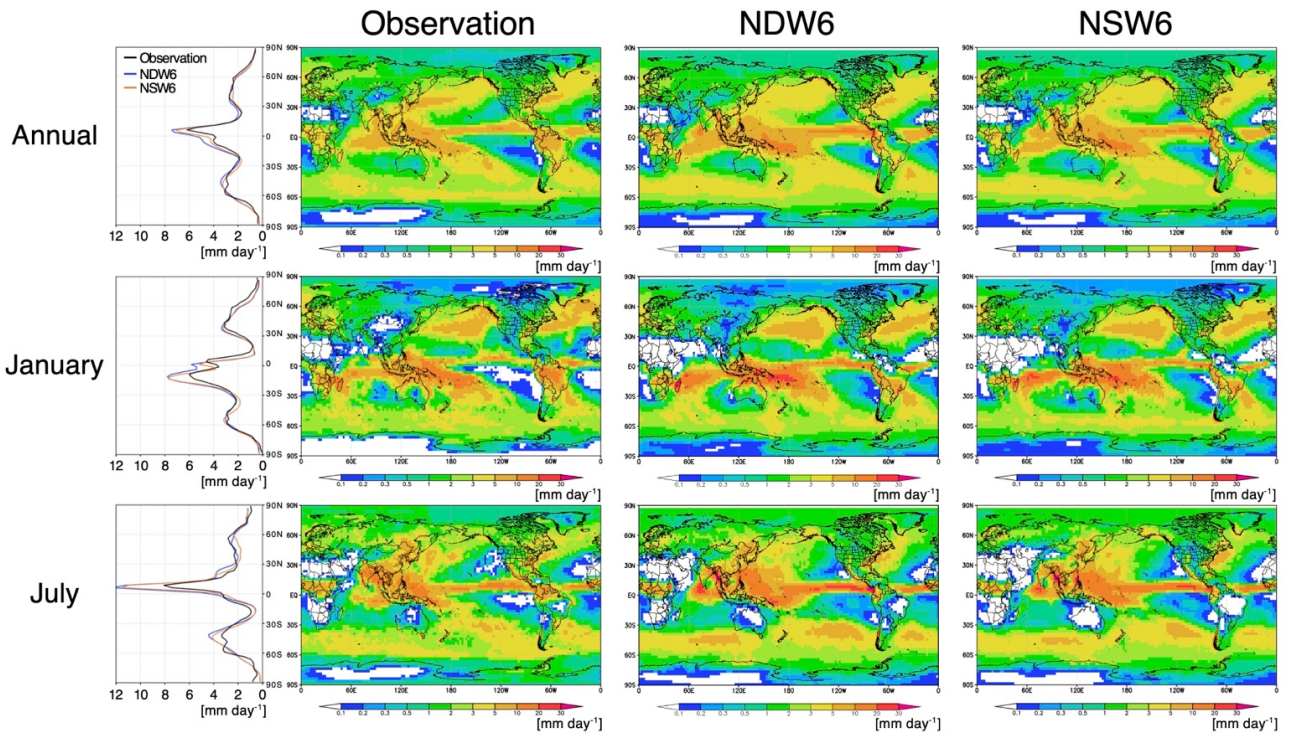
Figure 1: Zonal and horizontal distribution of precipitation (NDW6 and NSW6 ~~defined in Table 1~~simulations and GPCP~~)~~ as observations) as annual, January, and July averages. All units are in mm day⁻¹.

360
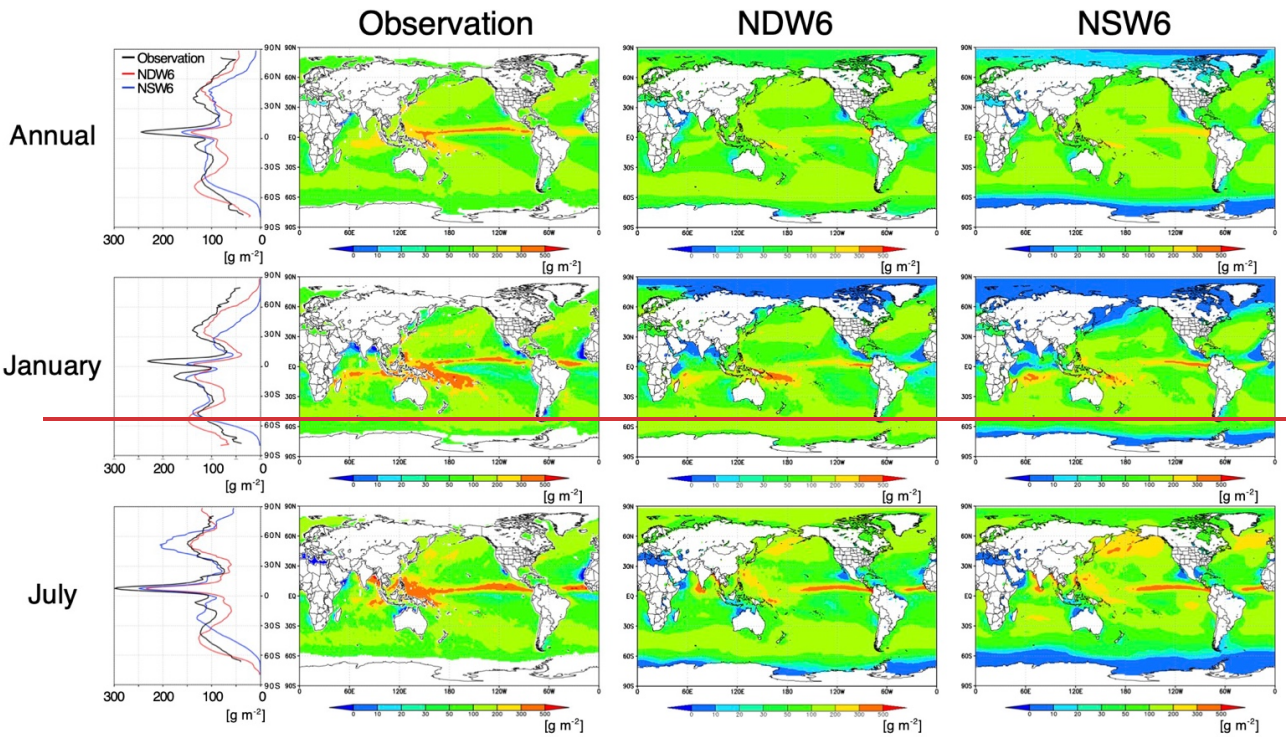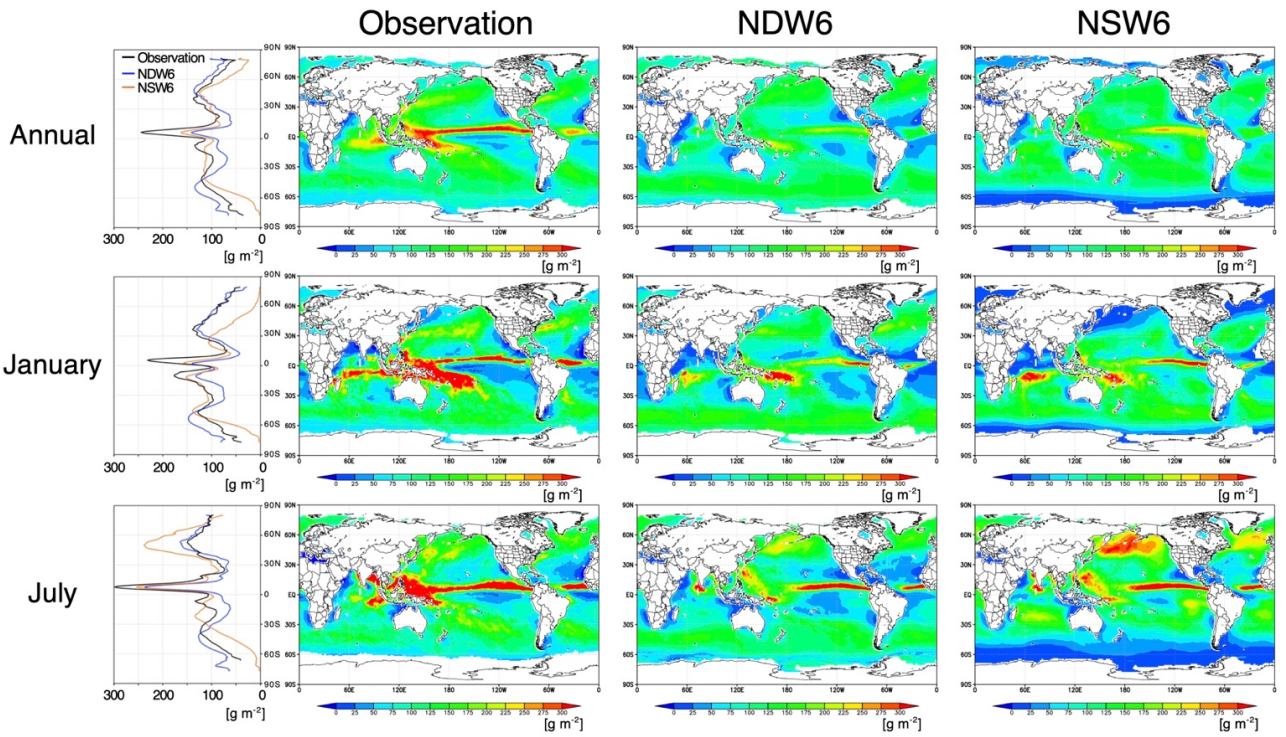
365   **Figure 2: Zonal and horizontal distributions of LWP (NDW6 and NSW6 ~~defined in Table 1~~simulations and MAC as observations)**

over only the ocean as annual, January, and July averages. All units are in g m^{-2}.
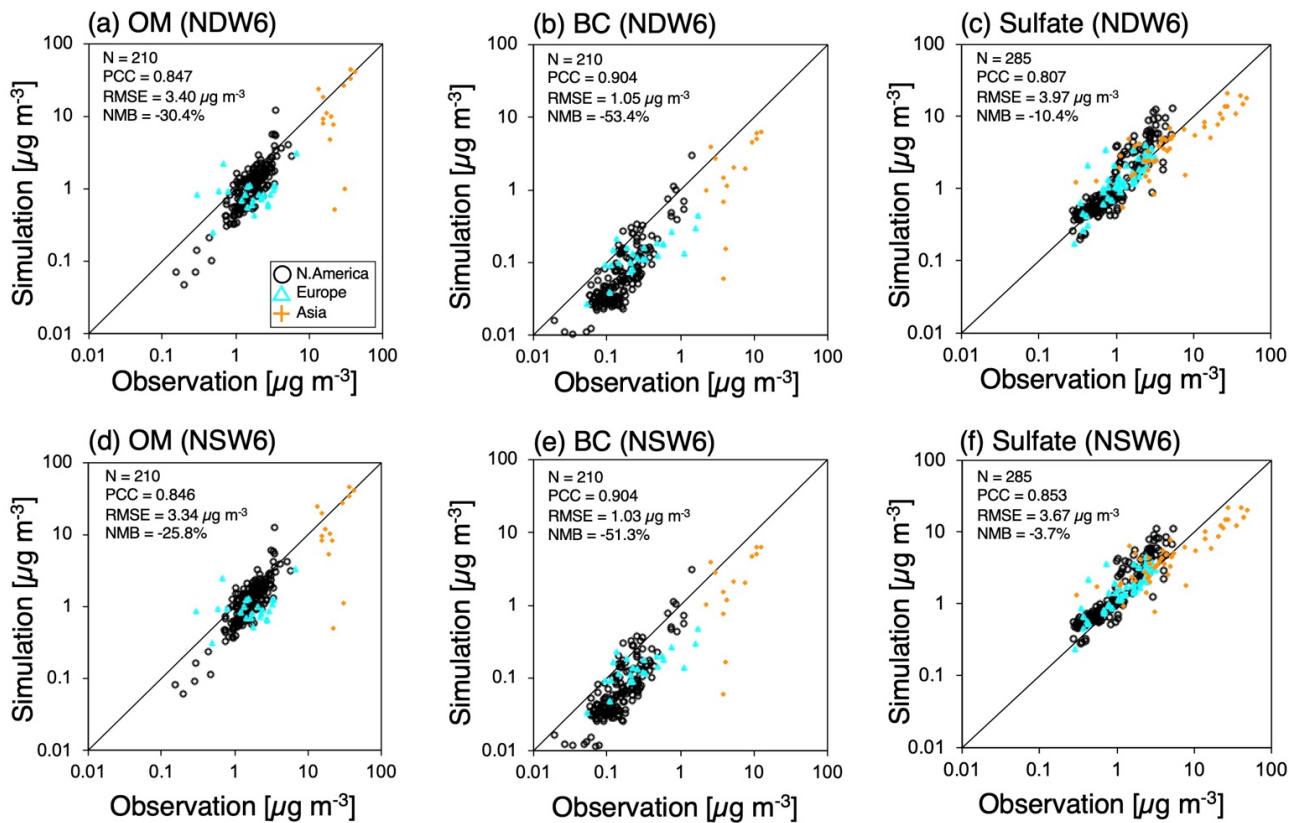
Figure 3: Scatterplots of the annual averages of surface aerosol mass concentrations (OM, BC, and sulfate) between in situ measurements (IMPROVE, EMEP, EANET and CAWNET) and the NICAM simulations (NDW6 and NSW6 ~~defined in Table 1~~). All units are in μg m⁻³. **The statistical metrics (N: sampling number, PCC: Pearson correlation coefficient, RMSE: root-mean-square error, and NMB: normalized mean bias), defined as (A1)-(A3) in Appendix A, are also shown in each panel. The values are also listed in Table A1.**
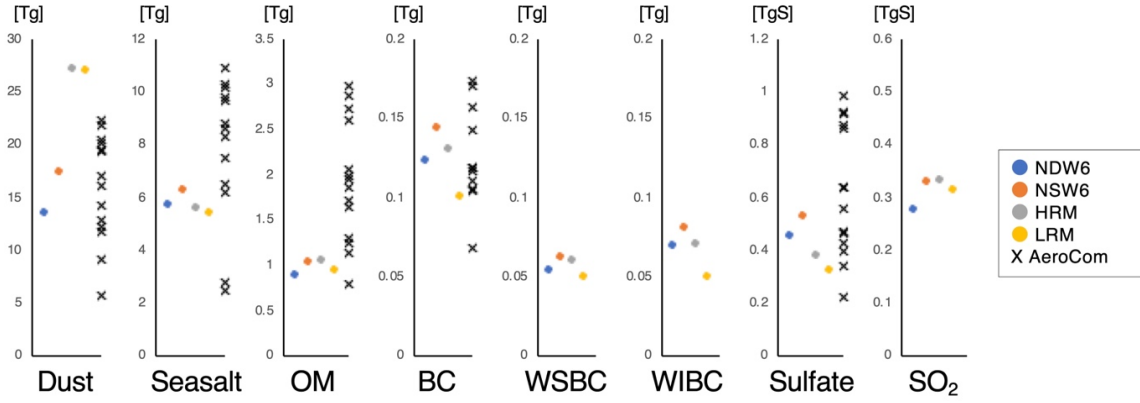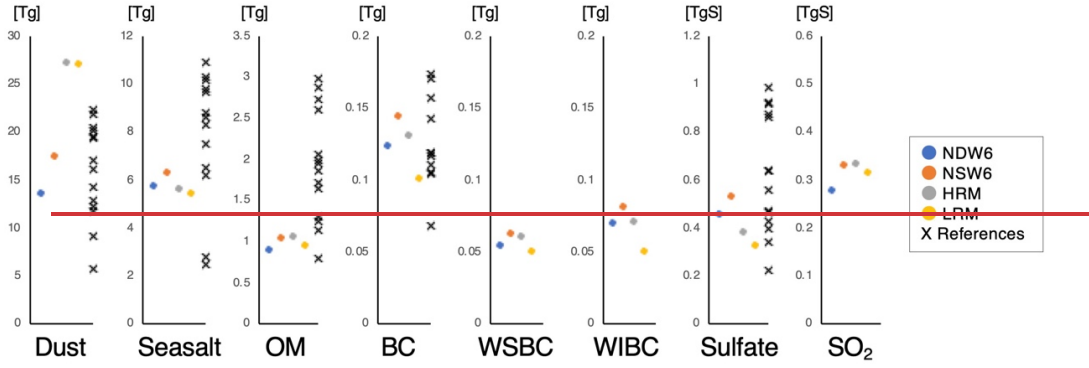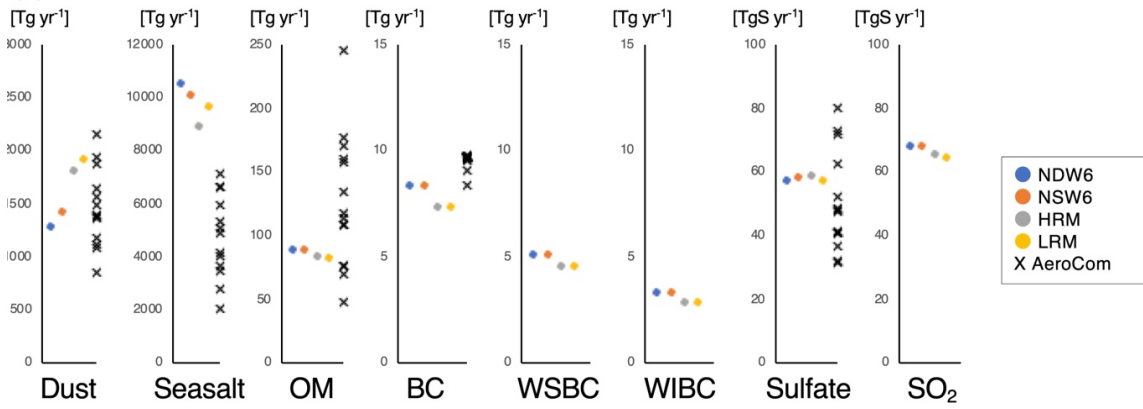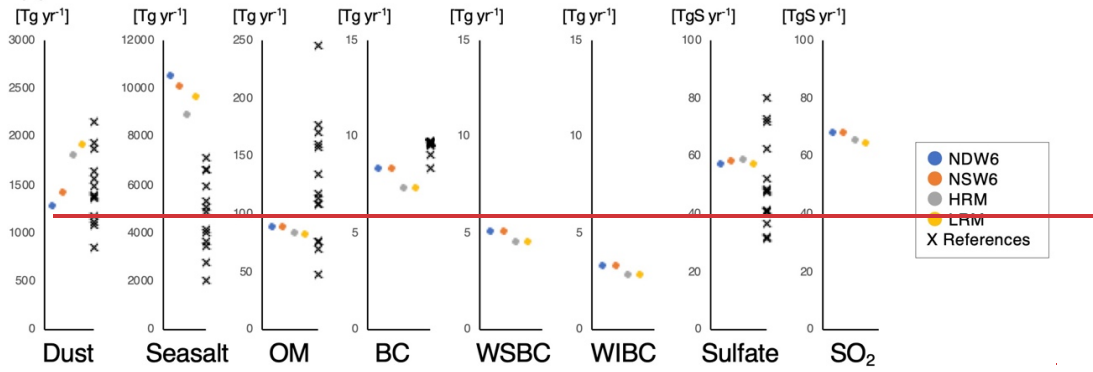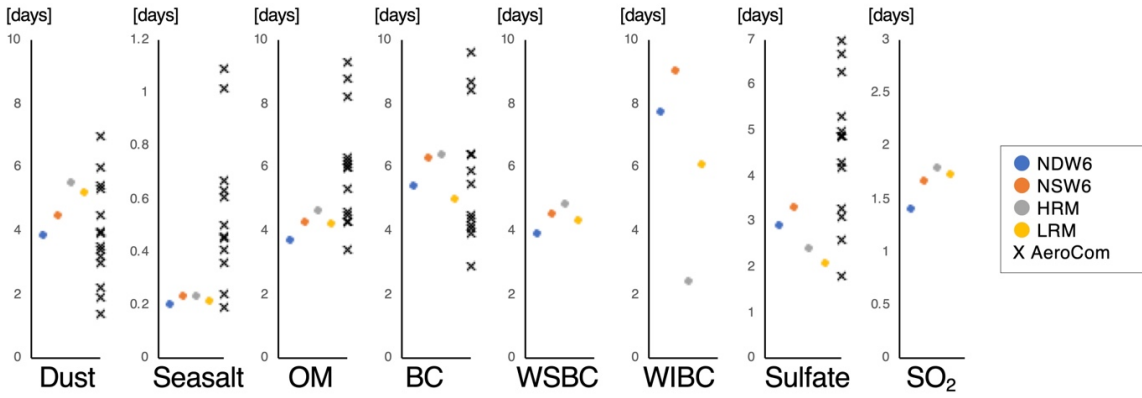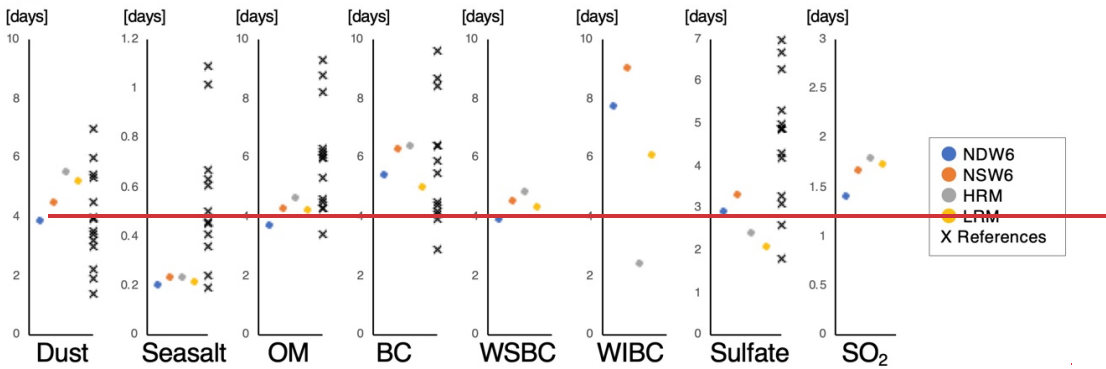
(b) Emission

Figure 4: Global and annual mean values of (a) column burdens [Tg or TgS], (b) emission fluxes [Tg yr^{-1} or TgS yr^{-1}], and (c) atmospheric lifetimes of the simulated aerosols and SO$_2$ [days]. The ~~NICAM~~ results include NDW6 and NSW6 in this study and references for the HRM and LRM in Goto et al. (2020) and AeroCom (Gliß et al., 2021). ~~———~~The values are also listed in Table ~~A1~~A2.
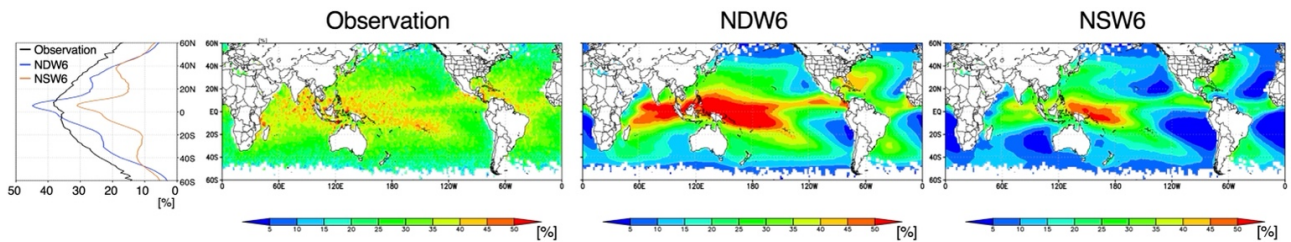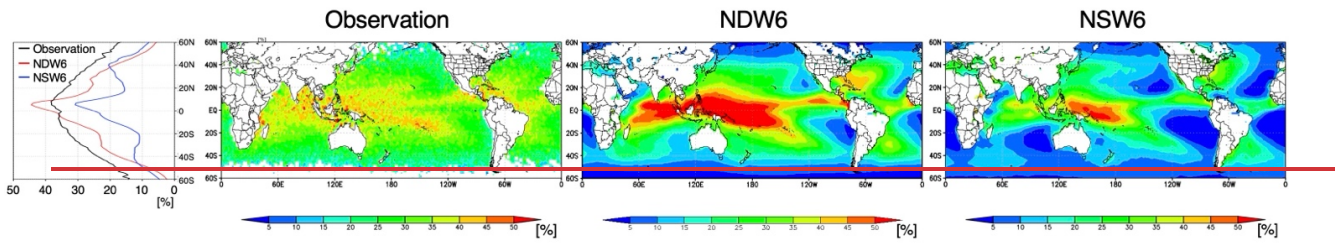
Figure 5: (a) NDW6-simulated, (b) NSW6-simulated, and (c) Cloudsat-retrieved ratio of column precipitation to the sum of column precipitation and total cloud water (RPCW) above 1 km height as annual averages. All units are in %.
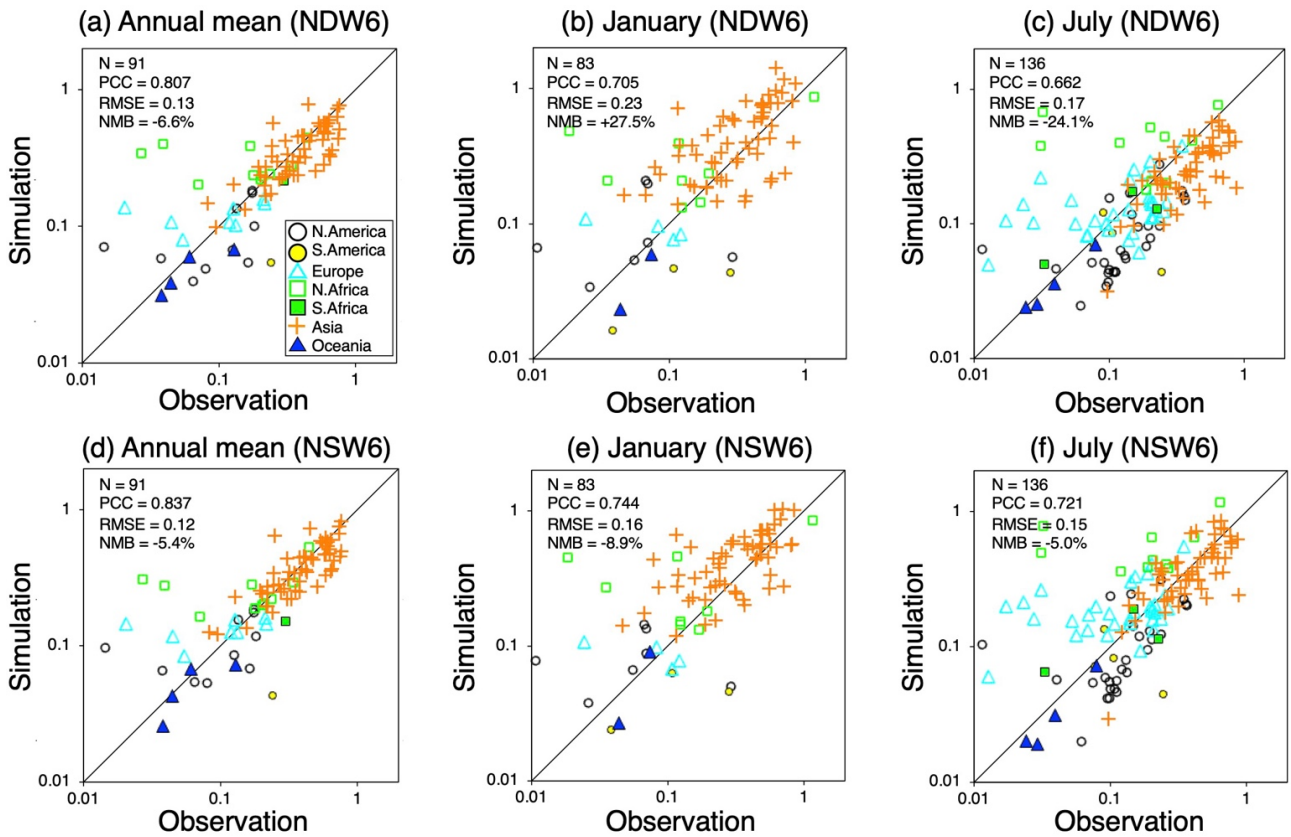
Figure 6: Scatterplot of the annual, January and July averages of AOT between ground-based measurements (AERONET, SKYNET and CARSNET) and the NICAM (NDW6 and NSW6) simulations. The different colors and symbols reflect the sites in the different regions (North America, South America, Europe, North Africa, South Africa, Asia, and Oceania) as defined in panel (a). The numbers located in the upper-left corner in each panel represent the statistical metrics, N, PCC, RMSE and NMB, which are defined as (A1)-(A3) in Appendix A.

1400
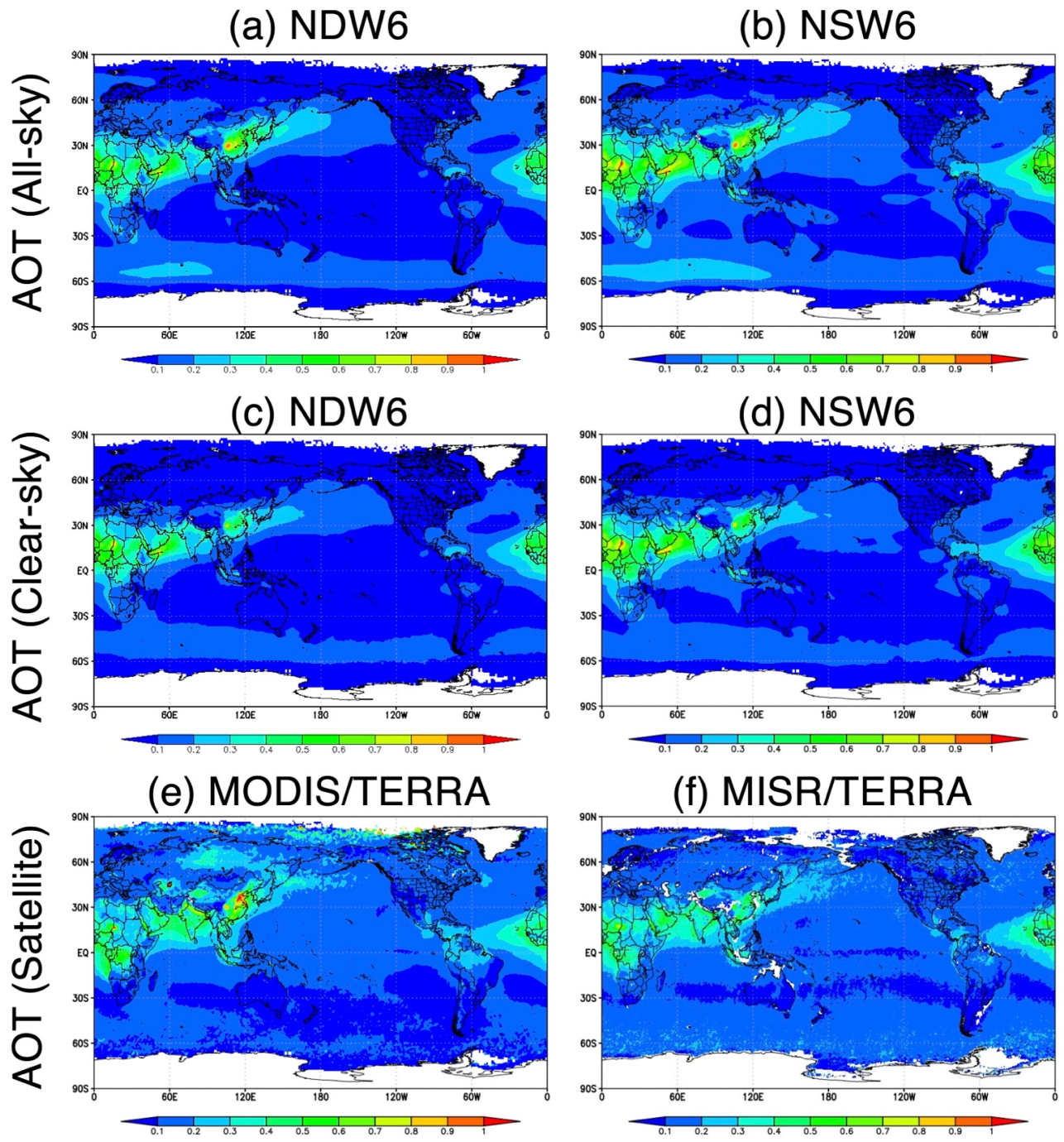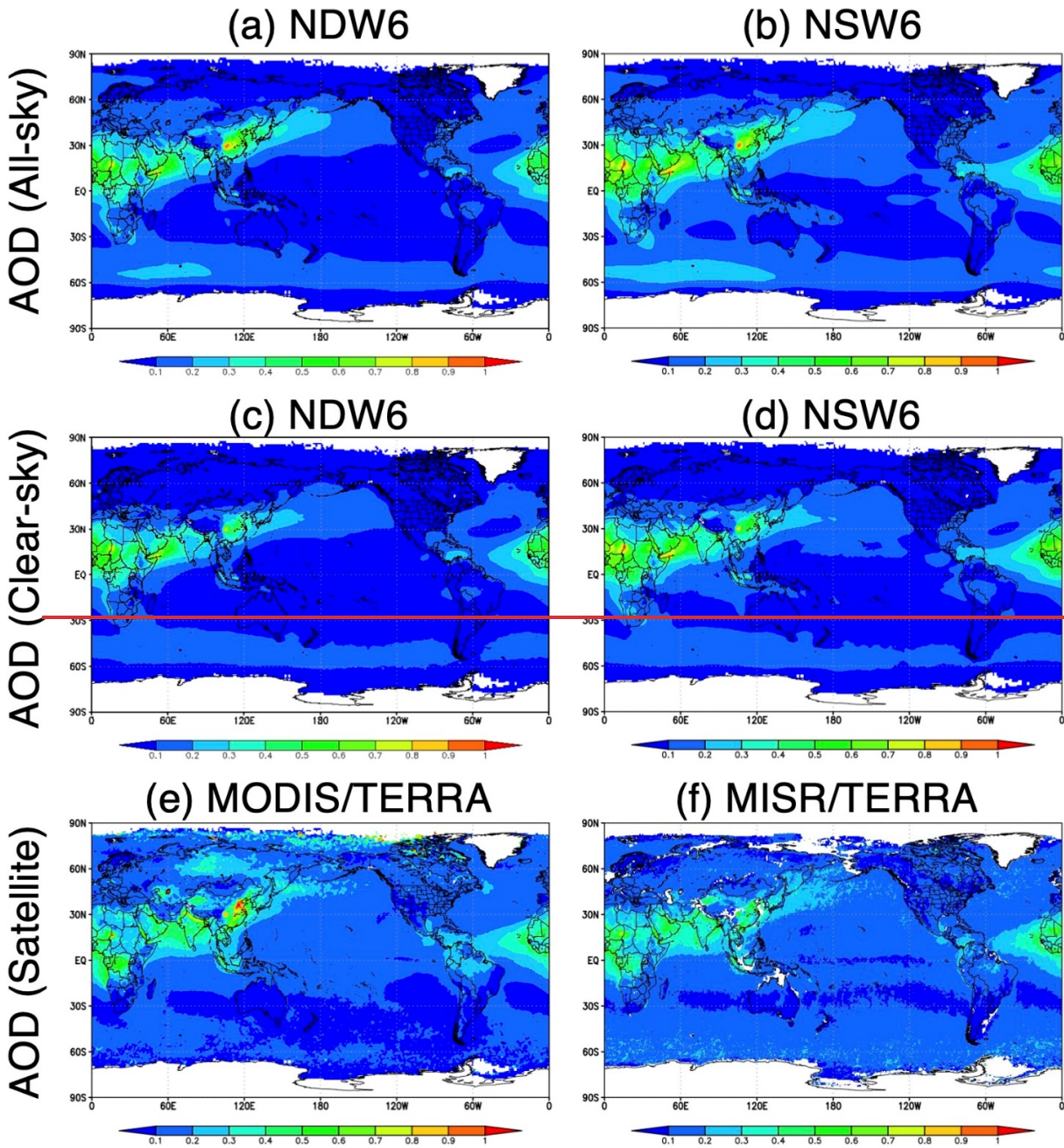
Figure 7: Global distributions of the annual averages of the NDW6-simulated AOT under (a) all-sky and (c) clear-sky conditions, the NSW6-simulated AOT under (b) all-sky and (d) clear-sky conditions, and (e) the MODIS/TERRA-retrieved and (f) the MISR/TERRA-retrieved AOT under clear-sky conditions.
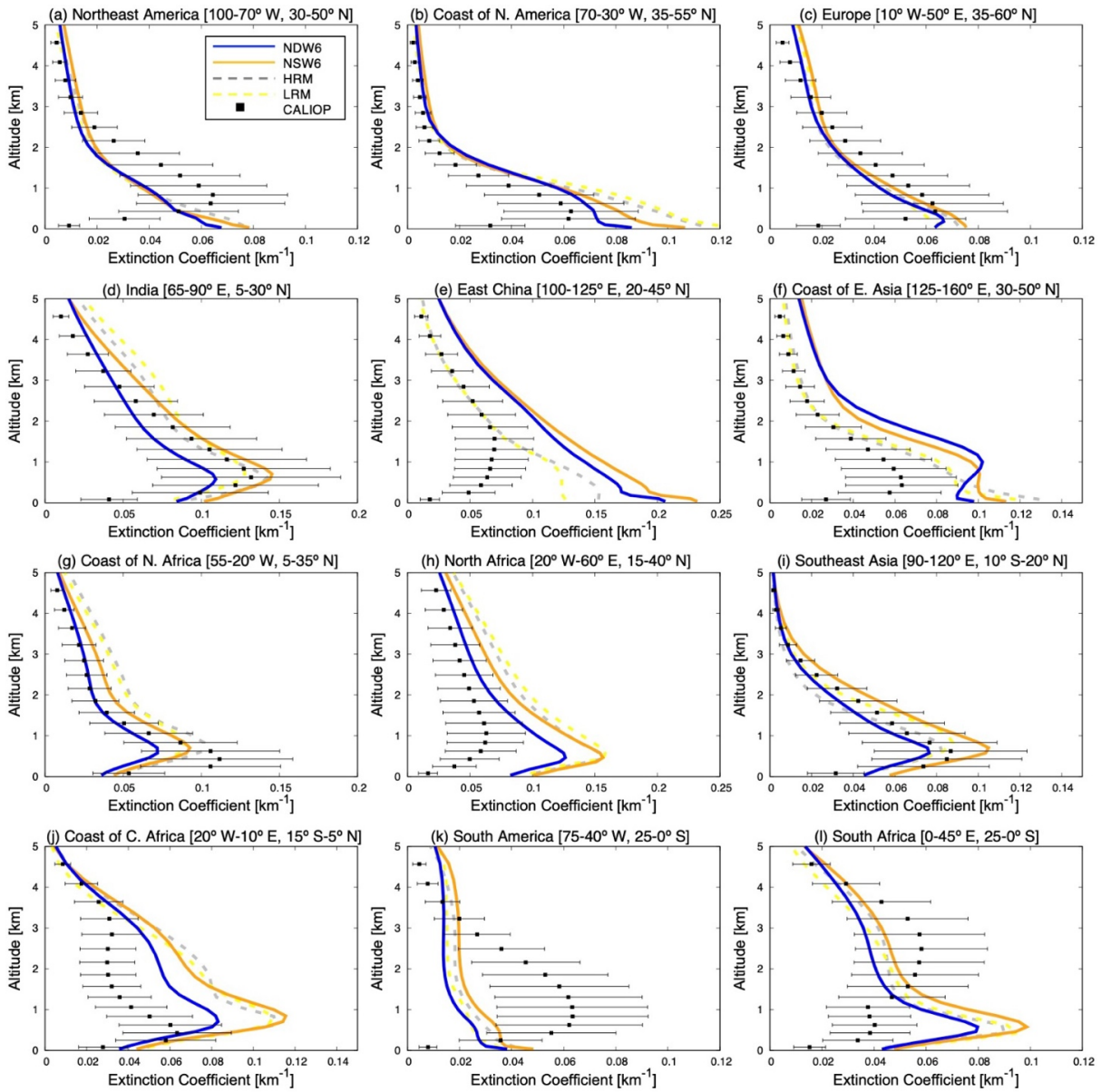
Figure 8: Vertical profiles of the annually and regionally averaged aerosol extinction coefficients from the NICAM simulations (NDW6, NSW6, HRM and LRM) and from CALIOP/CALIPSO observations in 12 different regions, which are generally defined in Goto et al. (2020) and Koffi et al. (2016). The CALIOP-retrieved values include the standard deviation of the results from 2014-2016 as bars. All units are in km^{-1}.
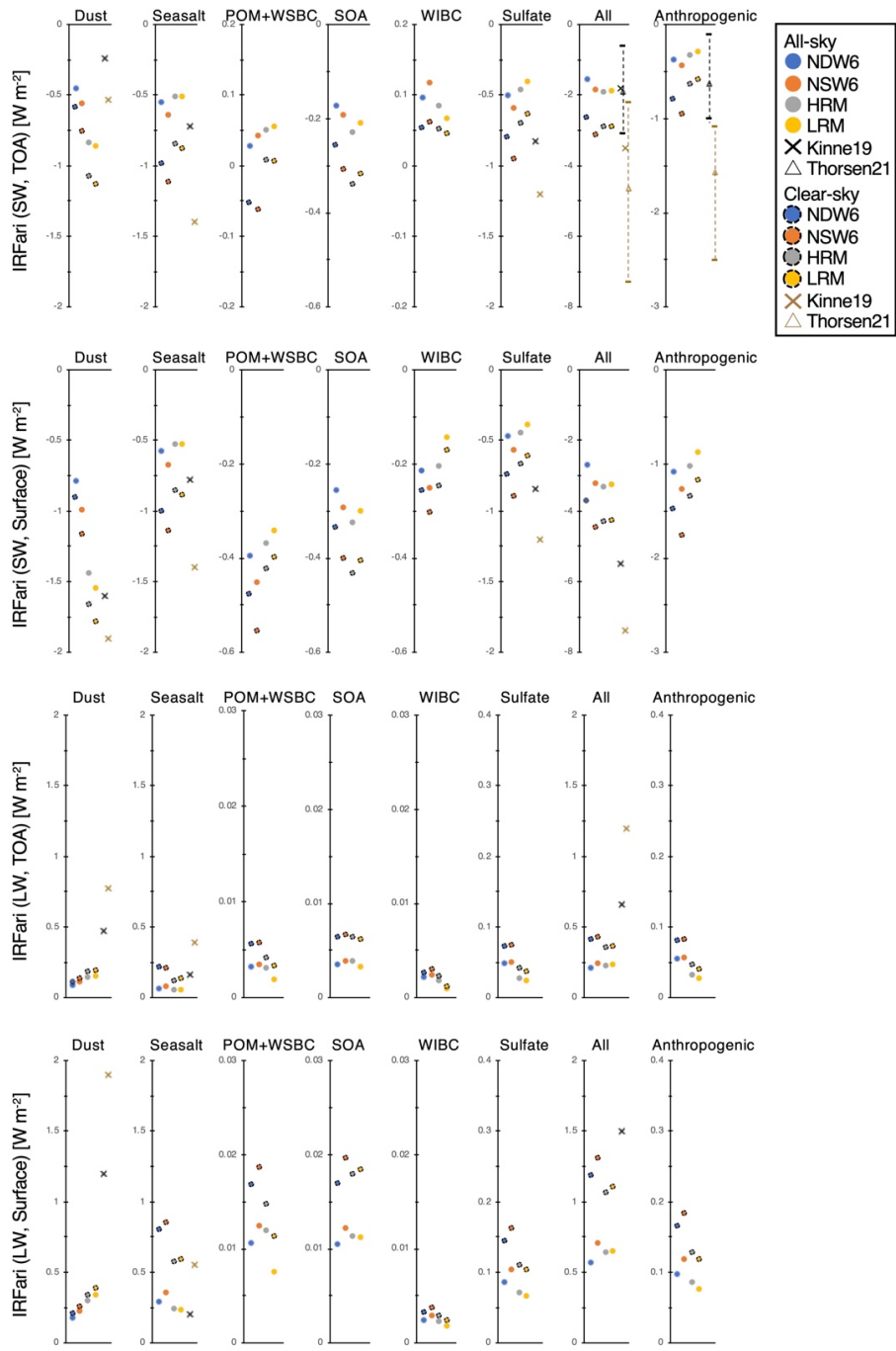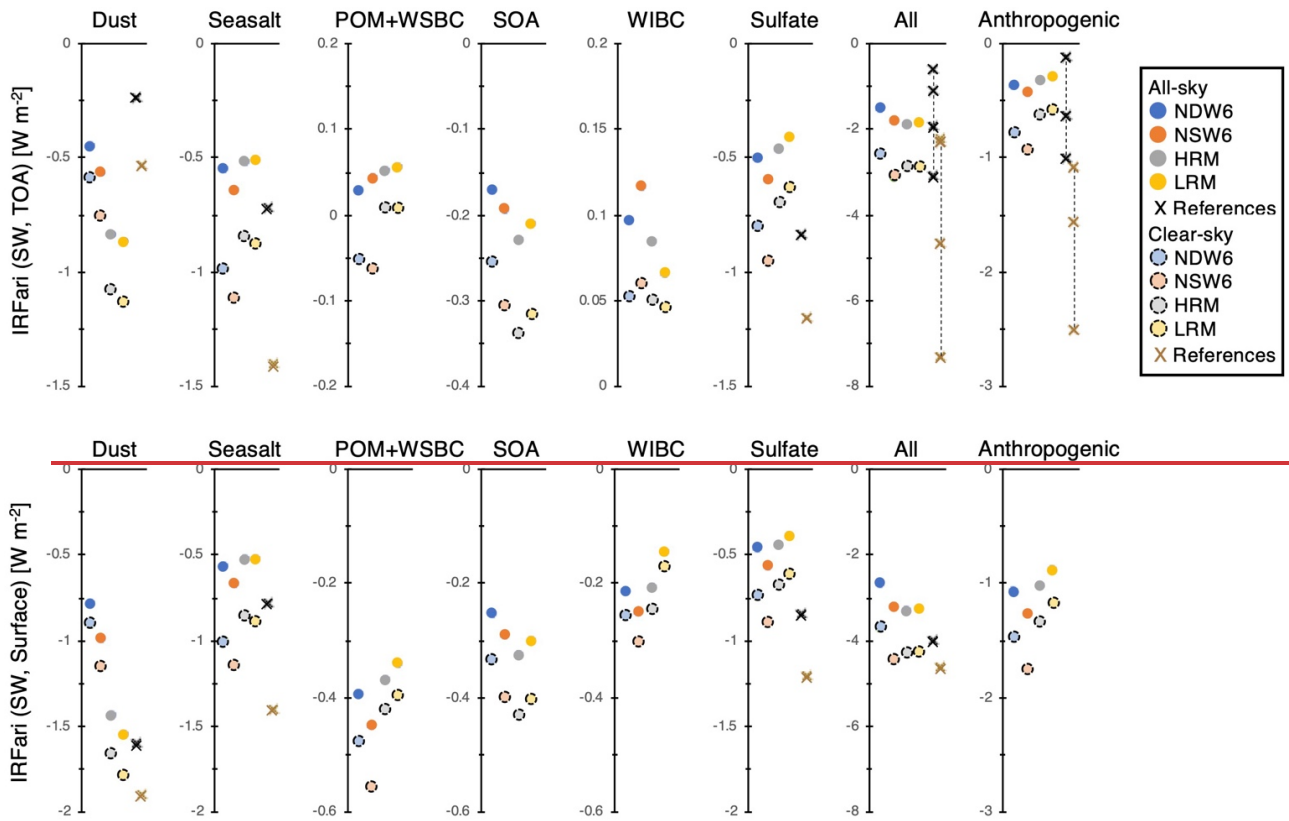
Figure 9: Instantaneous radiative forcing due to aerosol-radiation interaction (IRFari) for each aerosol (dust, sea salt, POM+WSBC, SOA, WIBC, and sulfate), total aerosols (all), and anthropogenic aerosols only (anthropogenic) for shortwave and longwave radiation at the TOA and the surface. The references are Thorsen et al. (2021) and Kinne (2019). All units are in W m⁻².
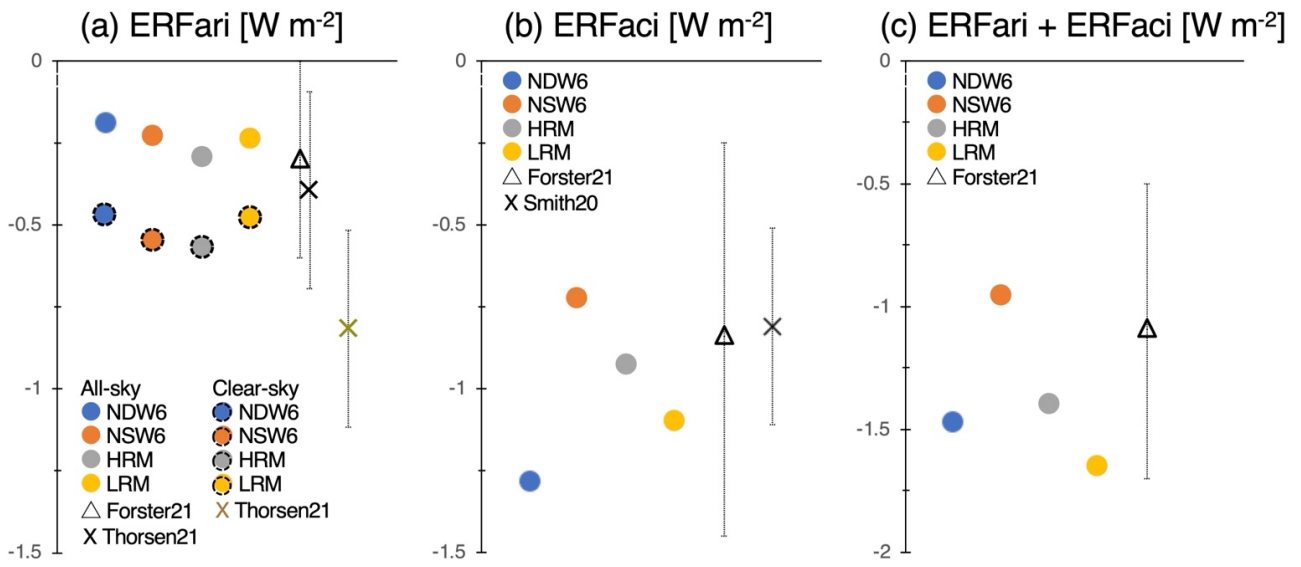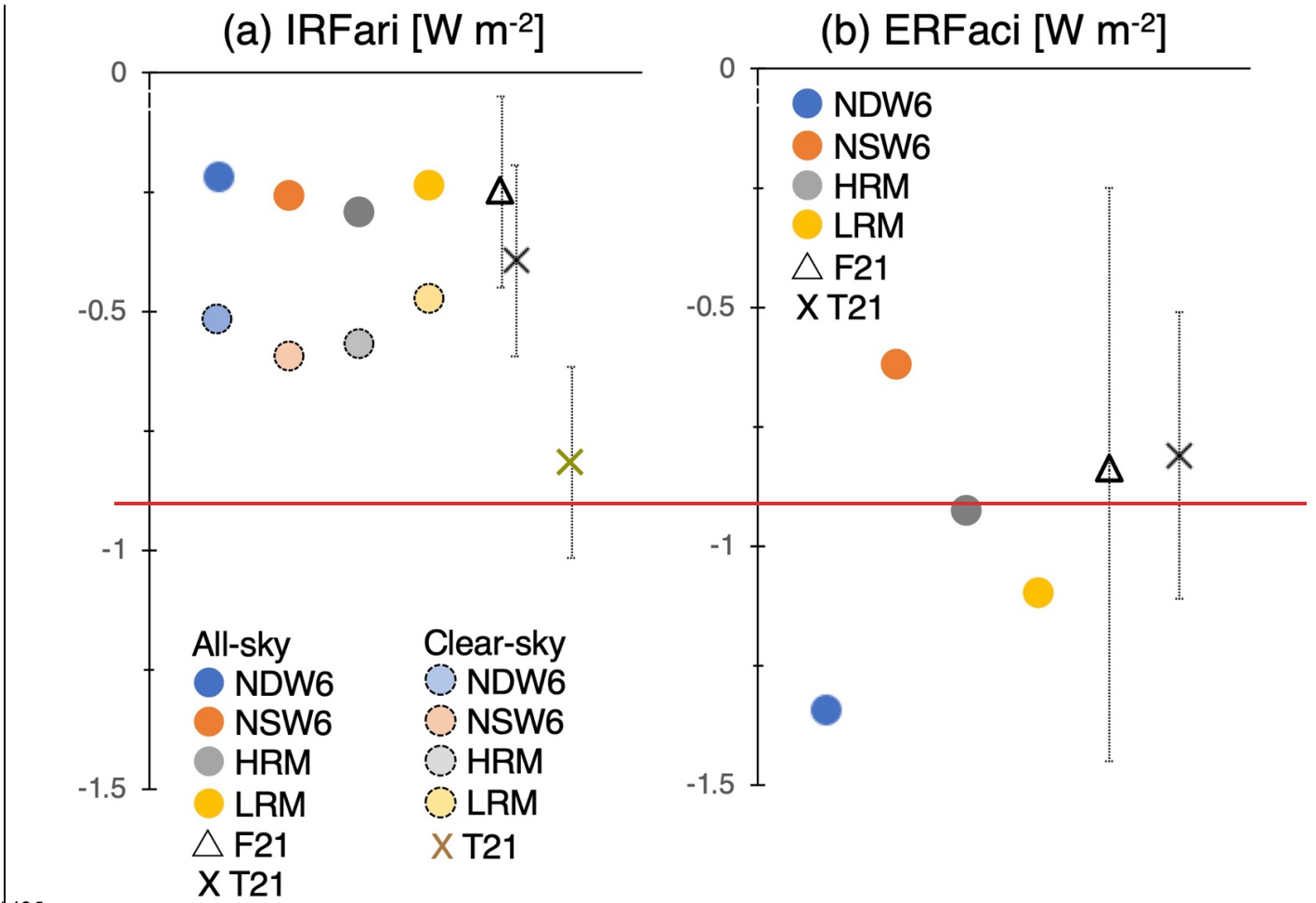
Figure 10: Global and annual mean values of (a) ~~effective~~ ~~instantaneous~~ radiative forcing for anthropogenic aerosol-radiation interaction (~~IRFari~~ERFari) for shortwave and net (sum of shortwave and longwave) radiation ~~at the TOA and~~, (b) ~~effective radiative forcing~~ERFaci for anthropogenic aerosol-cloud interaction, and (c) the net ERF (sum of ~~-~~ERFari and ~~(~~ERFaci). ~~Both~~ All units are in W m⁻². **In ERFari,** ~~The~~ the reference~~s~~ of F~~orster~~21 ~~and T21 are~~is estimated in the net radiation by IPCC-AR6 or Forster et al. (2021)~~,~~ ~~and~~ whereas the reference of Thort~~s~~en21 is estimated in the shortwave radiation by Thorsen et al. (2021)~~, respectively~~. **The reference for Smith20 is Smith et al. (2020). The values are also listed in Table 2.**

435
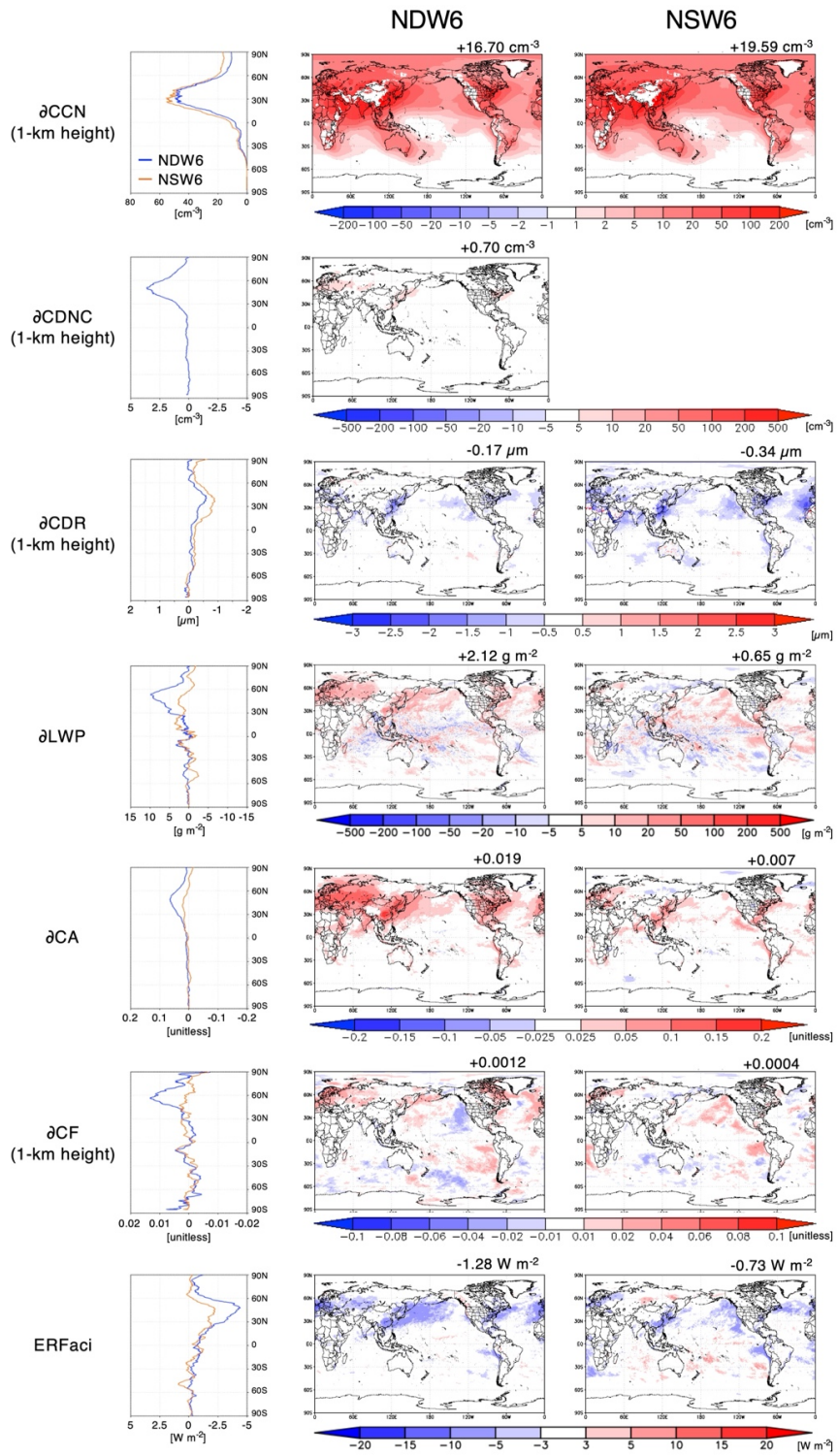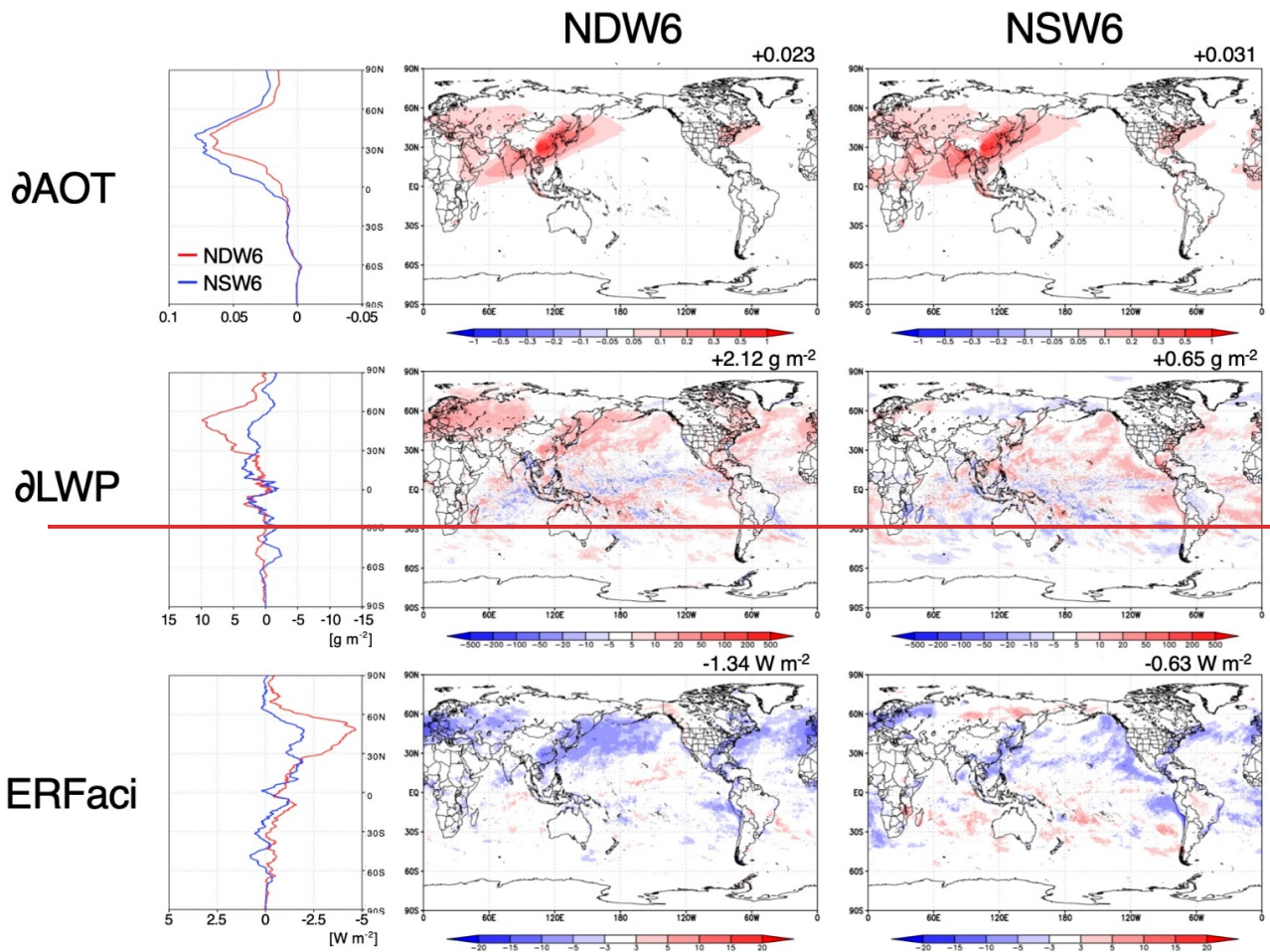
Figure 11: Global distributions of the annual averages of the NDW6- and NSW6-simulated ~~AOT~~ CCN **change at 1-km height** (∂CCN~~AOT~~**), CDNC (cloud droplet number concentrations, which in NSW6 is equal to the CCN concentrations in NSW6 due to the ignorance of sink process in the CDNC in NSW6) change at 1-km height (∂CDNC), CDR (cloud droplet effective radius for warm clouds) change at 1-km height (∂CDR),** LWP change (∂LWP), **CA (cloud albedo) change (∂CA), CF (cloud fraction) change at 1-km height (∂CF),** and ~~shortwave~~ net **ERFaci** ~~by~~ comparing the results between NDW6 and NSW6 for simulations with aerosol and precursor gas emissions for ~~between~~ the present and the preindustrial era. The number located in the upper right in each panel represents the global and annual mean value. **The results at 1-km height also include areas with elevations higher than 1-km height in white.**
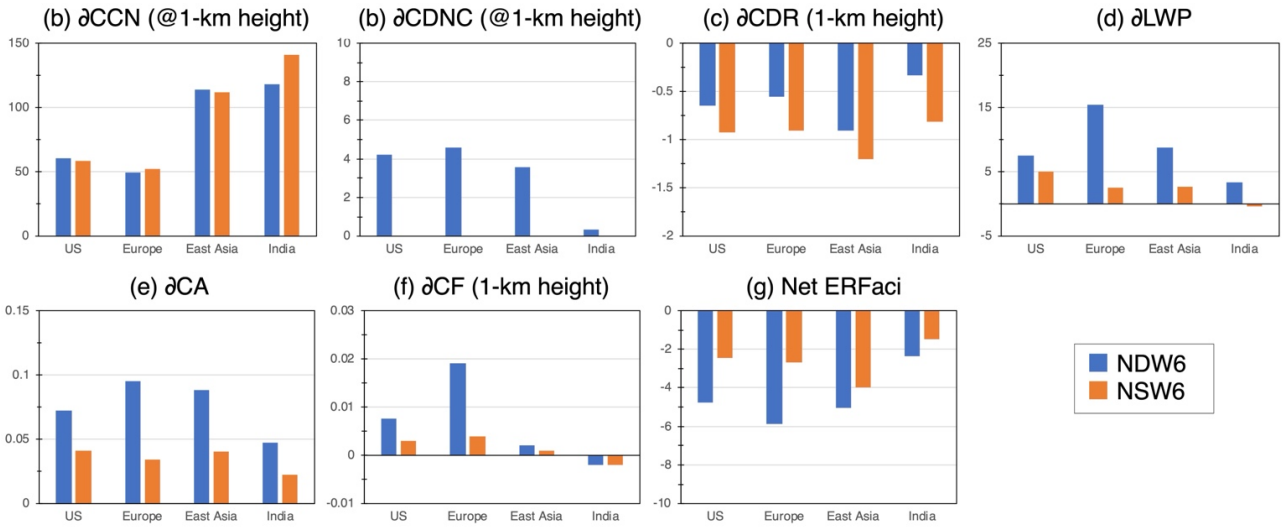
Figure 12: Regional averages of the differences in CCN at 1-km height, CDNC (cloud droplet number concentration only in NDW6), CDR (cloud droplet effective radius at 1-km height), LWP, CA (cloud albedo), CF (cloud fraction at a 1-km height), and net ERFaci between the preindustrial and the present days. The regions are defined as US (90°W-60°W, 30°N-50°N), Europe (0°E-30°E, 40°N-60°N), East Asia (110°E-140°E, 20°N-50°N), and India (70°E-90°E, 10°N-35°N).
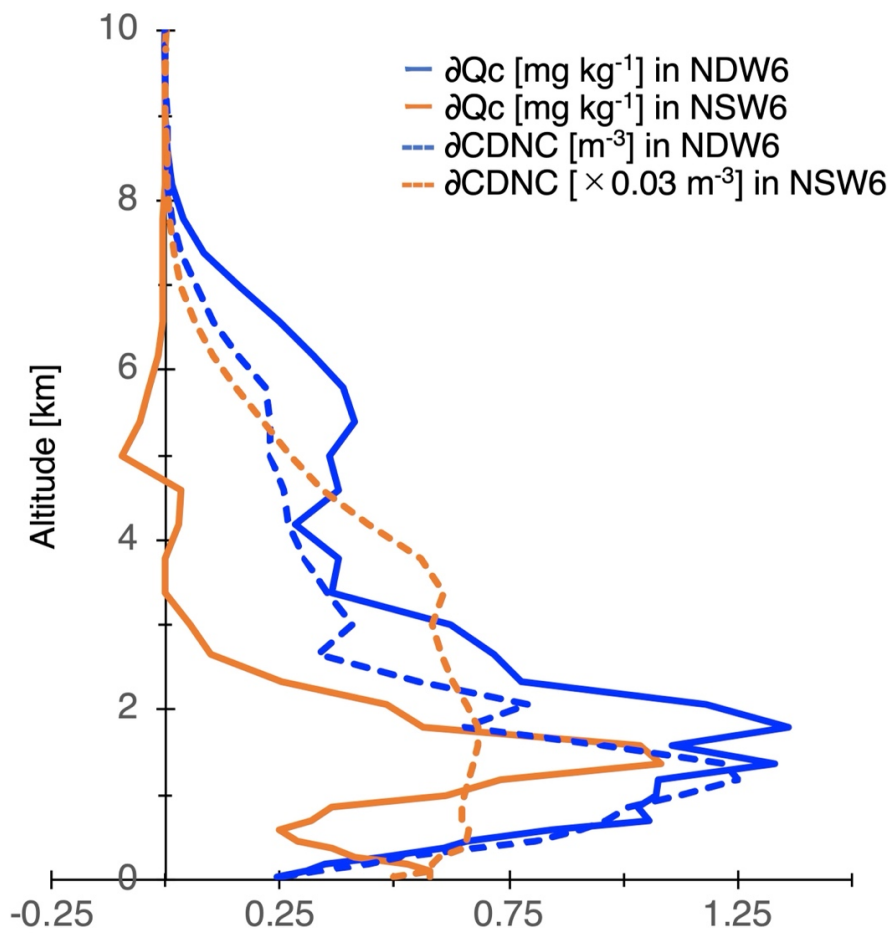
Figure 13: Global budgets of the annual averages of the NDW6- and NSW6-simulated Qc (mixing ratio of cloud droplets), the NDW6-simulated CDNC (cloud droplet number concentration), and the NSW6-simulated CDNC (cloud droplet number concentration, which is equal to CCN number concentrations)

460

Table A1: Statistical metrics of PCC, RMSE, and NMB for the annual averages of surface aerosol mass concentrations (OM, BC, and sulfate) between in situ measurements and the NICAM simulations (NDW6 and NSW6 in this study are shown in the panels of Figure 3 and HRM and LRM are shown in Figure 8 in Goto et al., 2020).

1465

	NDW6	NSW6	HRM	LRM
OM				
PCC	0.847	0.846	0.819	0.794
RMSE [μg m^{-3}]	3.40	3.34	5.03	5.21
NMB [%]	-30.4	-25.8	-54.8	-56.1
BC				
PCC	0.904	0.904	0.890	0.869
RMSE [μg m^{-3}]	1.05	1.03	1.16	1.28
NMB [%]	-53.4	-51.3	-46.4	-52.3
Sulfate				
PCC	0.807	0.853	0.815	0.768
RMSE [μg m^{-3}]	3.97	3.67	3.94	4.34
NMB [%]	-10.4	-3.7	-14.6	-23.7

Table ~~A1~~A2: Global~~ly~~ and annual~~ly~~ mean values of the NICAM-simulated aerosol budgets.

Species	Parameters [Units]	This study (NDW6)	This study (NSW6)	Goto et al. (2020) (HRM)	Goto et al. (2020) (LRM)	References from model results
Dust	Column [Tg]	13.44	17.35	27.08	27.01	16.6 (5.7-22.3)[a]
	Emission [Tg yr^{-1}]	1273	1414	1805	1911	1440 (848-5659)[a]
	Dry Deposition [Tg yr^{-1}]	234	289	342	363	396 (37-2791)[b]
	Grav. Deposition [Tg yr^{-1}]	380	452	634	663	314 (22-2475)[b]
	Wet Deposition [Tg yr^{-1}]	669	689	825	880	357 (295-1382)[b]
	Lifetime [Day]	3.82	4.43	5.49	5.17	3.7 (1.4-7.0)[a]
Seasalt	Column [Tg]	5.69	6.25	5.60	5.42	8.7 (2.5-26.4)[a]
	Emission [Tg yr^{-1}]	10486	10048	8856	9624	4980 (2030-50000)[a]
	Dry Deposition [Tg yr^{-1}]	2820	3006	2272	2169	1313[c]
	Grav. Deposition [Tg yr^{-1}]	2169	2316	1998	1951	327[c]
	Wet Deposition [Tg yr^{-1}]	5498	4726	4586	5504	1889[c]
	Lifetime [Day]	0.20	0.23	0.23	0.21	0.56 (0.19-1.51)[a]
OM	Column [Tg]	0.88	1.02	1.04	0.94	1.91 (0.79-2.99)[a]
	Emission [Tg yr^{-1}][h]	87.2	87.2	82.2	81.9	116.0 (48.0-246.0)[a]
	Dry Deposition [Tg yr^{-1}]	7.0	7.4	6.3	6.6	approximately 15 (0.2-28)[d]
	Grav. Deposition [Tg yr^{-1}]	6.1	6.8	3.7	3.9	
	Wet Deposition [Tg yr^{-1}]	74.3	73.8	72.6	71.4	approximately 90 (approximately 50-140)[d]
	Lifetime [Day]	3.66	4.24	4.60	4.17	6.0 (3.4-9.3)[a]
BC	Column [Tg]	0.12	0.14	0.13	0.1	0.131 (0.068-0.260)[a]
	Emission [Tg yr^{-1}][h]	8.3	8.3	7.3	7.3	9.7 (8.4-9.7)[a]
	Dry Deposition [Tg yr^{-1}]	0.9	1.0	0.8	0.8	
	Grav. Deposition [Tg yr^{-1}]	0.3	0.3	0.2	0.2	
	Wet Deposition [Tg yr^{-1}]	7.1	7.0	6.3	6.3	
	Lifetime [Day]	5.38	6.26	6.37	4.96	5.5 (2.9-8.7)[a]
WSBC	Column [Tg]	0.05	0.06	0.06	0.05	0.19[f]
	Emission [Tg yr^{-1}][i]	5.0	5.0	4.5	4.5	
	Dry Deposition [Tg yr^{-1}]	0.5	0.5	0.4	0.4	
	Grav. Deposition [Tg yr^{-1}]	0.3	0.3	0.2	0.2	
	Wet Deposition [Tg yr^{-1}]	4.3	4.3	3.9	3.9	
	Lifetime [Day]	3.88	4.49	4.78	4.29	6.4[f]
WIBC	Column [Tg]	0.07	0.08	0.07	0.05	0.03[f]

	Emission [Tg yr^{-1}] [i]	3.3	3.3	2.8	2.8	
	Dry Deposition [Tg yr^{-1}]	0.5	0.5	0.4	0.4	
	Grav. Deposition [Tg yr^{-1}]	0.0	0.0	0	0	
	Wet Deposition [Tg yr^{-1}]	2.8	2.8	2.4	2.4	
	Lifetime [Day]	7.68	9.00	8.95	6.04	1.0[f], 1.0-1.7[g], 9.6 (w/o aging)[g]
Sulfate	Column [TgS]	0.45	0.52	0.38	0.32	0.60 (0.22-0.98)[a]
	Production [TgS yr^{-1}]	57.1	57.8	58.4	56.7	37.6-61.1[c]
	from the gas phase	13.3	14.6	16.8	16.1	6.2[c] -17.4[e]
	from the aqueous phase	43.7	43.2	41.7	40.6	21.1[e]-58.8[c]
	Dry Deposition [TgS yr^{-1}]	3.8	4.6	3.9	3.6	5.8-7.6[c]
	Grav. Deposition [Tg yr^{-1}]	0.1	0.1	0.5	0.4	0.0[c]
	Wet Deposition [TgS yr^{-1}]	53.4	53.4	52.0	50.4	31.8-53.5[c]
	Lifetime [Day]	2.89	3.29	2.38	2.05	4.9 (1.8-7.0)[a]
SO$_2$	Column [TgS]	0.28	0.33	0.33	0.31	
	Production [TgS yr^{-1}][h]	67.8	67.~~5~~7	65.0	64.1	
	Chemical loss (gas phase)	13.3	14.6	13.0	12.5	
	Chemical loss (aqueous phase)	43.7	43.2	41.7	40.6	
	Dry Deposition [TgS yr^{-1}]	13.0	13.2	11.7	12.0	
	Wet Deposition [TgS yr^{-1}]	2.3	1.8	1.4	1.1	
	Lifetime [Day]	1.40	1.66	1.79	1.72	

1470 [a] Gliß et al. (2021); [b] Huneeus et al. (2011); [c] Takemura et al. (2000); [d] Tsigaridis et al. (2014); [e] Goto et al. (2011); [f] Chung and Seinfeld (2002); [g] Goto et al. (2012); [h] The global and annual mean values in this study (NDW6 and NSW6) are slightly different from those (HRM and LRM) in Goto et al. (2020) because the method of remapping from a latitude-longitude grid emission map to an icosahedral grid in NICAM is modified in this study.

1475
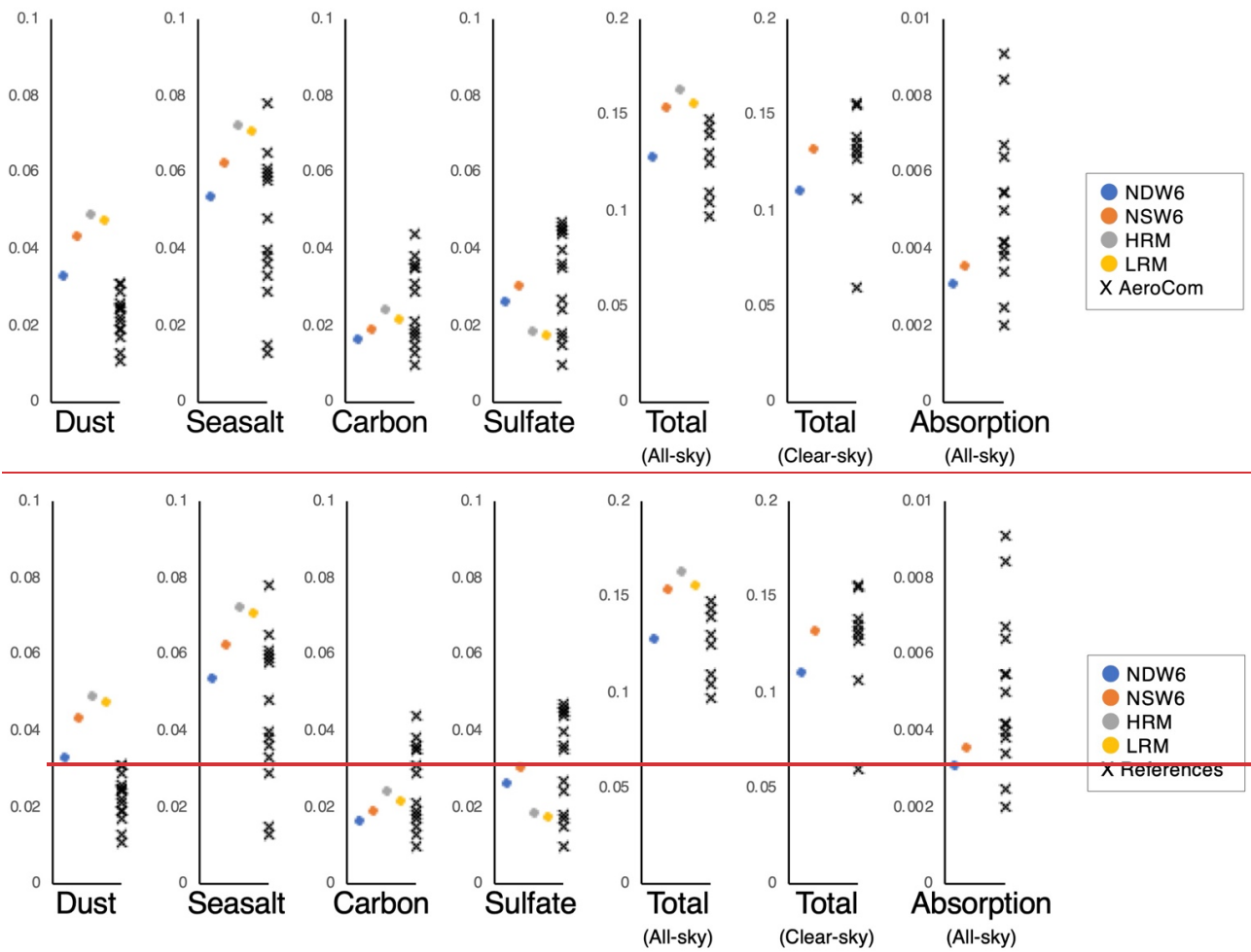
Figure C1: Global and annual mean values of AOT for chemical components (dust, sea salt, carbonaceous aerosols, and sulfate) under all sky conditions, AOT of total aerosols under both all-sky and clear-sky conditions, and absorption AOT under all-sky conditions. There are no HRM and LRM results for AOT under clear-sky conditions and absorption AOT.
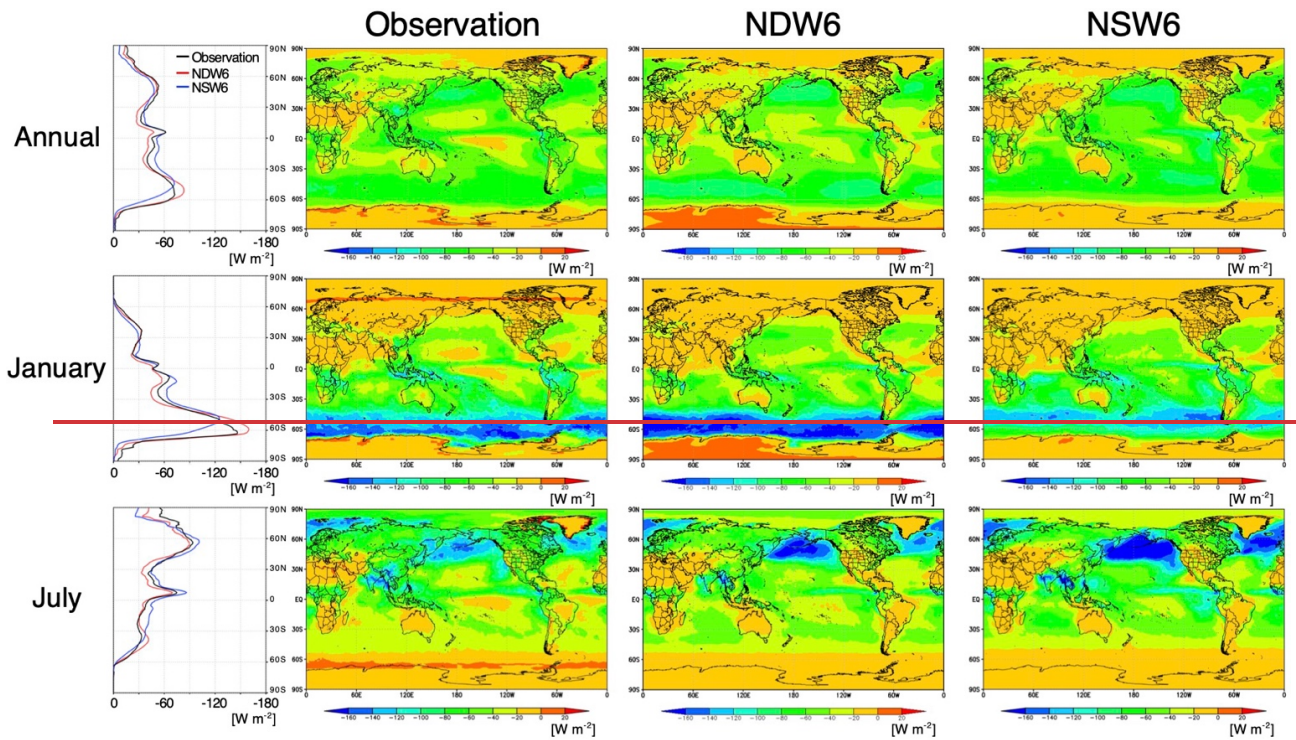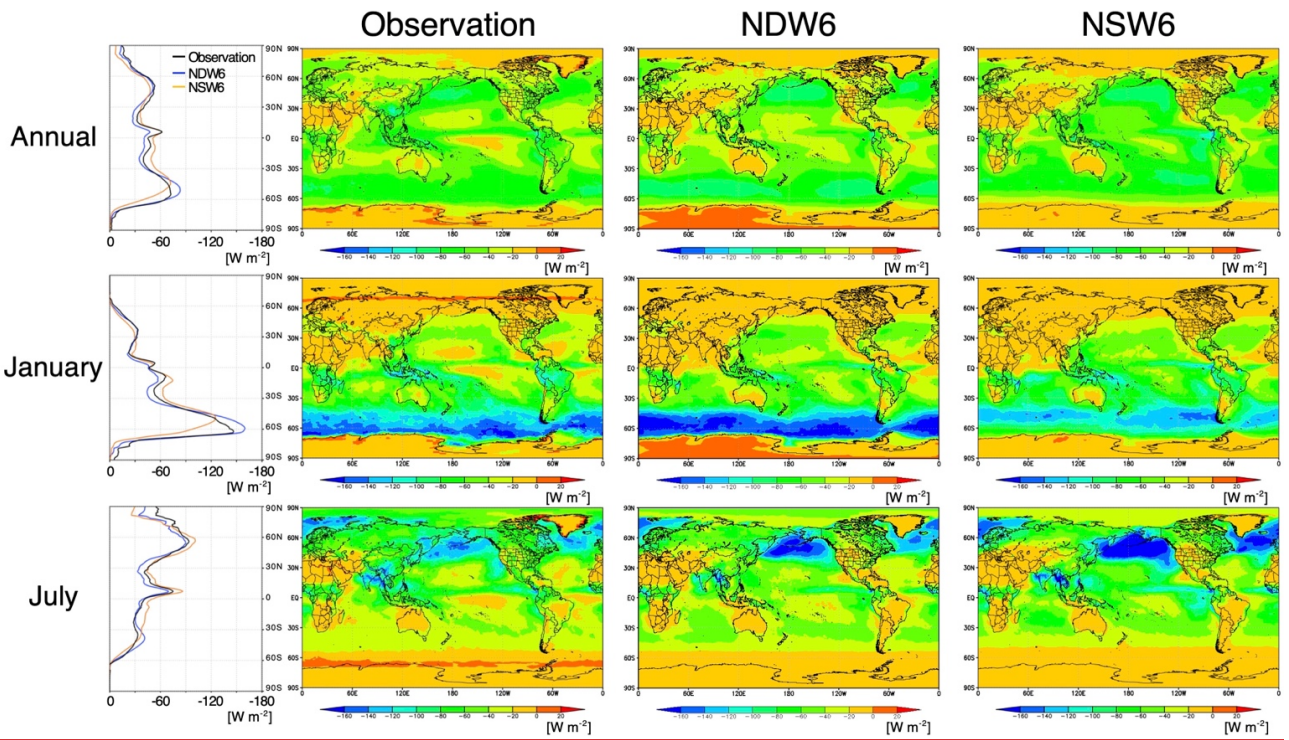
485 **Figure E1: Zonal and horizontal distribution of SWCRF (NDW6 and NSW6 ~~defined in Table 1~~simulations and CERES as ~~anSame as Figure 1 but for SWCRF. The~~ observation ~~is from CERES)~~ as annual, January, and July averages. All units are in W m^{-2}.**
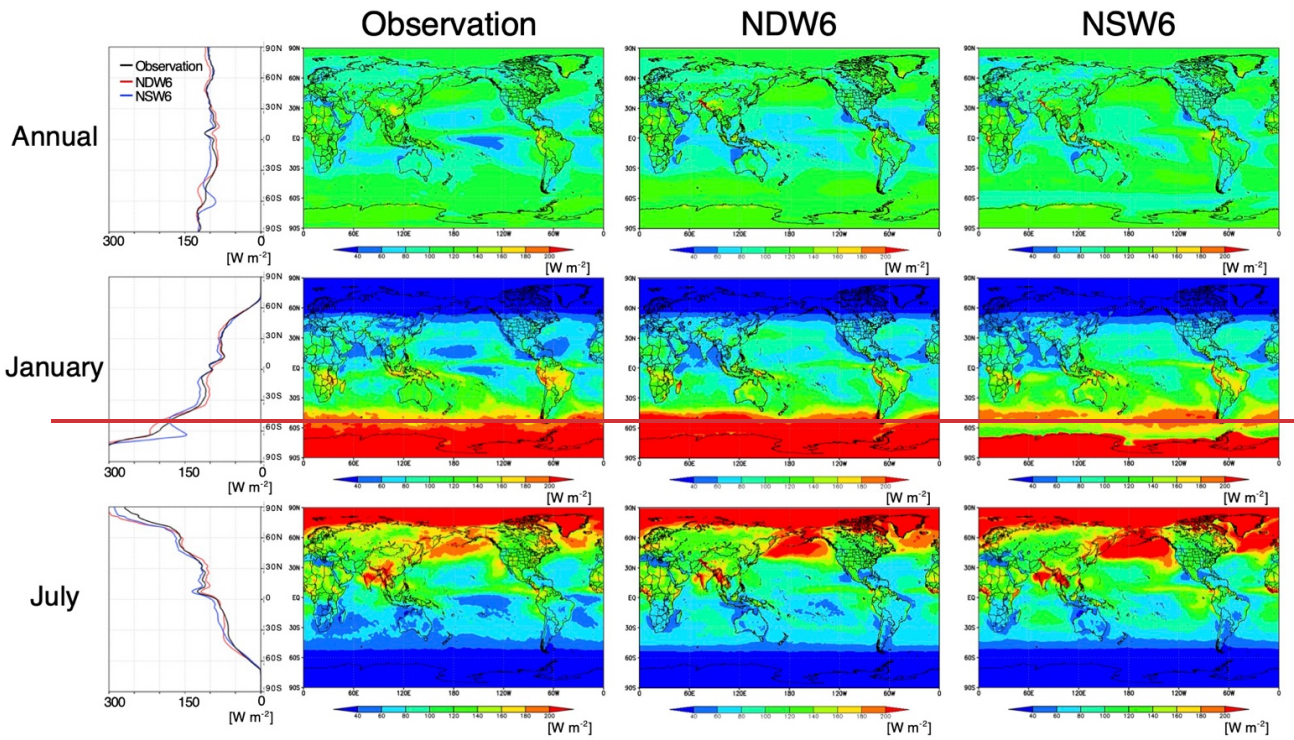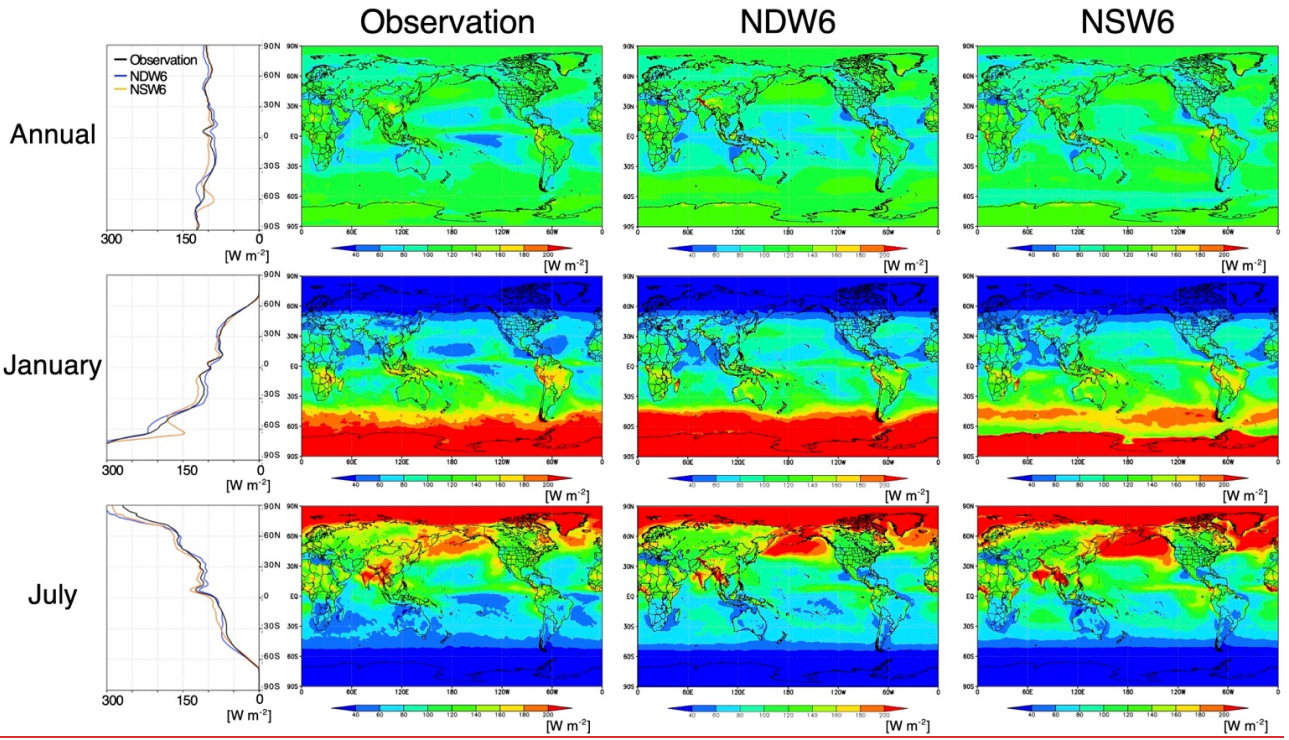
Figure E2: Same as Figure E1 but for OSR.